12-2018

Spatiotemporal Effects of Transport and Network Topology in Biological Systems

Paul John Mlynarczyk
University of Tennessee, pmlynarc@vols.utk.edu

To the Graduate Council:

I am submitting herewith a dissertation written by Paul John Mlynarczyk entitled "Spatiotemporal Effects of Transport and Network Topology in Biological Systems." I have examined the final electronic copy of this dissertation for form and content and recommend that it be accepted in partial fulfillment of the requirements for the degree of Doctor of Philosophy, with a major in Chemical Engineering.

Steven M. Abel, Major Professor

We have read this dissertation and recommend its acceptance:

Paul Dalhaimer, Maitreyi Das, Paul Frymier

Accepted for the Council:
Carolyn R. Hodges

Vice Provost and Dean of the Graduate School

(Original signatures are on file with official student records.)

Spatiotemporal Effects of Transport and Network Topology in Biological Systems

A Dissertation Presented for the

Doctor of Philosophy

Degree

The University of Tennessee, Knoxville

Paul John Mlynarczyk

December 2018

To my loving wife Jisha

Thank you for your unwavering support and enduring patience

Acknowledgments

I would like to first and foremost thank my advisor, Dr. Steve Abel, for his exceptional intellectual guidance throughout my graduate research. His diligence and highly professional scientific approach has been instrumental in both my academic training and professional development. I would also like to acknowledge my fellow research group members, especially Dr. Aaron Prescott and Rob Pullen, for numerous insightful discussions throughout the course of several research projects. Many of the key results I have achieved can be directly attributed to their supportive influence and noteworthy suggestions. Also, I would be remisced if I didn't thank my experimental collaborators from the BCMB department, Dr. Maitreyi Das and Dr. Andreas Nebenführ, for providing both motivation and scientific direction in projects detailed in this thesis. Finally, I'd like to thank the National Science Foundation and the University of Tennessee for providing funding to make all of this research possible.

Abstract

Emergent biological phenomena, although observed experimentally, are often not easily characterized or understood. Biological systems are often comprised of many interacting components, which may yield highly complex dynamics. A thorough understanding of these systems often requires a multi-faceted approach involving both experimental and computational techniques. Computer simulation allows for precise definition of system components and facilitates a wider exploration of the system parameter space, often leading to accelerated scientific discovery. In this thesis, we apply stochastic simulation methods to characterize the spatiotemporal behavior of three distinct biological systems. We first explore the role of spatial confinement and diffusion in a bistable reaction network with positive feedback. We find that confined systems with high molecular mobility promote the active steady state, and stochastic switching occurs unidirectionally by nucleation and growth of single active clusters. The results provide a general framework for studying geometry and diffusion in positive feedback networks, and suggest that confinement can be used to initiate the formation of localized active clusters of molecules that then propagate to activate a system. Next, we study transport properties of single molecular motors traversing cytoskeletal networks with random filament configuration. We find that systems containing few, long filaments exhibit slow and highly variable transport. Particular filaments are capable of having an outsized influence on first-passage times by acting as lynchpins that transport motors to and from regions of the system that act as traps that promote extended occupancy. Finally, we use two distinct models to explore the dynamics of protein organization along an actomyosin ring. We find that a positive feedback circuit can be used to establish and maintain polarized protein distributions, and clustering is suppressed by endocytosis and fast diffusion. In the absence of positive feedback and dissociation from

the ring, we find that slow association of large patches leads to clustered distributions of higher variability. These results suggest that homogeneous spatial distribution of proteins in mature actomyosin rings may depend on frequent association of small protein clusters. Taken collectively, these findings suggest that stochastic computational modeling can facilitate the elucidation of key mechanistic features of emergent biological phenomena.

Table of Contents

List of Tables

List of Figures

Chapter 1

Introduction

1.1 Computational Modeling in Biology

Emergent biological phenomena, although observed experimentally, are often not easily characterized or understood. Biological systems are typically comprised of many interacting components, which may yield highly complex dynamics. A thorough understanding of these systems often requires a multi-faceted approach involving both experimentation and computational modeling. *In vivo* and *in vitro* experiments are useful in elucidating key features and behavior of biological systems under certain conditions, but application of *in silico* methods expands capability by facilitating a wider exploration of the system parameter space and underlying biological mechanisms [82]. Computer simulation allows for precise definition of system components and testing of a wide variety of conditions. The growing availability of a wide array of computational resources renders computer simulation increasingly useful as a method of research. Through successful implementation of these complementary methods, underlying biological mechanisms can be better understood and predictions under alternate conditions can be effectively extrapolated.

A particular challenge of research on living systems is the inherent dependence of system behavior on spatiotemporal factors. For example, a cell may exhibit drastically different behavior over time as the spatial distribution of specific signaling molecules on its membrane undergoes changes. At the cellular population level, the stochasticity in protein copy number and in protein motion allow for genetically identical cells to exhibit phenotypic

differences, even in the same environment. Spatial inhomogeneity often accompanies critical cellular processes such as cytokinesis [154] and immune cell activation [30], which are characterized by large changes in spatial organization over relatively short timescales. A thorough understanding of these processes and other stochastic biological phenomena is often not attainable through simple observation, and so theoretical and computational methods become important tools for gaining insight [99].

The most useful and sustainable paradigm for computational modeling in biological systems research involves a recurring iterative feedback loop between *in silico* models and *in vivo / in vitro* experiments. Fundamentally, a model that does not incorporate biologically relevant parameters or display consistency with experimentally observed phenomena will not be readily accepted by experimentalists who study biological systems. The first challenge in constructing a computational model is deriving a quantitative description of a biophysical system. Appropriate molecular sizes, diffusion coefficients, kinetic rates, and other such quantities must be implemented to accurately simulate system behavior. While many of these values have been discovered and well documented through classical experimentation and measurement, some remain unknown and are unattainable by available experimental methods. In these cases, approximations of reasonable parameter ranges must be made. Parameter sweeps can then be employed to identify most likely parameter values that correspond to a given observation in system behavior, thus providing useful feedback for laboratory experiments. This two-way feedback between experimentally observed results and computationally simulated results allows for successive and educated hypothesis refinement, and thus can effectively lead to accelerated scientific discovery.

1.2 Simulation of Biophysical Processes

In a broad context, computational models fall into one of two categories: deterministic or stochastic.

1.2.1 Deterministic Modeling

In deterministic models, the output of the model is fully determined by the parameter values and the intial conditions. In other words, a deterministic model that uses the same given set of parameter values and initial conditions will always produce the same output result. A simple illustration of a deterministic model can be seen in traditional chemical kinetics. Here, the populations of N different chemical species evolve in time in a well-stirred, thermally equilibrated chemical system according to a set of coupled ordinary differential equations (ODEs) of the form:

$$\frac{dX_i}{dt} = f_i(X_i, ..., X_N) \qquad (i = 1, ..., N) \tag{1.1}$$

where X_i represents the number of molecules of species i and the functions f_i are inferred from the specifics of the interactions between various chemical species and include kinetic parameter values. For systems of size on the mL scale or greater, this set of ODEs approximates the system behavior quite well [90]. However, for smaller systems containing relatively small numbers of molecules of one or more reactant species, discreteness and stochasticity may play critical roles in determining the emergent system behavior. Since this situation often arises in the context of subcellular and cellular systems [100, 21, 116, 124, 16, 39, 38], the use of stochastic models becomes especially appropriate in computational biology.

1.2.2 Stochastic Modeling

Spatiotemporal dynamics of stochastic cellular processes are commonly studied using a variety of stochastic methods that fall under the broad classification of kinetic Monte Carlo algorithms [45, 85]. These computational algorithms rely on repeated random sampling to obtain numerical results, and intend to simulate the time evolution of some process occurring in nature. Stochastic models have been used to study a variety of biological processes including gene expression [39, 100], bacterial chemotaxis [42], and stem cell proliferation [137].

Stochastic models possess inherent randomness, and so the same set of parameter values and initial conditions will lead to an ensemble of outputs. Analysis of the collection of

outputs will then yield a probabilistic characterization of system behavior for a given set of input values. We use the case of chemical kinetics in a well-mixed reaction volume as an illustrative example. To first construct the stochastic model, each species S_i and potential event j in the system is identified. The state of the system $\mathbf{x}(t)$ at any given time t is completely specified by the positions of all molecules, and the rate of transitioning to a new state is dependent only on the current state. Each potential reaction event j is represented by its individual state-change vector ν_j and propensity function $a_j(x)$. The state-change vector ν_j defines the change in the state of the system that occurs as result of the completion of one instance of event j. The state-change vector for a system of N chemical species is defined as:

$$\nu_j = (\nu_{1j}, ..., \nu_{Nj}) \tag{1.2}$$

where ν_{ij} is the change in the molecular population of species S_i. When an event occurs, the state of the system $\mathbf{x}$ is instantaneously changed to state $\mathbf{x} + \nu_j$.

Propensity functions are defined such that $a_j(x)dt$ is equal to the probability of one instance of reaction j occuring in the reaction volume Ω sometime in the infinitesimal interval $[t, t+dt)$. In the case of chemical kinetics, the propensity functions would include all the rate law equations that govern the population of each species over time. The sum of all $a_j(x)dt$ is denoted as the total propensity $a_0(x)$, and each ratio $\frac{a_j(\mathbf{x})}{a_0(\mathbf{x})}$ represents the probability of event j occurring within the next infinitesimal time interval $[t, t + dt)$.

The time evolution of the probability of reaching state $\mathbf{x}$ at time t given that the state at t_0 is $\mathbf{x}_0$ is derived using the laws of probability. The results is the chemical master equation (CME), which is expressed as a partial differential equation (PDE) that can be written as:

$$\frac{\partial P(\mathbf{x}, t|\mathbf{x}_0, t_0)}{\partial t} = \sum_{j=1}^{M} [a_j(\mathbf{x} - \nu_j)P(\mathbf{x} - \nu_j, t|\mathbf{x}_0, t_0) - a_j(\mathbf{x})P(\mathbf{x}, t|\mathbf{x}_0, t_0)] \tag{1.3}$$

Equation 1.3 is only analytically solvable in rare simple cases, and in other cases can even be prohibitively difficult to solve numerically [57]. Also, this equation can rarely be solved for the probability density function of the state vector $\mathbf{X}(t)$, and so instead simulated trajectories of $\mathbf{X}(t)$ vs. t are generated to represent a random sample of $\mathbf{X}(t)$. To do this, a

new probability function $p(\tau,\, j \mid \mathbf{x},\, t)d\tau$ is defined as the probability, given $\mathbf{X}(t) = \mathbf{x}$, that the next reaction j in the system will occur in the infinitesimal time interval $[t + \tau,\, t + \tau + d\tau)$. This function represents the joint probability density fuction of the two random variables τ (time to the next reaction) and j (index of the next reaction). Applying the laws of probability, we are able to derive an expression for this function, which serves as the mathematical basis for the SSA:

$$p(\tau, j|\mathbf{x}, t) = a_j(\mathbf{x})exp(-a_0(\mathbf{x})\tau) \tag{1.4}$$

This expression implies that τ is an exponential random variable with rate $1/a_0(\mathbf{x})$. Throughout the course of a simulation, to determine the value of the time interval τ between successive events and which event j is chosen to occur, two random numbers r_1 and r_2 are drawn from the uniform distribution in the unit interval [0,1] and applied such that:

$$\tau = \frac{1}{a_0(x)} ln(\frac{1}{r_1}) \tag{1.5}$$

$$j = \min_j \{\sum_{j'=1}^{j} a'_j(x) > r_2 a_0(x)\} \tag{1.6}$$

Thus, beginning from an initial time $t = t_0$ and state of the system $\mathbf{x} = \mathbf{x}_0$, the stochastic simulation algorithm (SSA), also known as the Gillespie algorithm [55], can be written as:

1. Evaluate all $a_j(\mathbf{x})$ and their sum $a_0(\mathbf{x})$
2. Generate values for τ and j using Equations 1.5 and 1.6
3. Update the system by replacing $t \leftarrow t + \tau$ and $\mathbf{x} \leftarrow \mathbf{x} + \nu_j$
4. Record $(\mathbf{x}, t)$ as desired and return to Step 1

The SSA is typically executed until either a specific state is reached (e.g., a cell is activated) or a specified end time is reached. By running many independent trajectories with the same parameter values and initial conditions, one can gain information regarding the probability a specific state will be reached after a given amount of time. If all trajectories

obtained using the SSA closely resemble the deterministic ODE trajectory, one can conclude that random fluctuations of small molecule numbers is negligible. If instead there are noticeable differences in the two models, small molecule number randomness is a significant factor and a deterministic approach in modeling would not reflect the true behavior of the system.

1.2.3 Spatially Resolved Systems

A natural extension to the SSA is applied to systems that are not considered well-mixed in the specified system volume. For example, two molecules may have to diffuse appreciable distances to reach each other in order to initiate a molecular reaction [10]. In such cases, the system space can be partitioned into a collection of adjacent lattice sites of equal edge length h. The choice of lattice site size and shape is made to be most appropriate for the system being modeled. For example, the size of a lattice site may be defined to be on the same scale as the size of a typical molecule that occupies it, and an entire eukaryotic cell can be discretized with a hybrid mesh of triangles and tetrahedra [76]. Each individual lattice site is approximated as a well-mixed reaction subvolume, and molecules can hop from one lattice site to adjacent sites with a prescribed kinetic diffusive parameter k_{hop} to model diffusion. The event of hopping from one lattice site to another is included as an additional propensity function, and for square lattice sites the kinetic rate of hopping k_{hop} is related to the diffusion coefficient D_i of species i in the reaction volume Ω by the relation:

$$k_{\text{hop}} = \frac{(2d)D_i}{h^2} \tag{1.7}$$

Where d represents the dimensionality of the system. Alternatively, space can be modeled as continuous rather than discrete. Rather than hopping to a neighboring lattice site, the modeled particle can hop a prescribed distance h in a randomly chosen direction determined by the angle θ selected from a uniform distribution on the interval $[0, 2\pi]$. Whether applying discrete or continuous space, another consideration in these systems is spatial boundary conditions. Regardless of initial starting position, particles in systems of finite system size are often able to reach system boundaries through a series of successive diffusive moves at

relatively small timescales. These events are typically handled by the application of periodic or reflective (hard-walled) boundary conditions at the system boundary.

1.2.4 Studies on Spatiotemporal Behavior in Living Systems

With stochasticity being a common feature in many diverse biological systems, stochastic modeling approaches have been taken to study many observed phenomena including bursty eukaryotic gene expression [120, 149], bistability in bacteriophage infected *E. Coli* [67], bacterial chemotaxis [92, 104], and stem cell proliferation [137]. The spatially resolved extension to the Gillespie algorithm has also been widely used to explore spatiotemporal behavior in living systems. One such study found that rapid rebindings of enzyme molecules to substrate molecules caused by spatio-temporal correlations can speed up the response of a mitogen-activated protein kinase (MAPK) pathway and lead to loss of ultrasensitivity and bistability [135]. Another study looked at the dynamics behind irregular relocations of *Bacillus subtilis* Soj proteins from nucleoid to nucleoid [34]. From spatial modeling, it was shown that the irregularity may be due to the stochastic nature of the underlying Spo0J/Soj interactions and diffusion. Heterogeneity in embryonic stem cell differentiation was explained in a recent study by Sturrock et. al [133]. A spatial stochastic model of the Hes1 gene regulatory network was able to reproduce the variability in Hes1 oscillations seen in experiments and led to the conclusion that intrinsic noise is the main driving force for the observed heterogeneity in cell differentiation response.

Employing the Gillespie algorithm in the well-mixed or spatially resolved regime, we can model a wide array of biological processes that involve any combination of biochemical reactions, diffusion, active transport, binding and unbinding interactions, molecular recruitment, endocytosis, etc. Through systematic variation of model parameters, we can characterize system behavior under a variety of conditions. By studying multiple biological systems, we are able to gain broad insight regarding the spatiotemporal effects of kinetic transport and network topology in living systems.

1.3 Outline of Thesis

In this thesis, we use computational methods to characterize the behavior of three distinct biological systems that involve spatiotemporal effects of transport and network topology:

1. A simple biochemical reaction network with positive feedback (Ch. 2).
2. Molecular motors on a cytoskeletal network of actin filaments (Ch. 3).
3. Cell division proteins organizing on the cytokinetic ring (Ch. 4).

In each project, biologically relevant kinetic parameters and reasonable conditions are employed to simulate the spatiotemporal dynamics of a living system. Systematic variation of select parameters and conditions reveal nontrivial coupling with emergent system behavior.

1.3.1 Confinement and Diffusion in a Reaction Network with Positive Feedback (Chapter 2)

Positive feedback is a common feature in signal transduction networks and can lead to phenomena such as bistability and signal propagation by domain growth. Physical features of the cellular environment, such as spatial confinement and the mobility of proteins, play important but inadequately understood roles in shaping the behavior of signaling networks. Here, we use stochastic, spatially resolved kinetic Monte Carlo simulations to explore a positive feedback network as a function of system size, system shape, and mobility of molecules. We show that these physical properties can markedly alter characteristics of bistability and stochastic switching when compared with well-mixed simulations. Notably, systems of equal volume but different shape can exhibit qualitatively different behavior under otherwise identical conditions. We show that stochastic switching to a state maintained by positive feedback occurs by cluster formation and growth. Additionally, the frequency at which switching occurs depends nontrivially on the diffusion coefficient, which can promote or suppress switching relative to the well-mixed limit. Taken together, the results provide a framework for understanding how confinement and protein mobility influence emergent features of the positive feedback network by modulating molecular concentrations, diffusion-influenced rate parameters, and spatiotemporal correlations between molecules.

1.3.2 First Passage of Molecular Motors on Networks of Cytoskeletal Filaments (Chapter 3)

Molecular motors facilitate intracellular transport through a combination of passive motion in the cytoplasm and active transport along cytoskeletal filaments. Although the motion of motors on individual filaments is often well characterized, it remains a challenge to understand their transport on networks of filaments. Here, we use computer simulations of a stochastic jump process to determine first-passage times (FPTs) of a molecular motor traversing an interval containing randomly distributed filaments of fixed length. We characterize the mean first-passage time (MFPT) as a function of the number and length of filaments. Intervals containing moderate numbers of long filaments lead to the largest MFPTs with the largest relative standard deviation; in this regime, some filament configurations lead to anomalously large FPTs due to spatial regions where motors become trapped for long periods of time. For specific filament configurations, we systematically reverse the directionality of single filaments and determine the MFPT of the perturbed configuration. Surprisingly, altering a single filament can dramatically impact the MFPT, and filaments leading to the largest changes are commonly found in different regions than the traps. We conclude by analyzing the mean square displacement of motors in unconfined systems with a large density of filaments and show that they behave diffusively at times substantially less than the MFPT to traverse the interval. However, the effective diffusion coefficient underestimates the MFPT across the bounded interval, emphasizing the importance of local configurations of filaments on first-passage properties.

1.3.3 Protein Organization Along the Actomyosin Ring During Cytokinesis (Chapter 4)

Cytokinesis is the final step in cell division and is essential in regulating cell growth and development. In eukaryotes, this process involves the assembly of an actomyosin ring followed by a maturation period prior to constriction. While it is known that a homogeneous spatial distribution of key proteins on the ring is necessary to ensure proper concentric constriction, the mechanism by which these proteins arrange themselves on the ring is

not well understood. Here, we introduce two distinct models of protein organization on the actomyosin ring and use computer simulations to characterize emergent behavior. In the first model, a positive feedback circuit was implemented along with lateral diffusion and protein exchange between the ring and a bulk cytoplasmic pool via association and dissociation reactions and endocytosis. It was found that positive feedback was necessary to establish polarity in protein distribution, and clustering is suppressed by endocytosis and fast diffusion. Clustering analysis via the spatial descriptive statistic of the Ripley's K function revealed that an increase in feedback strength does not necessarily lead to an increase in protein clustering. In the second model, groups of proteins associate to the ring at fixed rate via endocytic patches. After association, they laterally diffuse and engage in binding and unbinding interactions, but don't dissociate for the duration of the maturation period. We found that fast diffusion and weak binding promote homogeneous protein distributions on the ring while slow association of patches containing large number of molecules lead to spatial heterogeneity. Our results suggest that even distributions of proteins on the ring may rely on frequent association of small-sized protein clusters.

Chapter 2

Confinement and Diffusion in a Reaction Network with Positive Feedback

Summary: This chapter is based on the published paper [103]:

Mlynarczyk, Paul J., Pullen III, Robert H., and Abel, Steven M. *Confinement and diffusion modulate bistability and stochastic switching in a reaction network with positive feedback*. Journal of Chemical Physics, 144(1):015102, 2016.

2.1 Introduction

Cells detect environmental stimuli by means of membrane receptor proteins that bind external ligands. Resulting cellular responses are controlled by signal transduction processes that involve the modification of intracellular molecules via biochemical reaction networks. In cellular environments, stochastic effects in the reaction networks are often important due to small numbers of molecules involved and fluctuations in the intracellular and extracellular environments [17, 43]. Additionally, both the shape of the region in which the reactions take place and the mobility of reactants can significantly influence the emergent properties of the reaction networks. For example, recruitment of proteins to the membrane leads to a number of important physical changes, such as increased effective concentrations, decreased mobility,

and altered spatiotemporal correlations between molecules [1, 135]. The role of geometry and diffusion in modulating signaling networks has received relatively little attention, yet may play an important role in structures such as membrane nanotubes (quasi-1D) [108], membranes (2D) [1, 6, 37, 69, 115], organelles (spatially confined) [18], the space between the nucleus and plasma membrane (moderately confined in some cell types) [107], complex fabricated environments [29], etc.

Biochemical reaction networks commonly contain network motifs that exhibit specific patterns of activation and inhibition among interacting molecular species. These motifs can play a critical role in regulating the dynamics and steady states of networks [5, 22, 80, 141]. Positive feedback is a common motif that is characterized by interactions in which the activation of a particular species further enhances its activation. Positive feedback can give rise to bistability, in which a system can reside in one of two stable steady states. This behavior is useful as the two states can be associated with a binary (on or off) response [46]. Bistability is an important feature of numerous cell signaling networks involving binary decisions, including those that regulate cell division and proliferation, apoptosis, and immune cell activation [30, 44, 111, 140]. In bistable networks, external perturbations (such as ligands that bind to protein receptors) can bias the network toward one of the steady states, thus allowing the network to act as a switch. The network confers memory of the perturbation, since the state will persist even after the perturbation is removed [56].

Bistable networks can also switch between states by means of spontaneous stochastic fluctuations. Stochastic switching can lead to phenotypic diversity in an otherwise identical population of cells, and it can also lead to unwanted cell behavior such as the accidental activation of immune cells [128]. Understanding stochastic switching in many cellular systems requires an understanding of stochastic chemical kinetics as well as the role of space and diffusion. For example, previous studies have shown a nontrivial interplay between spatial clustering of active molecules and subsequent propagation of an active domain in positive feedback networks [31, 68, 77, 83, 153]. Nontrivial coupling of spatial structure and chemical kinetics, along with more conventional modifications such as the diffusion influence of kinetic parameters, make stochastic switching in bistable systems an interesting physical problem with importance in cell biology.

There is no general framework for understanding the role of geometry and diffusion in signal transduction networks [1, 18]. Valuable insight can be gained through the study of reaction-diffusion models of simple reaction networks [134, 138]. In this study we use computational methods to investigate the effects of space and diffusion on a two-component positive feedback network that exhibits bistability. We use kinetic Monte Carlo computer simulations to generate simulation trajectories consistent with the reaction-diffusion master equation describing the spatiotemporal dynamics. We also analyze deterministic descriptions of the dynamics to complement the stochastic results [8, 73]. The organization of the paper is as follows: We first introduce the network and the simulation approach. We then compare the system in the well-mixed limit to spatially resolved simulations. Characteristics of bistability and stochastic switching are explored by systematically varying the system geometry and molecule mobility. We then study fixed-volume systems of varying shape and perturb the inactive state with localized pulses of active molecules to investigate switching to the active state. We conclude by discussing how the underlying physical constraints imposed by confinement, system shape, and diffusion influence the behavior of the positive feedback network.

2.2 Methods

We consider a two-component reaction network with positive feedback:

$$A \underset{k_2}{\overset{k_1}{\rightleftharpoons}} X$$
$$A + 2X \underset{k_4}{\overset{k_3}{\rightleftharpoons}} 3X$$

This network is relatively simple yet exhibits the key feature of systems with positive feedback: The presence of active molecules (denoted by X) further enhances the production of active molecules. This network and similar variants have been used widely to explore bistability [52, 145]. We use rate constants that give dynamical responses on biologically relevant time scales and that support bistability. These rate constants are summarized in Table 2.1. The third-order rate constants k_3 and k_4 are defined for three-dimensional

Table 2.1: Bistable kinetic parameters

Parameter	Description	Value
k_1	unimolecular forward rate constant	0.05 s^{-1}
k_2	unimolecular reverse rate constant	40 s^{-1}
k_3	trimolecular forward rate constant	5×10^{-8} $\mu m^6 s^{-1}$
k_4	trimolecular reverse rate constant	1×10^{-8} $\mu m^6 s^{-1}$

volumes. We adopt the language that the active species is X and the inactive species is A. Thus an active state is one that contains many X and few A molecules whereas an inactive state is one that contains few X and many A molecules. Note that a system governed only by the first-order reactions would have an average steady state ratio of A to X molecules given by $k_2/k_1 = 800$. The third-order reactions allow the system to reach large numbers of X molecules when the total concentration is sufficiently large.

We seek to explore the spatial and temporal dynamics of the positive feedback network as a function of system size, system shape, and mobility of molecules. We employ a slab-like geometry to study the effects of system shape and confinement. Initially, the effect of confinement is explored by fixing the total number of molecules in a simulation box of size 1 μm $\times 1$ μm $\times L$. Two sides are held at fixed length, while L, which we call the confinement length, is systematically varied. The total population is 10^4 molecules. Unless otherwise noted, initial configurations are obtained by placing the molecules uniformly at random. To investigate the effect of system shape without changing molecular concentration, we perform additional simulations using various system shapes of equal volume. The diffusion coefficient is systematically varied to study the effects of protein mobility.

We consider discrete-space, continuous-time stochastic dynamics. The time evolution of the system is governed by a reaction-diffusion master equation. Space is discretized into a cubic lattice with lattice spacing $a = 0.01$ μm. Multiple molecules are allowed to occupy a single site, reactions occur only between molecules occupying the same lattice site, and each lattice site is modeled as a well-mixed reaction volume. Diffusion is modeled by

allowing molecules to hop to nearest neighbor lattice sites at a rate specified by the diffusion coefficient. Periodic boundary conditions are employed. At any given time, the positions of all molecules completely specify the state of the system. We use the Gillespie algorithm to generate stochastic simulation trajectories consistent with the reaction-diffusion master equation [57].

Simulation trajectories are generated using the standard stochastic simulation algorithm, with reaction rates defined as follows [57]. Consider a well-mixed volume (V_i) containing n_X X molecules and n_A A molecules. The reaction volume corresponds to a single lattice site in the spatially resolved case and the entire system in the well-mixed case. The propensity (rate) of each reaction within the volume is given by

$$
\begin{aligned}
a_1(n_A) &= k_1 n_A \\
a_2(n_X) &= k_2 n_X \\
a_3(n_A, n_X; V_i) &= \tilde{k}_3 n_A \frac{n_X(n_X-1)}{2} \\
a_4(n_A, n_X; V_i) &= \tilde{k}_4 \frac{n_X(n_X-1)(n_X-2)}{6}
\end{aligned}
$$

We have defined $\tilde{k}_i = k_i/V_i^2$. The rate at which a molecule hops to a particular neighboring lattice site is given by D/a^2. In the limit of large D, spatial degrees of freedom become irrelevant and the system is assumed to be well mixed. We distinguish between well-mixed and spatially resolved stochastic simulations by referring to them as as either "stochastic, well-mixed" or "stochastic, spatially resolved" in the results that follow.

We are interested in probing whether the system exhibits bistability. In the spatially resolved system, it is difficult to know a priori whether a system will be bistable, and if so, the relative population of each steady state. To test for bistability, we consider two different initial states that bias the system toward different steady states if the system is bistable: Starting with all A molecules targets the inactive state, while starting with all X molecules targets the active state. If the system is monostable, both sets of initial conditions converge to the same state.

2.3 Results

2.3.1 Bistability in the well-mixed regime

We begin by characterizing bistability and stochastic switching in the well-mixed limit. Here, changing the confinement length L changes the volume of the system, with decreasing L leading to increased concentration. In the positive feedback network, the first two reactions are first order, and thus are not affected by the system volume. The third and fourth reactions, which are third order and encompass the positive feedback effect, demonstrate a strong dependence on volume. This is illustrated by the ordinary differential equations (ODEs) associated with deterministic well-mixed kinetics, in which these terms involve a product of three terms (written in terms of discrete molecular populations):

$$\frac{dN_A}{dt} = -\frac{dN_X}{dt} = -k_1 N_A + k_2 N_X - \frac{\tilde{k}_3}{2} N_A N_X (N_X - 1) + \frac{\tilde{k}_4}{6} N_X (N_X - 1)(N_X - 2) \quad (2.1)$$

Here, $\tilde{k}_3 = k_3/V^2$ and $\tilde{k}_4 = k_4/V^2$, where V is the system volume. Thus, it is expected that decreasing L, and hence decreasing V, will increase the relative importance of the third and fourth reactions. Smaller L is expected to promote an active state.

Figure 2.1 demonstrates the effect of confining the system with a fixed total number of molecules. The deterministic description given by Eqn. 2.1 yields the steady state results shown in the figure, with behavior spanning a monostable (active) regime for small L, a bistable regime for intermediate L, and a monostable (inactive) regime for sufficiently large L. Stochastic, well-mixed simulations were conducted at values of L corresponding to integer multiples of the lattice spacing. For each value of L and for each initial condition (either all A or all X), we generated 1000 independent trajectories of duration 100 s. The mean inactive and active steady state values obtained from the stochastic simulations are in close agreement with the deterministic solutions. The stochastic results in Fig. 2.1B again illustrate the presence of monostable regimes at both sufficiently small and sufficiently large system volumes, with bistability present at intermediate volumes. From a physical standpoint, at $L = 0.01$ μm, the concentration of X due to the first-order reactions is

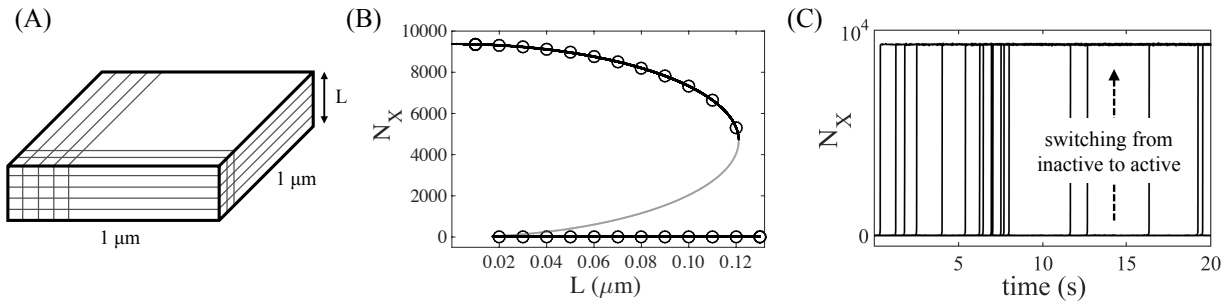

Figure 2.1: (A) Schematic of the system geometry. (B) Behavior of the reaction network in the well-mixed limit. The bistable regime is present at intermediate values of L. Steady state solutions of the deterministic well-mixed equations are shown as black lines (stable states) and a grey line (unstable state). Results from stochastic simulations (circles) demonstrate bistability at values of L between 0.02 and 0.12 μm. The standard deviation is smaller than the symbols for each case. Stochastic switching was observed only for $L = 0.02$ μm (from the inactive to active steady state) and is attributed to the inactive state being close to the unstable steady state. (C) Well-mixed, stochastic simulation trajectories starting from the all-A initial condition for $L = 0.02$ μm. Multiple simulation trajectories are shown, and each near-vertical line represents a transition to the active state for a different trajectory. Stochastic switching is observed only for this value of L in the well-mixed regime.

sufficiently large so that a small number of X molecules can significantly engage the third-order reactions that produce additional X molecules. As these reactions occur, the X population increases, which in turn increases the propensity associated with the third-order reaction producing additional X molecules. This effectively engages the positive feedback loop and quickly leads the system to the active state.

In the well-mixed stochastic simulations, we observe stochastic switching only at $L = 0.02$ μm, with switching occurring from the inactive state to the active state (Fig. 2.1C). Typically, the stochastic switching studied here involves at most a single switching event per trajectory. This is in contrast with some studies in which a single trajectory switches between states many times [4]. At the confinement length of $L = 0.02$ μm, in the deterministic case the inactive steady state lies close to the unstable steady state. Thus, stochastic fluctuations in the number of X molecules for a system in the inactive steady state can readily exceed the number of X molecules associated with the unstable steady state and enter the basin of attraction for the active state. The standard deviation in the number of molecules in the active state increases as L increases, indicating larger fluctuations in numbers of active molecules at larger volumes. However, even at $L = 0.12$ μm, we do not observe stochastic

transitions from the active to the inactive state since the characteristic number fluctuations are small compared with the difference in the number of X molecules in the active and unstable steady states. Stochastic switching from the active to inactive state is observed only in a narrow range of L near the transition from bistable to monostable behavior that occurs at $L \approx 0.1211$ μm.

2.3.2 Confinement and diffusion in spatially resolved systems

We now consider spatially resolved stochastic simulations to probe the impact of confinement and mobility on the positive feedback network. We generate stochastic simulation trajectories for various values of the confinement length (L) and the diffusion coefficient (D). For each pair of values, we generate 25 independent trajectories of duration 5 s for each initial condition (all X and all A). This time is sufficiently long to assess whether the system is bistable, noting that in the well-mixed, monostable activate state ($L = 0.01$ μm), trajectories starting with all A molecules reach the active state within 0.2 s.

Figure 2.2 shows individual simulation trajectories for conditions that give bistable behavior in the well-mixed regime. It is immediately evident that changing the diffusion coefficient can lead to qualitatively different behavior from the well-mixed case. For example, sufficiently slow diffusion at the larger values of L abrogates bistability and leads to a monostable, inactive state. When bistability is present, increasing the diffusion coefficient monotonically increases the average number of X molecules in the active steady state. Stochastic switching is clearly evident in the systems with $L = 0.02$ μm and $L = 0.03$ μm. Both systems exhibit behavior in which the average waiting time before switching occurs is nonmonotonic in D. Within the bistable regime, switching is infrequent at small D and initially becomes more frequent as D increases. However, switching in the well-mixed regime is again relatively infrequent, implying that at sufficiently large D the average waiting time before switching occurs increases. This observation is explored in more detail later, when we discuss spatiotemporal aspects of the switching event, which occurs by the growth of a cluster of active molecules.

Figure 2.3 summarizes the behavior of the positive feedback network for a range of parameters, with cases characterized as monostable or bistable. At some conditions,

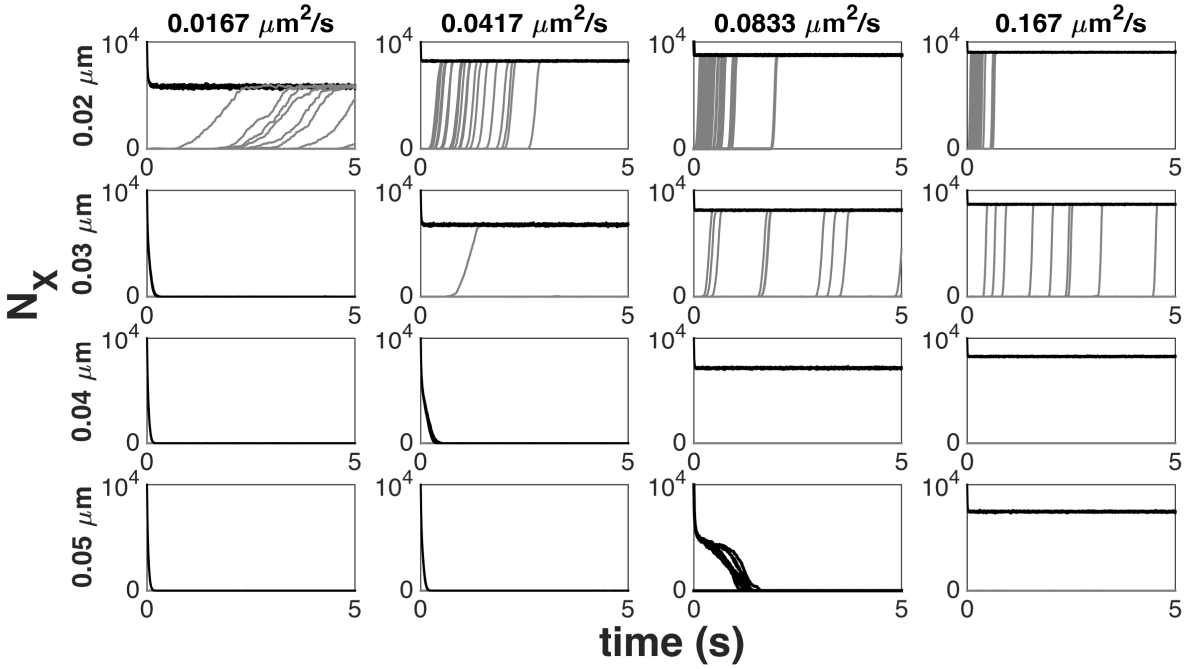

Figure 2.2: Representative trajectories for various system sizes and diffusion coefficients. Each plot displays 25 trajectories from each initial condition (all A in grey and all X in black). The average number of X molecules in the inactive state is small, and due to the vertical scale, trajectories in the inactive state appear coincident with the horizontal axis. Increasing the diffusion coefficient (D) leads to larger numbers of X molecules in the active state. At larger values of the confinement length, larger values of D are required to achieve the active state.

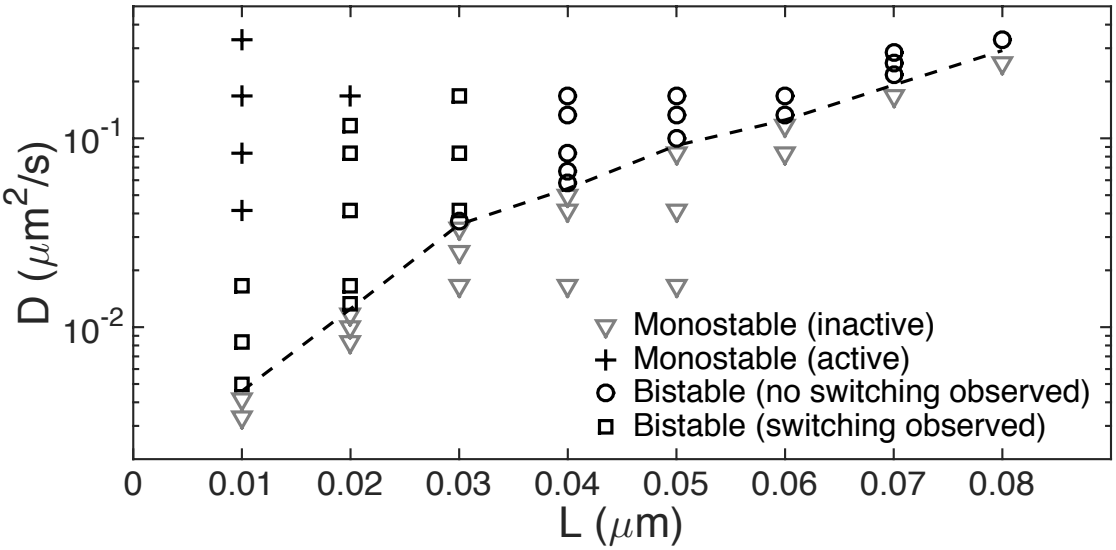

Figure 2.3: Bistability diagram for the spatially resolved system. Results are obtained using stochastic, spatially resolved simulations and summarize behavior of the system at fixed number of molecules as a function of the confinement length (L) and the diffusion coefficient (D). The active state is promoted by small values of L (high concentration) and large values of D (high mobility). For each value of L, there exists a value of D below which the system is inactive (monostable). The dashed line illustrates the approximate transition line between the monostable inactive regime and a regime in which the active state is stable. In the parameter regime displayed in the figure, stochastic switching is observed only at smaller values of L, as the observed mechanism of cluster formation and growth is promoted by increased concentration and intermediate diffusion coefficients.

distinguishing between bistable and monostable behavior can be difficult because trajectories starting in one steady state rapidly switch to the other steady state. With limited simulation data, it can be difficult to distinguish this from a monostable case. To call a system bistable, we require that some trajectories must reside around a plateau value (associated with a steady state) for at least 0.3 s before initiating a switching event. This is longer than the maximum time observed for a transition to the active state in well-mixed stochastic trajectories at $L = 0.01$ μm, and thus provides a useful heuristic for identifying bistable systems.

More confined systems with larger values of D promote the active state. Confining the system with a fixed number of molecules increases the concentration and thus promotes the reactions involved in positive feedback. This has the effect of promoting the active state, as in the well-mixed case. Diffusion plays an important role by influencing encounter times between molecules initially on different lattice sites. Encounter times are also affected

by concentration and system geometry, which affect the distribution of distances between molecules. At sufficiently slow diffusion, decreased encounter times can lead to decreased effective kinetic rates, which are often called diffusion-influenced parameters. Analytical approaches to calculating diffusion-influenced kinetic parameters are technically difficult and have been limited to simple reaction schemes in infinite spatial domains [87, 134, 138]. As such, computer simulations provide an essential tool for understanding the effect of diffusion in more complicated systems.

At small values of the diffusion coefficient, there is insufficient mixing to sustain the positive feedback reaction, and the system is monostable and inactive (corresponding to the region below the dashed line in Fig. 2.3). It is instructive to consider the limiting case of $D \to 0$, in which molecules do not move from their initial position on the lattice. In the most confined case ($L = 0.01$ μm), there is one molecule per lattice site on average. If we assume the number of molecules at each site is distributed according to a Poisson distribution, then with an average occupancy of 1 the fraction of sites having three or more molecules is approximately 0.08. Thus, finding three or more molecules on a single lattice site is relatively rare even in the most concentrated case and most molecules are governed solely by first order reaction kinetics. Additionally, starting from the master equation for a fixed number of molecules in a well-mixed volume, the steady state probability distribution of X molecules can be solved exactly. This calculation is detailed in Appendix A. At least six molecules must be present on a lattice site for a greater than 2% probability that at least one X molecule is present. Thus for immobile molecules, the expected number of X molecules is small and consistent with an inactive state.

The transition from the monostable inactive regime to the bistable regime in Fig. 2.3 occurs at larger D as L increases. This is a consequence of molecules having to diffuse farther on average to encounter one another. Within the bistable regime, there is a nontrivial interplay between diffusion and stochastic switching. In particular, as illustrated in Fig. 2.4, switching from the inactive to active state occurs by the growth of a cluster of X molecules. The two trajectories shown are representative of all stochastic switching events observed from the inactive to active state. The cluster growth mechanism is also observed in transitions

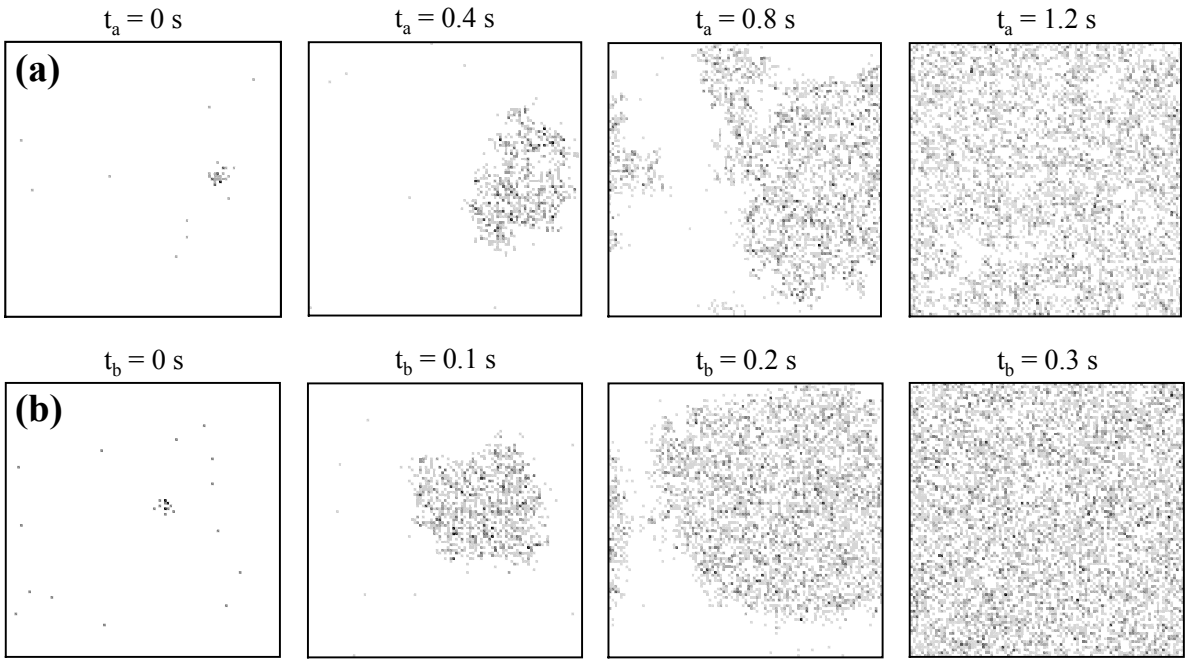

Figure 2.4: Representative spatial snapshots of stochastic switching events. Snapshots from two trajectories show the spatial distribution of X molecules (grey) during a stochastic transition to the active state. A single active cluster is formed and then grows in size (the approximate formation time is defined as $t_i = 0$). Analogous behavior is observed in other trajectories that switch from the inactive to active state. **(A)** 1 μm $\times$ 1 μm $\times$ 0.01 μm with $D = 0.00833$ $\mu\text{m}^2/s$. **(B)** 1 μm $\times$ 1 μm $\times$ 0.02 μm with $D = 0.0417$ $\mu\text{m}^2/s$. The images are two-dimensional projections of the system.

from the initial condition with all A to the active state in the cases characterized as monostable (active).

Within the bistable regime, stochastic switching is relatively infrequent at small values of the diffusion coefficient, as molecules have a limited range of interaction and are influenced by other molecules in small, effectively local domains. The size of the domain is a single lattice site as $D \to 0$, and can be thought of as the volume accessible to an isolated X molecule before it transitions to an A molecule (since X molecules serve to initiate positive feedback). Within small domains, relatively large effective concentrations are needed to promote the active state. We discuss this quantitatively in Appendix A using the exact steady state solution of the chemical master equation. Thus, large and relatively rare localized fluctuations in concentration are needed to nucleate a cluster of active molecules. Hence, switching is slow, as nucleation of an active domain is needed before it can spread in space. As

the diffusion coefficient increases, X molecules can sample larger effective volumes that are still small compared with the system size. In Appendix A.2, we show how the concentration required to activate a domain depends on the domain size, and we use this to determine an approximate value of D at which stochastic switching becomes likely. Faster diffusion is required to promote switching at larger values of L.

As D increases further, molecules eventually interact over a substantial fraction of the system volume and the system approaches a well-mixed state. As is seen in Fig. 2.1B, within the bistable regime, the steady states become well-separated relative to typical number fluctuations. Localized fluctuations of X molecules are rapidly dissipated, and growth of localized domains no longer promotes activation. Taken together, these physical reasons underlie the non-monotonic average switching time as a function of D within the bistable regime: (i) at small D, the small effective range of interactions requires large effective local concentrations for activation, (ii) at intermediate D, interactions in moderate-sized domains promote the formation of spatially-localized clusters of active molecules that then spread in space, and (iii) at large D, the large number of molecules in the well-mixed limit stabilizes each steady state and suppress switching.

2.3.3 System shape influences stochastic switching at fixed concentration

In the previous sections, changing the system shape also changed the concentration of molecules. Here we investigate changes in system shape while keeping the number of molecules and system volume constant. Thus, these results probe a purely geometrical effect of the environment. We focus on a specific case with $D = 0.0833\ \mu\text{m}^2/s$ and a volume of $0.04\ \mu\text{m}^3$. This corresponds to the system studied in Figs. 2.2 and 2.3 with $L = 0.04\ \mu$m, which is bistable in the slab geometry with no observed stochastic transitions. Changing the shape of a system with fixed volume can generate systems with markedly different degrees of confinement (examples include a one-dimensional line of lattice sites, a two-dimensional array of lattice sites, and a nearly cubic domain). We find that systems of dimensions 400 μm $\times$ 0.01 μm $\times$ 0.01 μm and 2 μm $\times$ 2 μm $\times$ 0.01 μm are monostable and inactive, even

though they have the same concentration as the slab geometry with $L = 0.04$ μm. These geometries highlight an important feature associated with molecular transport and encounter times. The expected time for a molecule to diffuse across the longest dimension of the system scales as $\tau \sim \xi^2/D$, where ξ denotes the distance. In the two-dimensional system this gives $\tau_2 \sim 50$ s and in the one-dimensional system it gives $\tau_1 \sim 2 \times 10^6$ s, highlighting markedly different timescales.

In the examples above, purely one- and two-dimensional systems exhibit monostable behavior while a less confined system exhibits bistability. This indicates that system geometry alone can control the steady state behavior of the network. To further probe the effect of geometry on stochastic switching, we consider an initial condition with mostly A molecules and a small number of clustered X molecules. The A molecules are distributed uniformly at random and the X molecules are localized at a single lattice site. We refer to this as a pulse of X molecules. Biologically, this is representative of a localized stimulus (such as a receptor bound to a ligand) that locally activates a number of molecules. Figure 2.5A shows the fraction of trajectories that switch to the active state as a function of the number of X molecules in the pulse. The number of X molecules required to activate the system depends on system shape, with less confined systems requiring larger pulses to initiate switching. Distributing the initial pulse of X molecules over a slightly larger domain does not substantially change the results. Fixing the number of X molecules and increasing the spatial extent of the pulse eventually decreases the likelihood of switching (see Fig. 2.5B).

Two physical mechanisms contribute to the observations in Fig. 2.5. The first is that changing the distribution of distances between molecules affects the diffusion-influenced rates. This is reflected by the average number of X molecules in the active steady state: More confined systems have smaller numbers of X molecules (see Fig. 2.5 caption for details). This has the effect of making the active steady state easier to reach from the inactive state in the more confined systems. The second mechanism is that confinement helps to keep the pulse of X molecules spatially localized, since there are fewer degrees of freedom by which molecules can diffuse away. This has the effect of sustaining clusters of X molecules for a longer period of time. In less confined systems, X molecules originating in a pulse may diffuse away more easily, thus reducing the likelihood of nucleating growth of an active

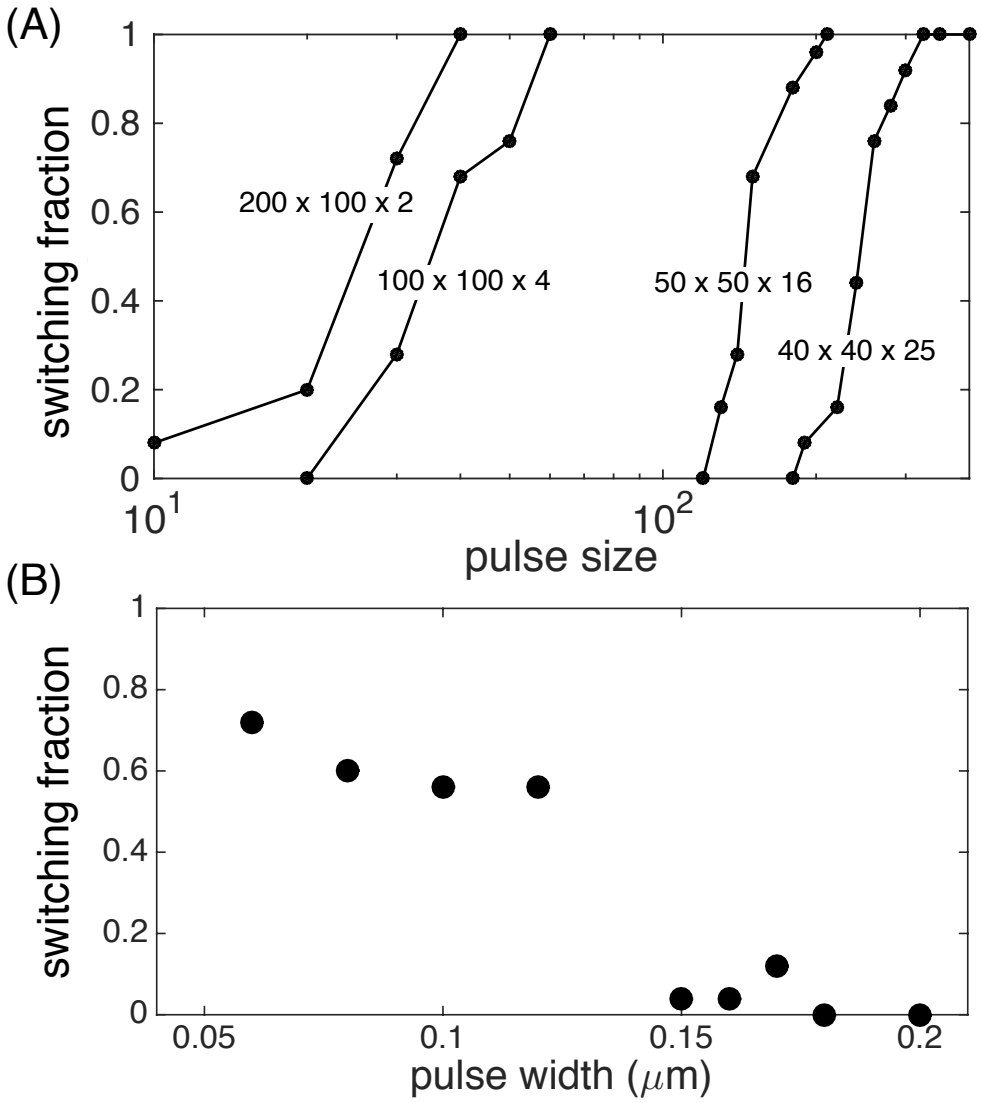

Figure 2.5: (A) Likelihood of switching as a function of pulse size (number of X molecules) at fixed total concentration. Trajectories are generated using stochastic, spatially resolved simulations with a pulse of X molecules initially localized within a single lattice site and the remaining molecules inactive and randomly distributed throughout the system. Results are shown from simulations in four different geometries (described by the number of lattice sites in each dimension of the simulation box). The switching fraction is calculated using 25 trajectories. Each case considered exhibits bistability, and less confined systems require larger pulses to induce switching. From left to right, the active steady state contains on average the following number of X molecules: 6766, 7098, 7178, and 7179. (B) Likelihood of switching as a function of the linear size of a pulse in stochastic, spatially resolved simulations. The initial number of X molecules is fixed at 48 and the spatial extent of the pulse is varied. The switching fraction for a slab geometry with $L = 0.04$ μm is calculated using 25 trajectories. The X molecules are initially uniformly distributed within a region with dimensions l μm $\times$ l μm $\times$ 0.04 μm, where l denotes the pulse width.

domain by positive feedback. Similarly, if diffusion is too fast, pulses of X molecules will dissipate rather than propagate as a growing cluster.

2.3.4 Fast diffusion suppresses pulse-induced switching in the bistable regime

Here we investigate how switching to the active state depends on sustaining the spatial localization of a cluster, but without complications arising from the diffusion-influence of kinetic parameters. To do this, we consider the partial differential equations (PDEs) governing the deterministic evolution of molecular concentrations:

$$\frac{\partial C_X}{\partial t} = D\nabla^2 C_X + k_1 C_A - k_2 C_X + \frac{\hat{k}_3}{2} C_A C_X^2 - \frac{\hat{k}_4}{6} C_X^3$$
$$\frac{\partial C_A}{\partial t} = D\nabla^2 C_A - k_1 C_A + k_2 C_X - \frac{\hat{k}_3}{2} C_A C_X^2 + \frac{\hat{k}_4}{6} C_X^3$$

We specifically consider the slab geometry with $L = 0.04$ μm and assume the system is well-mixed in the narrow dimension only. Then $C_X = C_X(x, y, t)$ is a two-dimensional concentration and $\hat{k}_i = k_i/L^2$ is the appropriate rate parameter for two dimensions. Note that there is no effect of diffusion on the kinetic rates and that the system shape does not affect the steady state concentrations. Solutions are obtained numerically using a finite difference scheme. As before, we consider the effect of starting with a spatially localized pulse of X molecules with all other molecules inactive and spatially homogeneous. Figure 2.6 shows the concentration of X molecules within the pulse needed to transition to an active state as a function of the linear size of a pulse. Highly localized pulses and larger diffusion coefficients require larger concentrations in order to reach the active steady state. Confining the system in an additional dimension further decreases the concentration needed for a pulse of a particular linear size. This is consistent with stochastic simulations, in which decreased diffusion coefficients can (i) destabilize the active steady state due to decreased diffusion-influenced parameters and (ii) promote active domain formation by sustaining X interactions at the site of a pulse of molecules.

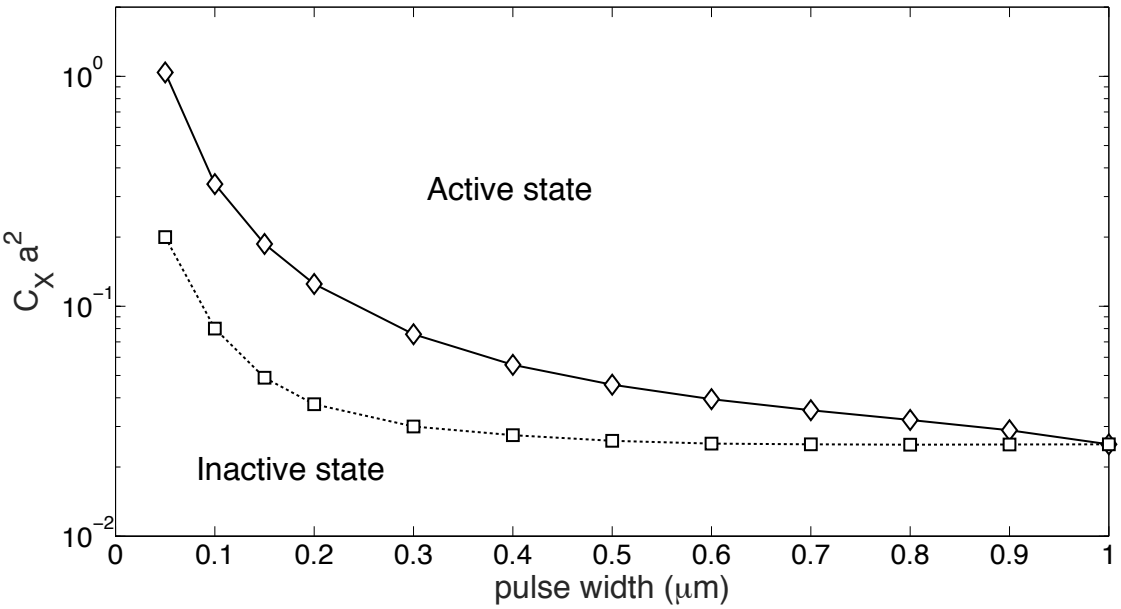

Figure 2.6: Pulse concentration required for activation. Numerical solutions to the deterministic, spatially resolved PDEs are obtained for various pulse widths and concentrations (C_X), with the long-time behavior characterized as active or inactive. Lines mark the transition from inactive to active final states for $D = 0.0833\ \mu\text{m}^2/s$ (squares, lower) and $D = 0.833\ \mu\text{m}^2/s$ (diamonds, upper). A square pulse of a given width requires a concentration higher than the transition line in order to activate the system. Note that $C_X a^2$ measures the number of molecules in a projected area the size of a single lattice site in the stochastic simulations.

2.4 Discussion

We used stochastic computer simulations to explore a simple two-component network with positive feedback as a function of system size, system shape, and protein mobility. These physical features are important in many biological contexts. For example, membranes are often associated with changes in confinement and diffusion: Membrane-associated proteins diffuse slowly in an effectively two-dimensional environment and membranes can confine cytoplasmic reactants within small vesicles [107, 115]. The stochastic switching studied here is typically unidirectional, with one steady state having a higher relative stability than the other [48]. Biological examples of rare stochastic switching include spurious immune cell activation [60], decisions in developmental pathways [94], and changing stem cell lineage commitment [41].

The positive feedback network studied here exhibits feedback-mediated bistability, and it additionally exhibits a clustering mechanism whereby spatially localized active molecules form a self-sustaining and growing domain. This mechanism is observed in other biologically-inspired networks of varying complexity and can be viewed as a generic feature of the network topology [31, 68, 77, 83, 153]. Thus, we expect the physical mechanisms explored in this study to be relevant to a broad class of positive feedback networks, given that they support bistability and have sufficiently slow diffusion to allow active domain formation. We have identified various mechanisms by which the physical features of the system affect bistability and stochastic switching in the positive feedback network:

Steady state behavior. Confining a system with a fixed number of molecules increases the concentration of molecules and hence promotes positive feedback through mass-action effects. This is reflected in the well-mixed and spatially resolved simulations. However, spatially resolved systems are also influenced by the mobility of molecules and the shape of the system. Changing the diffusion coefficient affects steady state behavior by modulating effective kinetic rates and altering spatiotemporal correlations. At slow diffusion, reaction rates (higher than first order) are effectively reduced because of increased time between molecular encounters. Additionally, once molecules are close together in space, they are more likely to stay in close proximity for a longer time. Changing the shape of the system

alters the distribution of distances between molecules, with more confined systems (at fixed concentration) having molecules that are farther apart on average. This affects diffusion-influenced rates since it affects the distribution of encounter times between molecules [1].

Stochastic switching. The concentration of molecules, modified in this work through the confinement length, influences stochastic switching between states in the bistable regime. In the limit of fast diffusion, the likelihood of switching is governed by characteristics of the basin of attraction for each steady state. Interestingly, in the spatially extended system, there is a nontrivial interplay between diffusion, system shape, and spatiotemporal correlations. Both diffusion and system shape modulate stochastic switching by changing properties of the steady states (e.g., by the modulation of effective kinetic rates), which can affect number fluctuations and the regions of state space that act as attractors for each steady state. At sufficiently slow diffusion, the system is inactive due to insufficient mixing of molecules. This can be regarded as an extreme diffusion-influence of kinetic rates. At sufficiently high diffusion coefficients, the system is effectively well-mixed, and there is no spatial structure. However, at intermediate diffusion coefficients, stochastic switching is observed to occur by a mechanism of cluster formation and growth.

Starting from an inactive state, the formation of clusters of active molecules is the result of spontaneous fluctuations in the system. Diffusion plays an important role and can promote or suppress stochastic switching relative to the well-mixed state. Even though the total number of molecules is large, cluster formation is dominated by localized number fluctuations involving small numbers of molecules. Slow diffusion limits the ability of X molecules to interact over large distances, and hence restricts the spatial range over which a spontaneous fluctuation of X molecules must occur. As mobility increases, an active cluster can initially interact over a larger spatial range, yet relatively slow diffusion prevents the molecules from dissipating in space. Sustaining a cluster for a sufficiently long time is necessary to promote cluster growth. At larger diffusion coefficients, even though spontaneously formed X molecules can interact over longer ranges, large diffusion disrupts cluster formation and hence suppresses a local enhancement of positive feedback. This leads to the nonmonotonic average waiting time for switching as a function of the diffusion coefficient. System shape also plays a role by influencing the degrees of freedom by which molecules can diffuse away.

Biological significance. Positive feedback is a common feature in signal transduction networks. Cells often modify the distribution of molecules and their physical shape in response to environmental cues, and hence can modulate properties of the effective environment experienced by a signaling network [87]. This work provides a framework for thinking about the roles of confinement, geometry, and protein mobility in modulating properties of a positive feedback network. Because we have chosen a simple network that captures key features of positive feedback, the results are expected to be relevant to other networks exhibiting positive feedback. This network also suggests the utility of confinement and protein localization in activating a network. For example, recruitment of molecules to the membrane, followed by spatially localized activation, can lead to rapid signaling by propagation of a growing cluster of active molecules. Additionally, compartmentalization within a cell can lead to localized confinement within a particular region such as the nucleus, which can promote the initiation and subsequent spreading of an active signal [66]. The physical mechanisms explored in this work are also expected to play a role in other signal transduction networks.

Chapter 3

First Passage of Molecular Motors on Networks of Cytoskeletal Filaments

Summary: Sections 3.1 - 3.3.6 of this chapter are based on the submitted paper:

Mlynarczyk, Paul J. and Abel, Steven M. (2018) *First passage of molecular motors on networks of cytoskeletal filaments*. Manuscript submitted for publication.

3.1 Introduction

Active intracellular transport is essential for proper cellular function in eukaryotes, with defects resulting in various types of disease [15]. Passive diffusion is often too slow for transport across cellular distances, so biological cargo such as vesicles and organelles are commonly transported via active processes [14, 24, 147]. Active transport is facilitated by molecular motor proteins that bind cargo and generate directed motion along cytoskeletal filaments by converting energy obtained from the hydrolysis of ATP into mechanical work [125, 143, 72, 53]. The cytoskeleton of the cell is comprised of a network of filamentous protein assemblies and serves as a substrate for the movement of motor proteins in the cytoplasm [121, 11]. Individual filaments have a polarity that dictates the direction in which a motor protein moves.

Myosins are a class of molecular motors that travel along actin filaments [156]. The organization of the actin cytoskeleton is controlled by many accessory proteins; commonly,

it can be found arranged in an approximately random configuration, with little correlation between filaments [95, 3]. In traversing a cytoskeletal network, active transport along filaments is interspersed with passive cytoplasmic motion [71]. Although the biophysical properties of many types of myosin motors on single actin filaments have been well characterized [97, 74, 123, 84, 102, 122], the influence of various features of the cytoskeletal network on transport is not as well established.

Experimental and theoretical studies have shown that an actin network of sufficient filament density can effectively transport material, with transport controlled by motors switching from one filament to another rather than by means of spontaneous changes in network structure [93, 129, 96]. Theoretical studies have demonstrated that intermittency in passive versus active transport can increase the efficiency of transport by decreasing the amount of time required to traverse a given intracellular distance [65, 19]. Thus, the spatial organization of the filament network can significantly affect the transport of molecular motors. In addition, the local organization of filaments can have outsized influence on transport over larger length scales in some cases. Experimental and theoretical studies have shown that motors can become trapped at junctions of multiple filaments, leading to unproductive cycling states [126, 9].

In some cases, filaments are capable of arranging in such a way to produce a large degree of spatial heterogeneity in network structure. For instance, bundles of many individual actin filaments are commonly seen in large eukaryotic cells and function to facilitate transport of molecular species and organelles at relatively high speeds [58, 59]. This phenomenon is relevant in many plant organisms such as the aquatic alga *Chara corallina*, which possess exceptionally large intermodal cells that undergo rotational streaming driven by vesicles coated with motor proteins sliding along cables of bundled actin filaments [157]. The presence of these filamentous bundles in a network of otherwise randomly oriented filaments may significantly alter the emergent transport properties in the cell [40].

In the field of stochastic processes, first-passage processes are a class of problems that have been useful in the study of many physical and biological systems [19, 117]. Applications in biology include problems involving molecular search, transcription, channel transport, and

evolution (reviews of biological applications can be found in Refs. [28] and [131]). The first-passage time (FPT) is the time to first reach a specific state (or set of states) starting from a specified initial condition. Because FPTs reflect the underlying stochastic process, they provide a useful way to characterize properties of the process and are often directly related to physical properties of interest. For the case of coupled active and passive motor transport, characterizing FPTs gives insight into the timescales and variability of transport. For the example of a motor crossing an interval, a small mean first-passage time (MFPT) and low variability would represent fast and reliable transport; in contrast, a large MFPT and high variability would represent slow, unreliable transport. In this context, Ando et al. used simulations to characterize the FPTs of motors moving from the nucleus to the cell surface and determined that the MFPT was largely determined by the total length of all filaments in the system [9].

Recent experimental and theoretical work has shown intriguing coupling between motor transport and the structure of the underlying cytoskeletal network [126, 9]. However, much remains unknown about the relationship between configurations of filaments and the large-scale transport of motors [11, 23, 132, 81]. In this work, we use stochastic computer simulations to study the transport of single motors traversing random configurations of filaments. We systematically vary the number and length of filaments and characterize the first-passage times for a motor to traverse an interval of fixed length. We examine the FPT distributions of select cases, investigate the impact of net filament polarity, and determine the MFPT that results from reversing the polarity of all filaments of a given configuration. For specific filament configurations, we assess the impact of individual filaments by reversing their polarity and determining the change in MFPT; we then compare the location of high-impact filaments with regions of space in which motors spend large amounts of time. To further characterize cytoskeletal network transport, we assess whether the transport of a motor across a domain with many filaments can be treated as a diffusive process with an effective diffusion coefficient. We then introduce filamentous bundling and investigate its impact on MFPT and FPT variability. Finally, we characterize motion of motor-organelle complexes and the impact of cytoskeletal traffic in multiple motor systems.

3.2 Methods

A molecular motor is represented as a particle that diffuses, reversibly binds to filaments, and undergoes directed motion when bound to a filament. We consider a single molecular motor as it traverses a two-dimensional rectangular system containing static, fixed-length filaments that are randomly distributed in the system space. The dynamics are described by a continuous-time stochastic jump process.

The system is 20 μm by 5 μm with hard-wall boundary conditions. Filaments are represented as line segments with a fixed directionality for motor motion (we refer to this as the polarity of the filament). The filaments are placed by selecting a random point in the system, extending a line segment of a prescribed length at a random angle, and then assigning a polarity at random. Filaments are truncated if they cross a boundary. The number and length of filaments are both systematically varied. The choice of system size is motivated by plant cells, in which motors often traverse large cellular dimensions ($\sim$ 10 to $\sim$ 100 μm) with a third dimension that is substantially restricted ($\sim$ 1 μm) due to the close proximity of a large vacuole and the cell membrane [146].

When the particle is not bound to a filament, it hops at rate $k_{\text{hop}} = 270\ \text{s}^{-1}$ with a step length of 100 nm in a randomly chosen direction. This gives a diffusion coefficient of $D = 0.675\ \mu\text{m}^2\,\text{s}^{-1}$. When unbound, the motor has a binding rate of $k_{\text{on}} = 6\ \text{s}^{-1}$ with each filament located within 100 nm of the particle. This is the approximate size of a myosin motor. When the motor is bound to an actin filament, it takes 100 nm steps along the filament in the direction prescribed by the filament's polarity. The hops occur at a rate of $k_{\text{fil}} = 60\ \text{s}^{-1}$, giving an average speed of 6 $\mu\text{m}\,\text{s}^{-1}$. The motor unbinds from the filament either spontaneously ($k_{\text{off}} = 2\ \text{s}^{-1}$) or when the end of the filament is reached. The rate constants were chosen to be physiologically relevant and were motivated by *in vitro* experiments with myosin and kinesin [159]. We use the Gillespie algorithm to generate independent stochastic simulation trajectories using various filament network configurations [57].

The primary quantity of interest is the first-passage time (FPT) for the motor to cross the rectangular interval in the longer (20 μm) dimension, starting from one boundary. The motor starts at the center of the boundary in an unbound state, and the simulation runs until

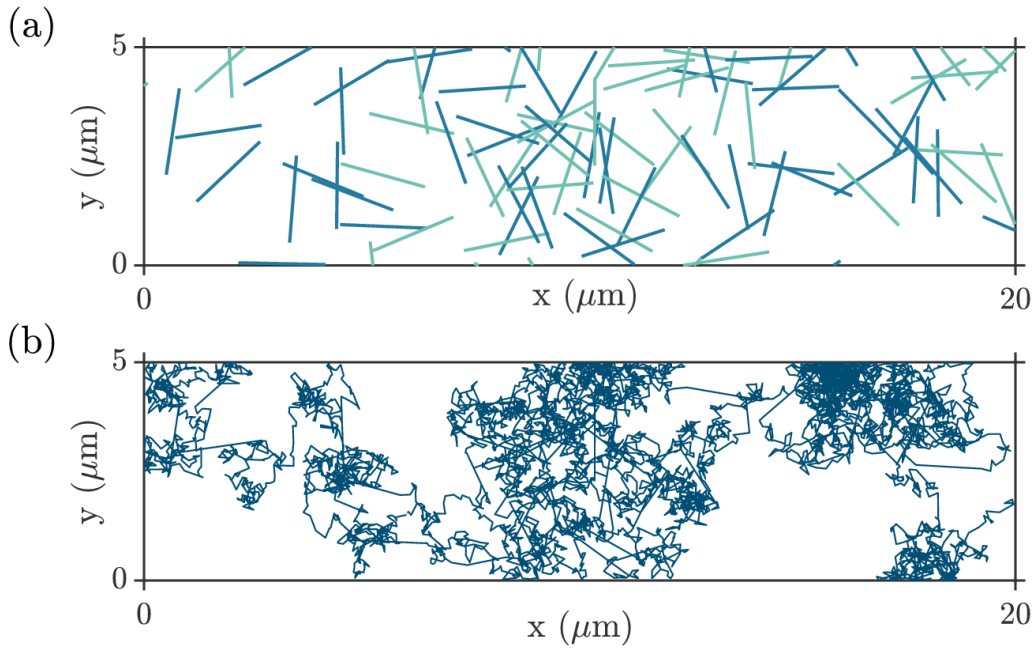

Figure 3.1: (a) Random configuration of filaments for a system containing 100 filaments of length 2 μm. Filaments possess either positive (blue) or negative (green) polarity, which specifies whether a motor bound to a filament moves in the positive or negative x-direction. (b) Sample path of a motor traversing the system from left to right.

the motor reaches the opposite boundary. The motor crosses the interval by a combination of passive diffusion and active transport along filaments. Figure 3.1 shows a sample filament configuration along with the path taken by a motor traversing the system from left to right in a sample simulation trajectory. Longer line segments on the path correspond to periods of directed transport. Each independent trajectory results in a different path.

Areas in which the motor spends the most time are characterized by discretizing the system and measuring the time spent in each discrete lattice site. The relative effect of an individual filament on the FPT in a network is investigated by reversing the polarity of that filament and measuring the resulting MFPT.

3.3 Results and discussion

3.3.1 The length and number of filaments influence first-passage properties

We begin by systematically varying the number (N_f) and length (L_f) of filaments in the system. For each case, we generate 10,000 network configurations, each of which is used to obtain a single stochastic trajectory. The mean first-passage time (MFPT) is obtained by averaging the FPTs of these trajectories, and the relative standard deviation is the associated standard deviation (σ) divided by the MFPT.

Figure 3.2 shows that the largest MFPTs with the highest variability occur in systems containing a relatively small number of long filaments; the smallest MFPTs occur in systems with large numbers of long filaments. Systems with many short filaments also have large MFPTs, but they exhibit less relative variability than systems with relatively few long filaments. It is interesting to note that systems with many short filaments exhibit larger MFPTs than pure diffusion ($N_f = 0$).

3.3.2 First-passage times can vary widely for networks with the same number and length of filaments

Figure 3.3 shows the full distribution of FPTs for three cases appearing in Fig. 3.2. This includes the case with no filaments ($N_f = 0$) in which the particle moves by diffusive motion only. The smallest MFPT is associated with large numbers of long filaments ($N_f = 3000$, $L_f = 3$ μm). The FPT distribution for this case has a peak at relatively short times and is somewhat right-skewed, with the peak occurring at a time moderately lower than the mean. The case with 100 filaments of length 3 μm exhibits the largest MFPT. Interestingly, this case has a peak in the FPT distribution at shorter times than the purely diffusive case, but the MFPT is more than twice as long. Although there is a relatively narrow distribution around the peak, the large MFPT is caused by the long tail of the distribution in which FPTs are anomalously large but relatively rare (Fig. 3.3, inset). The overall distribution reflects the time for a motor to traverse many different underlying filament configurations,

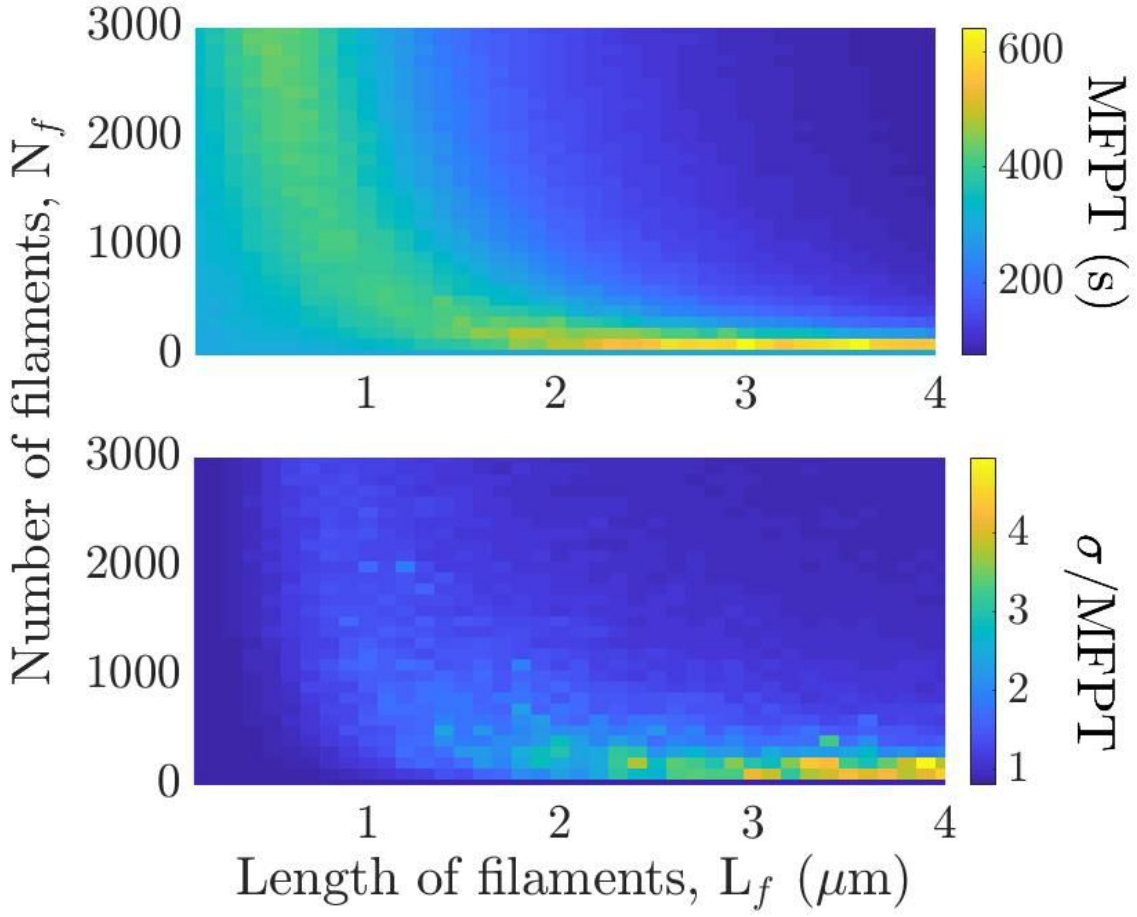

Figure 3.2: Mean first-passage time (MFPT, top) and relative standard deviation (σ/MFPT, bottom) for various numbers (N_f) and lengths (L_f) of filaments. Each value is obtained from 10,000 independent trajectories, each generated with a different filament configuration.

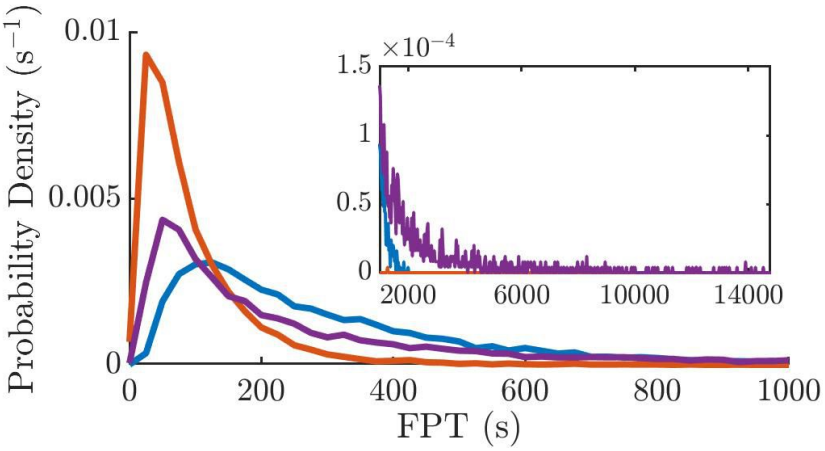

Figure 3.3: Probability density of first-passage times (FPTs) in systems with no filaments (blue, MFPT = 298.9 s), 3000 filaments of length 3 μm (red, MFPT = 95.2 s), and 100 filaments of length 3 μm (purple, MFPT = 633.8 s). The tails of the distributions at longer times are shown in the inset. Each distribution is constructed from 10,000 trajectories.

suggesting that typical configurations lead to relatively fast transport, but that a small fraction of configurations produce very slow transport. Others cases from Fig. 3.2 with a large relative standard deviation have similar distributions of FPTs.

To investigate the influence of specific filament configurations, we also determine the distribution of FPTs for fixed configurations. When sampling over independent, randomly generated filament configurations, we refer to the resulting FPT distribution as "annealed." The results shown in Figs. 3.2 and 3.3 were obtained in this manner. In contrast, when determining the distribution of FPTs for a specific filament configuration, we refer to the distribution as "quenched." To illustrate the difference, Fig. 3.4 compares annealed and quenched FPT distributions for a system consisting of 100 filaments of length 3 μm. Each quenched distribution was obtained using a different filament configuration. Pronounced differences are evident when comparing results for the three configurations and for the annealed case. In particular, the third quenched distribution is strikingly flat with a long tail. The MFPT associated with this configuration is 1,111 s, in comparison with 634 s for the annealed case and 156 s for the first quenched configuration. This indicates that the filament configuration, even with the same network properties, can markedly influence the ability of a motor to traverse the system.

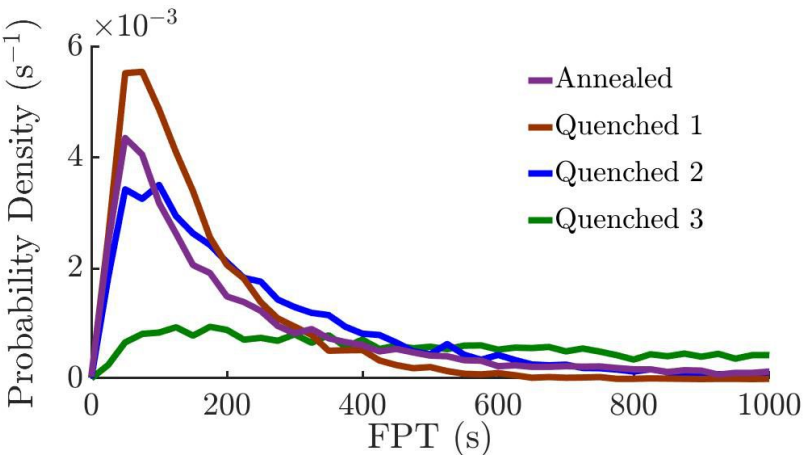

Figure 3.4: Annealed versus quenched FPT distributions. The probability density is generated from independent, randomly generated network configurations ("Annealed," MFPT = 633.8 s) and for fixed filament configurations ("Quenched 1 - 3" for three different configurations; MFPT = 155.7 s, 257.1 s, and 1,111.3 s, respectively). Each network contains 100 filaments of length 3 μm. Each distribution is constructed from 10,000 trajectories.

Differences between quenched distributions of FPTs result from differences in the configurations of filaments. In the following, we explore both "bulk" properties that reflect the entire filament configuration and "local" properties that involve specific local arrangements of filaments.

3.3.3 The MFPT is correlated with net filament polarity

The random generation of a filament configuration can lead to a net filament polarity, which we characterize in terms of the fraction of filaments oriented toward the initial boundary. We refer to configurations with a fraction greater than 0.5 as having "net negative polarity," meaning that more than half of the filaments are negatively polarized and point away from the target boundary. Because motors bound to these filaments move away from the target boundary, a larger fraction of negatively polarized filaments is expected to increase transit times on average.

Figure 3.5 shows the MFPT as a function of the net filament polarity for various numbers and lengths of filaments. The dominant trend is that a larger fraction of negatively polarized filaments leads to a larger MFPT. For the case with a large number of short filaments ($N_f = 3000$, $L_f = 1$ μm), the MFPT increases by approximately a factor of two when the

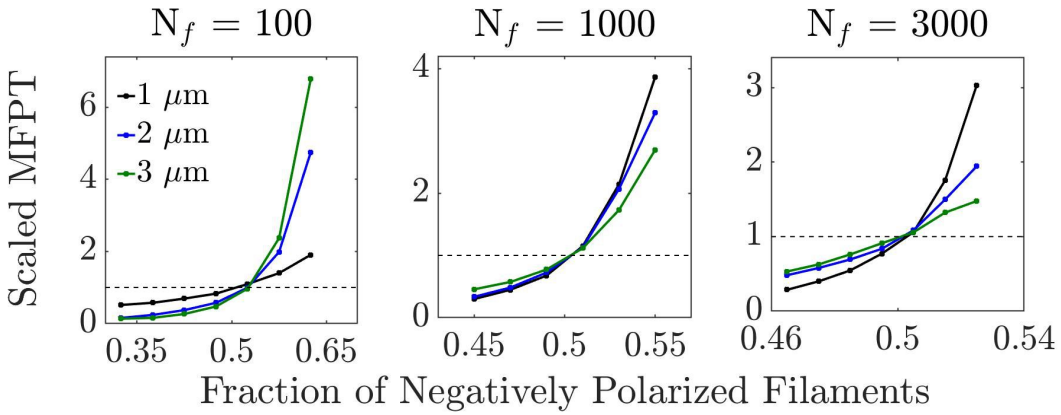

Figure 3.5: Scaled MFPT versus the fraction of negatively polarized filaments in the network. Different combinations of filament length (L_f) and number (N_f) are shown. Each curve is constructed with data from 10,000 independent trajectories (each with a randomly generated filament network). For each case, the MFPT for all trajectories is scaled to 1 (horizontal dashed line). The fraction of negative filaments is binned so that each bin contains many samples; the scaled average MFPT for each bin is shown.

fraction of negatively polarized filaments increases from 0.5 to just 0.52. The magnitude of the change in MFPT highlights the sensitivity to net filament polarity.

The results in Fig. 3.5 are consistent with trends in Fig. 3.2: Cases with a larger relative standard deviation (Fig. 3.2) exhibit a more pronounced increase in MFPT as the fraction of negatively polarized filaments increases. For example, systems with relatively few filaments ($N_f = 100$) exhibit greater sensitivity to the net polarity when filament lengths (L_f) are greater, which is the regime in which they have a large relative standard deviation. In contrast, systems with larger numbers of filaments ($N_f = 1000$ and 3000) are most sensitive to net polarity when filaments are short.

When there is a net filament polarity in the system, the MFPT can be impacted in two ways. The first is that there is a net bias in the transport of the motor across the system. One can think of this as a drift term in a diffusion equation or as a bias in the steps of a random walk. The second is that an increased number of negatively polarized filaments increases the likelihood of local filament configurations that impact the first passage of the motor, for example by locally trapping the motor in a specific region [126, 9] or by acting as a barrier through a particular interval in the system.

3.3.4 Reversing the polarity of filaments can significantly impact the MFPT

We now explore the relationship between the layout of filaments and how each filament is polarized. Given a particular filament configuration, we first determine its MFPT; we then reverse the polarity of all filaments in the system and determine the resulting MFPT. Figure 3.6a shows one example configuration ($N_f = 100$, $L_f = 3$ μm) and its counterpart with reversed polarity. Here the original filament configuration has an anomalously large MFPT of 5484 s while the network with reversed polarity has a MFPT of 46 s. The original configuration has a large fraction of negatively polarized filaments (0.63), and it is likely that local structures involving small numbers of filaments contribute to the large MFPT. For example, all filaments near the starting position are negatively polarized, thus effectively trapping the motor near its starting location. Reversing the polarity of all filaments alters this local structure and eliminates its ability to trap the motor, thereby significantly reducing the MFPT.

Figure 3.6b shows the correspondence between the quenched MFPTs of randomly generated configurations and the configurations obtained by reversing the polarity of all filaments (each MFPT was obtained using 1000 trajectories). The general trend is an inverse relationship between the MFPT in the original and "reversed polarity" networks. Reversing the polarity can dramatically impact the MFPT, particularly for configurations initially having anomalously large MFPTs. This is particularly evident in the case with relatively few filaments ($N_f = 100$). Here, reversing polarities of all filaments can change the MFPT by over 3 orders of magnitude. Several large changes in the MFPT (> 1000 s) were identified in configurations with no net polarity, indicating that changes in local organization — and not just net polarity — can strongly influence the MFPT.

3.3.5 Identifying traps and high-impact filaments

To probe local effects involving specific arrangements of filaments, we first identify where motors spend the most time by characterizing the average residence time as a function of

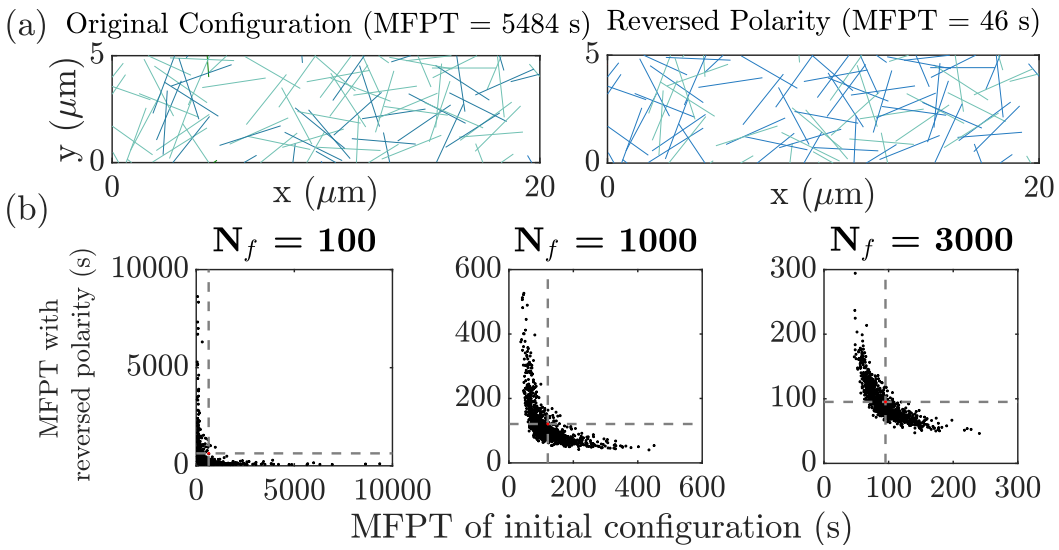

Figure 3.6: (a) Original and reversed filament configurations ($N_f = 100$, $L_f = 3$ μm) producing abnormally large and small MFPTs, respectively. (b) A comparison of the MFPT for random filament configurations ("initial configuration") and the configurations generated by reversing the filament polarity ("reversed polarity"). Dashed lines represent the MFPT obtained from the annealed average. Filaments are 3 μm in length.

position. For a given filament configuration, we discretize the system into 0.01 μm^2 square regions and determine the average time spent in each region over 10,000 trajectories.

Figure 3.7 shows the mean residence time for a system with no filaments and for the filament configuration shown in Fig. 3.6a. For the purely diffusive case, the residence time decays from left to right in an approximately linear manner. Cases with filaments typically look qualitatively different because of the spatial heterogeneity imposed by the filaments. Given a filament configuration, the map of residence times highlights the particular filaments and regions of space where a motor spends the most time. Regions with large residence times that are surrounded by small numbers of frequently-occupied filaments indicate local filament structures that promote extended occupancy. These filaments constitute a "trap" in which a motor remains confined for extended periods of time [9]. The example in Fig. 3.7b shows that filaments trap the motor near the starting position.

The emergence of traps suggests that small numbers of localized filaments have a disproportionately large influence on the overall MFPT. To probe this idea, we systematically perturb the network structure by reversing the polarity of each filament (one at a time) while keeping all others in their original state. For each perturbed network, we compute the

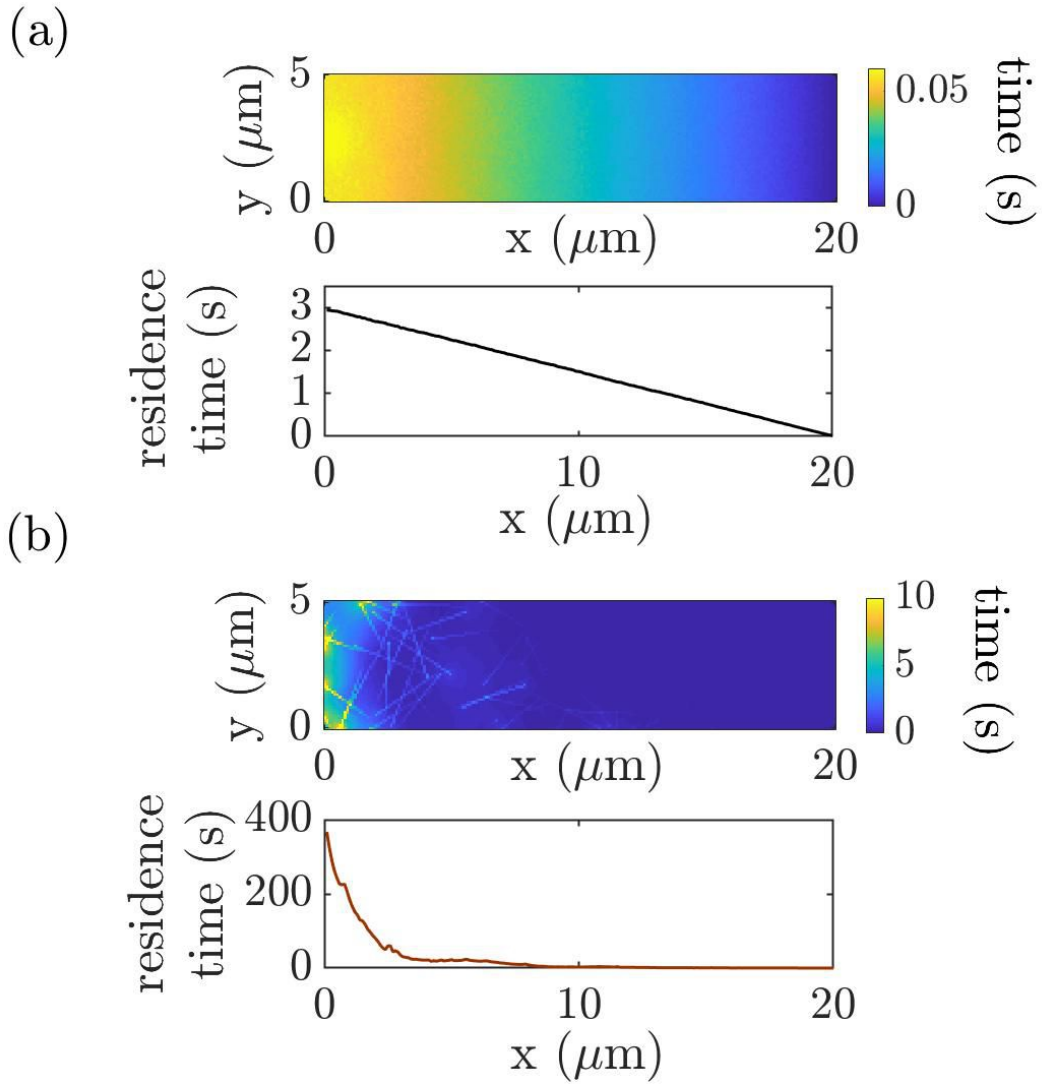

Figure 3.7: Average residence times (a) for diffusive motion only (no filaments) and (b) for the filament configuration shown in Fig. 3.6a. The heat maps show the average residence time in each square lattice site when the space is discretized; each site has area 0.01 μm^2. The corresponding line plots show the average residence time in each vertical slice of width $\Delta x = 0.1$ μm. Results are averaged over 10,000 trajectories.

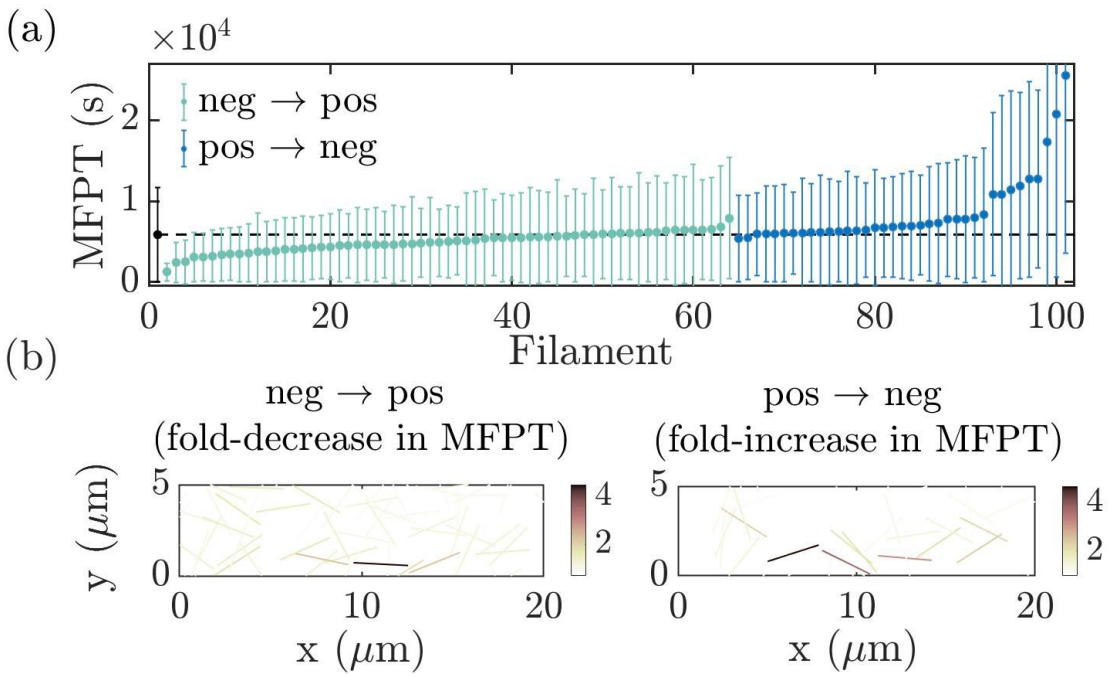

Figure 3.8: (a) The MFPT obtained when reversing the polarity of each filament (one at a time) from the configuration in Fig. 3.6a. Results are sorted in order of increasing MFPT for filaments that were initially negatively (green) and positively (blue) polarized. The MFPT of each new configuration is averaged over 100 independent trajectories (shown with the standard deviation). The MFPT of the initial configuration is indicated by the dashed horizontal line. (b) Filaments colored according to their impact on the MFPT when their polarity is reversed: The fold-decrease in MFPT for filaments changing from negative to positive polarity (left) and the fold-increase in MFPT for filaments changing from positive to negative polarity (right).

resulting MFPT using 100 independent trajectories. Figure 3.8a shows the results for the filament network presented in Fig. 3.6a. The network contains 100 filaments of length 3 μm, so reversing the polarity of each results in 100 new configurations.

Figure 3.8a shows that changing the polarity of filaments that were initially negatively polarized typically leads to a decrease in MFPT; changing the polarity of filaments that were initially positively polarized typically increases MFPT. The change in MFPT due to a single filament can be quite substantial, as evidenced by the greater than 4-fold decrease and 4-fold increase in MFPT for the most extreme cases. It is interesting to note that reversing the polarity of negatively (positively) polarized filaments can increase (decrease) the MFPT. This further indicates the importance of local filament structures on transport.

The previous results suggest that certain filaments have outsized influence on the first-passage properties of motors crossing the interval. Given the trap regions previously identified, it is interesting to characterize where the most impactful filaments are located. Figure 3.8b shows the location of filaments and their influence on the MFPT when their original polarity is reversed. Interestingly, the highest impact filaments are not located near the areas of high residence time but instead are found "downstream." In this case, the filaments whose reversal cause the largest increase in MFPT appear to form a bridge that link the trap with a region of the system closer to the final boundary. The other filaments in this region are polarized toward the origin; thus, the high-impact filaments provide the only clear path from one side to the other. When one of them is reversed, the bridge is broken, and the motor is forced to traverse a field of filaments that are polarized toward the origin. Thus, even when the motor exits the initial trap, it is likely to be transported back to the trap.

This suggests that filaments most critical in determining transit times for a system with a large MFPT are not necessarily those that constitute a trap, but instead can be those providing a path away from one. These filaments act as lynchpins connecting different regions and facilitate transport of a motor to or away from areas of prolonged occupancy. This suggests that a motor enters and escapes trapping regions multiple times in a typical trajectory for a filament configuration with a large MFPT, thus producing a recurring unproductive cycling state.

We have focused on a single filament configuration with a large MFPT. As a step toward generalizing the results, we consider additional configurations that are characterized by MFPTs that are slow, typical, and fast compared with the annealed average. Figure 3.9 shows an additional configuration with anomalously slow transport. Traps can again be identified by inspection of the spatially resolved residence times. In this case, the most impactful filament whose reversal leads to an increase in MFPT is located near the end of the trap. The filaments leading to the largest decrease in MFPT are located downstream of the area with large residence time. The next two figures in Fig. 3.9 have intermediate MFPTs that are close to the annealed average. These also exhibit areas with enhanced occupancy, but the time spent in these regions is less pronounced than in the slow cases. Flipping

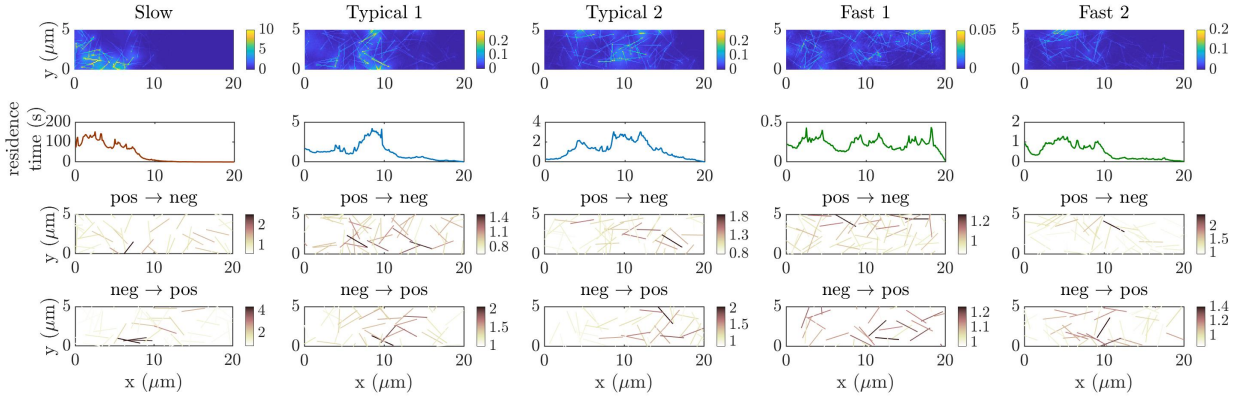

Figure 3.9: Residence times and impact of single-filament reversal for five configurations of filaments with $N_f = 100$ and $L_f = 3$ μm. The configurations are categorized as slow, typical, and fast in comparison to the MFPT for the annealed case. From left to right, the MFPT values for the initial configurations are 7960 s, 250 s, 251 s, 46 s and 98 s. The first two rows show average residence times (analogous to Fig. 3.7). Rows 3 and 4 show the fold-increase and fold-decrease in MFPT, respectively, resulting from changing the polarity of single filaments (analogous to Fig. 3.8b).

individual filaments can still significantly influence the MFPT, but to a lesser relative degree than in the slow cases. High-impact filaments are located both within and downstream of traps. The final two configurations in Fig. 3.9 have fast MFPTs. In the first, the residence time is relatively constant throughout, in contrast with the diffusive case, which decays linearly. In the second, the motor spends substantially more time in the first half of the domain than the second half. There is a single filament whose reversal leads to a substantial change in MFPT; it is located just beyond the high-residence time area.

Collectively, the results in Figs. 3.8 and 3.9 show that altering single filaments can dramatically influence the MFPT and that the most impactful filaments can be located in areas that are not associated with traps. For cases in which the high-impact filaments are downstream of traps, they appear to serve as lynchpins that connect trap regions with regions further downstream; other filaments in their vicinity are typically polarized in the opposite direction. For anomalously slow FPTs, the physical picture that emerges is that the motor escapes and re-enters trap regions multiple times.

3.3.6 Do motors behave diffusively when the number of filaments is large?

In the previous section, we focused on a regime with moderate numbers of long filaments. We established that the configuration of filaments plays a large role in dictating FPTs, and that averaging over different configurations leads to broad distributions of FPTs. In this section, we consider a regime with large numbers of filaments. We investigate whether motors behave diffusively in this regime at sufficiently long times, and if so, whether the effective diffusion coefficient produces the MFPT obtained from an annealed average over configurations of filaments.

With a large density of filaments, a motor will spend most of its time bound to filaments because it is typically within binding range of multiple filaments. Additionally, a large density reduces correlations in the motion of a motor imposed by rebinding to recently-traversed filaments. Thus, in a large isotropic system, the motor is expected to undergo a random walk with a step size dictated by the filament length. An effective diffusion coefficient for this motion would be given by $D_e \approx (1/2d)\,\overline{l^2}/\tau$, where $\overline{l^2}$ is the characteristic square distance traveled between each filament binding, τ is the characteristic time to bind and traverse a single filament, and $d = 2$ is the dimensionality. Given sufficiently long filaments, the motor would rapidly bind to a new filament once unbinding from another. Thus, it would spend most time on filaments and, assuming the dissociation rate of the motor is small, $\overline{l^2}$ would be given by averaging over the square distance from a random binding position to the end of the filament, $\overline{l^2} \approx L_f^2/3$. The characteristic time, $\tau \approx (L_f/2)\Delta x^{-1} k_{\text{fil}}^{-1}$, is the average time required to traverse half the distance of the filament, giving $D_e \approx L_f\,\Delta x\,k_{\text{fil}}/6$. Thus, D_e is expected to scale linearly with the filament length for sufficiently long filaments.

To test the whether motors behave diffusively, we calculate the mean-square displacement (MSD) of a motor as a function of time in a larger system (100 μm $\times$ 100 μm) with 200,000 filaments. This gives the same filament concentration (20 filaments/μm^2) as for the interval with $N_f = 2000$. We vary the length of filaments and fit the long-time behavior of the MSD to a power-law to assess whether it scales linearly in time, as expected for diffusive behavior. Figure 3.10 shows the MSD for two different filament lengths, with the complete results shown

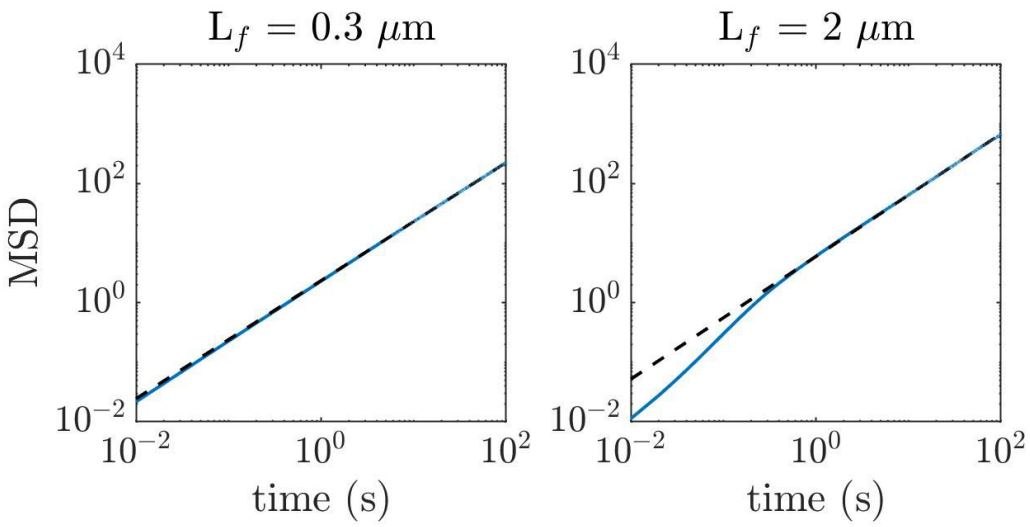

Figure 3.10: Mean square displacement (MSD, blue line) of motors in a 100 μm $\times$ 100 μm domain with 200,000 filaments of length $L_f = 0.3$ μm (left) and $L_f = 2$ μm (right). Dashed lines are power-law fits to long-time (10 s $< t <$ 80 s) data obtained from 1000 trajectories of length 100 s. The exponents are 0.99 (left) and 1.03 (right), indicating approximately diffusive motion.

in Figure B.1 of Appendix B. The case with short filaments ($L_f = 0.3$ μm) is approximately linear over the entire time domain. The case with long filaments ($L_f = 2$ μm) exhibits superdiffusive behavior at short times (< 1 s) and diffusive behavior at longer times. This is consistent with ballistic-like motion when motors are bound to filaments and to random-walk behavior at longer times. The diffusive behavior emerges at times considerably shorter than the typical first passage times obtained for a motor crossing a 20 μm $\times$ 5 μm interval.

The long-time behavior of the MSD is approximately linear for all values of L_f. We use the slope of linear regime with the expression $\text{MSD}(t) = 4D_e t$ to determine D_e, the effective diffusion coefficient. The results are shown in Fig. 3.11a. The diffusion coefficient is nonmonotonic as a function of L_f, as D_e decreases between $L_f = 0$ and $L_f = 0.3$ μm and increases beyond $L_f = 0.3$ μm. This is likely a consequence of short filaments having truncated steps (< 100 nm) near the ends of filaments and more frequent rebinding. The behavior of D_e at larger values of L_f increases in an approximately linear manner, which is consistent with the scaling arguments above. However, the slope of the line (≈ 0.81) is smaller than the value of 1 that emerges from the scaling analysis. This may be because we

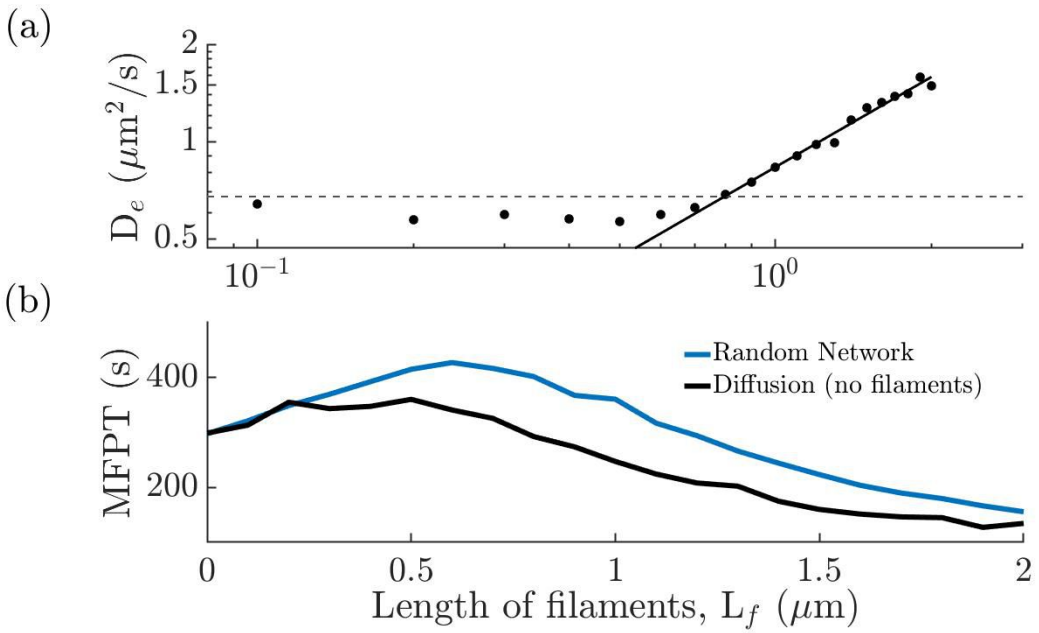

Figure 3.11: (a) Effective diffusion coefficient (D_e) obtained from the MSD for various filament lengths (L_f) for a system with 20 filaments/μm^2. The diffusion coefficient of the motor in the cytoplasm is indicated by the dashed line. The solid line is a linear fit to the data ($L_f \geq 1$ μm), $D_e = 0.81\, L_f$. (b) Comparison of MFPTs obtained in original simulations with filaments and in simulations without filaments using the effective diffusion coefficient. Cases with a filament network contained 2,000 filaments of various lengths. Cases without filaments used the effective diffusion coefficient from (a). All data points represent averages over 10,000 trajectories.

are not probing sufficiently large values of L_f or because not all of the assumptions (e.g., negligible rebinding) hold.

Using the effective diffusion coefficients from Fig. 3.11a, we finally determine the MFPT for a motor traversing the original interval (20 μm $\times$ 5 μm) in the absence of filaments. The results, shown in Fig. 3.11b, are consistent with the effective diffusion coefficient, with a maximum MFPT coinciding with the local minimum in D_e. However, when compared with the MFPT obtained from the simulations with explicit filament networks, it is evident that the effective diffusion coefficient underestimates the MFPT for most filament lengths. Thus, the behavior of the motor in the interval used to obtain FPTs is not well-described by purely diffusive motion governed by the effective diffusion coefficient. This suggests that local filament configurations impact the FPTs in nontrivial ways.

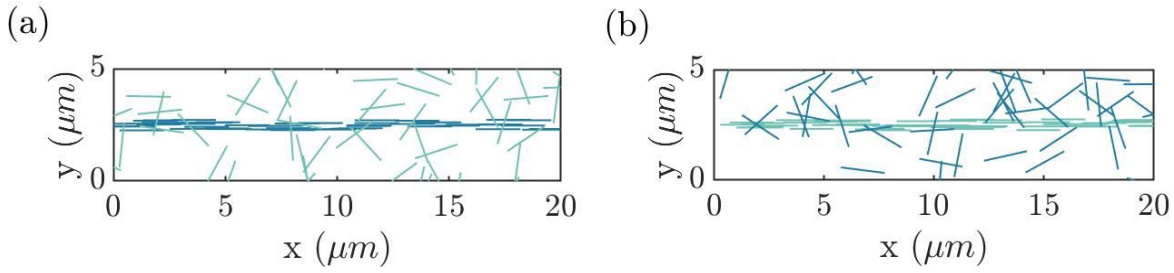

Figure 3.12: Random configuration of filaments for a net neutral polarity system containing 100 filaments of length 2 μm and 50% (a) positively polarized and (b) negatively polarized bundling.

3.3.7 Bundling of filaments decreases FPT variability

In the previous sections, all networks consisted of randomly oriented filaments of random polarity. Now we consider networks consisting of a portion of bundled filaments: horizontal filaments confined to a narrow horizontal band of width 0.5 μm located in the vertical center of the system. The previous non-bundled networks considered applied random polarity to each filament, and thus on average contained 50% negatively polarized and 50% positively polarized filaments. Thus, to preserve a net neutral filament polarity in the system while maximizing the fraction of bundled filaments, we consider the cases of 50% bundled filaments with the remaining 50% of filaments randomly oriented and polarized opposite to the bundle. Sample configurations for both negative and positive polarization variations of a system containing 100 filaments of length 2 μm are shown in Fig. 3.12. In these systems, the progression of a motor toward the end boundary via active transport within the bundle is counteracted by active transport outside the bundle.

As in Section 3.3.1, we again systematically vary N_f and L_f and compute the resulting MFPT and FPT variability for both bundling cases. Figure 3.13 shows that the MFPT for a system with 50% positive bundling decreases as the filament number N_f or length L_f increases. However, FPT variability for this case is highest in systems of many long filaments. This suggests that faster, more reliable transport relative to the no bundling case can be acheived with lower filament densities in these systems. In the 50% negative bundling case, an MFPT gradient profile emerges at low filament densities (small N_f or small L_f and $N_f L_f < 1000$) similar to that seen in the no bundling case shown in Fig. 3.2 but in reverse direction. Here, the MFPT decreases along this gradient in the transition from a many,

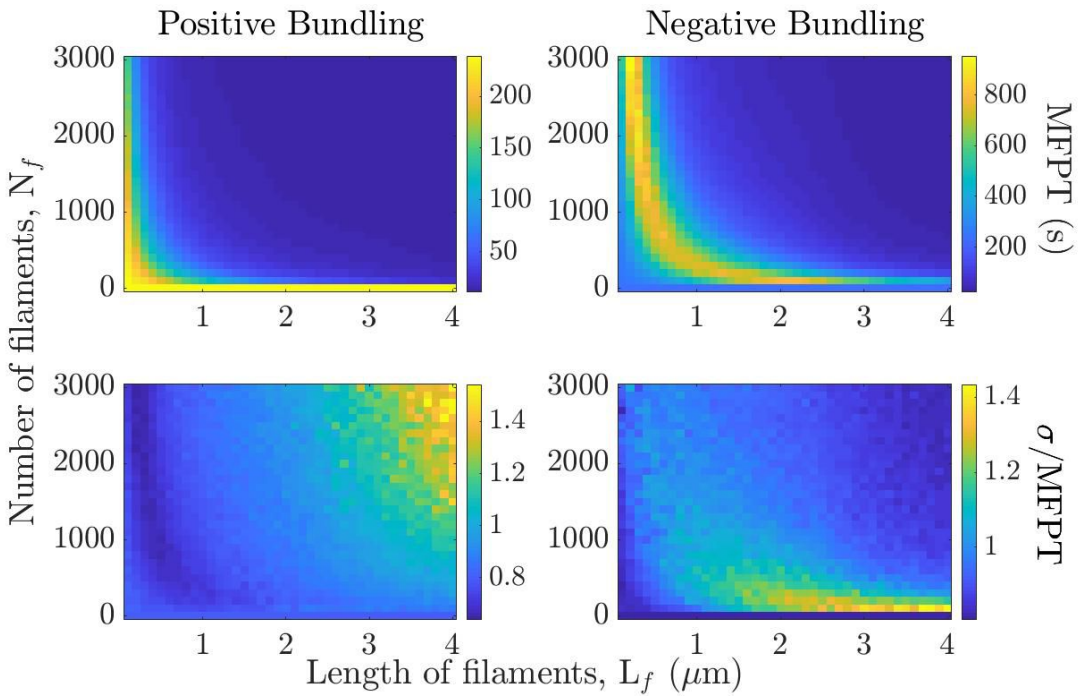

Figure 3.13: Mean first-passage time (MFPT, top) and relative standard deviation (σ/MFPT, bottom) for various numbers (N_f) and lengths (L_f) of filaments for the cases of 50% positively polarized bundled filaments (left) and 50% negative polarized bundled filaments. All non-bundled filaments are randomly oriented and polarized opposite to the bundle. Each value is obtained from 10,000 independent trajectories, each generated with a different filament configuration.

short filament regime to a few, long filament regime. Relative to the no bundling case, the MFPT is higher for systems of many short filaments and the MFPT and FPT variability is lower for systems of few long filaments. For these latter systems, the positive polarization of all filaments outside the bundle combined with the low density of filaments in the system (1 filament/μm^2) increases the likelihood that a motor will be transported away from the bundle region and spend a greater fraction of time in the low filament density bulk region of the system. The horizontal orientation of the negatively polarized bundle filaments leads to large horizontal displacements and thus prevents the formation of the previously discussed local trap regions composed of a small number of filaments that would lead to anomalously large FPTs. This further supports the finding that local filament configurations in randomly oriented networks can have an outsized impact on FPT.

Since a high concentration of filaments exist in a confined horizontal region in these bundled systems, motors within this bundle region are more likely to rebind to other bundle

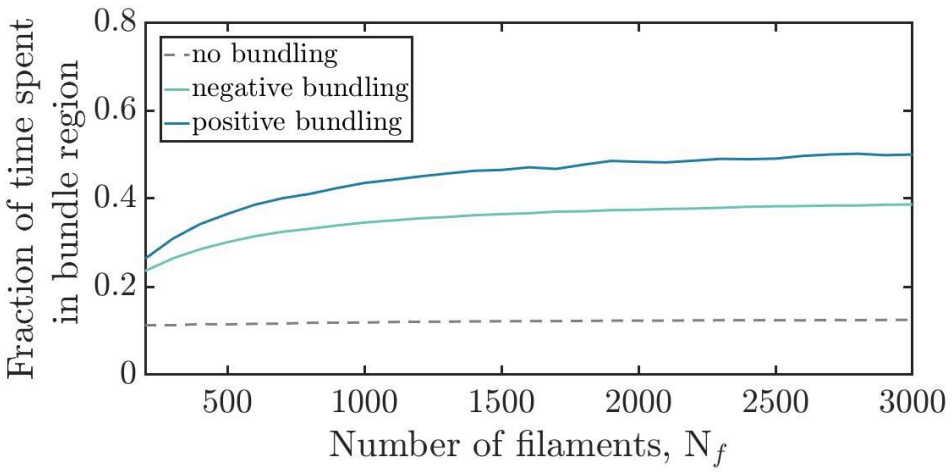

Figure 3.14: Fraction of time spent in bundle region (0.5 μm horizontal band in the vertical center of the system) for systems of net zero filament polarity of various numbers of 2 μm long filaments. Each value represents an average over 10,000 independent trajectories, each generated with a different filament configuration.

filaments and remain in this bundle region for extended periods of time. To investigate the impact of this heterogeneous filament density on residence time within the bundle region (vertical center 10% of system space), we discretize the system space and compute the total occupancy time in the bundle and non-bundle regions for 10,000 independent trajectories. The fraction of time spent in the bundle region for systems of various numbers of filaments is shown in Fig. 3.14.

In the 50% positive bundling case with $L_f = 2$ μm, motors spend more than 40% of their time in the bundle region for moderate to high N_f (> 700). In the equivalent negative bundling case, motors spend more than 33% of their time in the bundle region for this same regime. The reason for the discrepancy can be largely attributed to the condition that a motor must exit the bundle region to reach the end boundary in the negative bundling case, while a motor may remain in the bundle region to reach the end boundary in the positive bundling case. In both cases, however, the amount of time spent in this center 10% of the system space is 2-4 times greater relative to the equivalent non-bundled system case. This disproportionately large fraction of time the motor spends traveling in the same direction when bound to a filament contributes to the decreased FPT variability in bundled systems, and thus produces more reliable transport.

Table 3.1: Base parameters used for motion of motor-organelle complexes on actin filaments

Parameter	Description	Value
k_{hop}	Diffusive hopping rate	1728 s^{-1}
k_{fil}	Filament-bound hopping rate	480 s^{-1}
k_{on}	Binding rate to filament	0.1 s^{-1}
k_{off}	Unbinding rate from filament	0.5 s^{-1}
d	hopping distance	0.0125 μm
D	Diffusion coefficient	0.27 $\mu m^2 s^{-1}$
N_{org}	Number of organelles	200
N_f	Number of filaments	20

3.3.8 Movement of Motor-Organelle Complexes on Filament Networks

Thus far, we have considered systems of varying filament density and orientation to study transport properties of single motors on networks of filaments. In most real intracellular systems, many motors work cooperatively to transport biological cargo. One example is the transport of organelles during cytoplasmic streaming in plant cells. Through the use of fluorescence microscopy, the movement of individual organelles can be tracked over time.

To model the movement of individual organelles on actin filaments, we implement model parameter values consistent with experimental observations provided by our collaborators in the Nebenführ research group. Specifically, the mean velocity of a bound organelle on a filament is fixed at 6 μm/s, and on and off rates are chosen such that approximately 10% of organelles are bound to filaments at any given time. Organelles are equally sized with a diameter of 0.3 μm and can bind to a nearby filament only if it is located within a threshold binding distance of 0.15 μm. The system size is 10 μm $\times$ 10 μm, and filaments are assumed to span from boundary to boundary. We use periodic boundary conditions. Excluded volume effects apply to organelles bound to filaments, so an attempted move by an organelle on a filament resulting in spatial overlap with another organelle is rejected. No excluded volume effects are implemented in the cytoplasm. The model parameters used are summarized in Table 3.1.

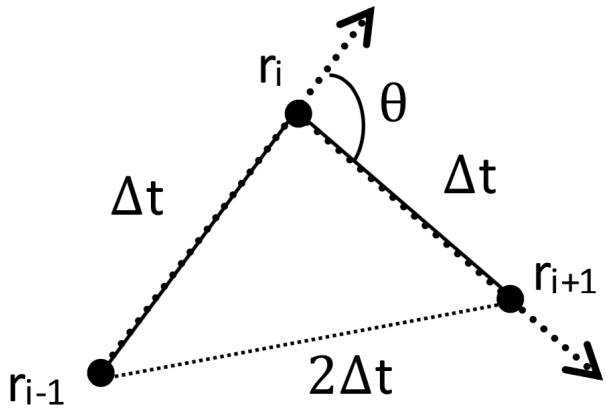

Figure 3.15: Schematic diagram for turning angle and displacement rate calculations. θ ranges from -π to +π, and is computed using a vector dot product with the x and y coordinates of consecutive position points r_{i-1}, r_i, and r_{i+1}. Displacement rate is computed over the entire time interval 2Δt using r_{i-1} and r_{i+1}.

We are interested in the motion of individual organelles in a given time interval, which can be characterized by the distance it moves and the angle by which it turns. For consistency with experimental measurements, we compute a single displacement rate and turning angle for each time interval, which is illustrated by the schematic shown in Fig. 3.15.

The turning angle θ during each interval $2\Delta t$ is computed as the angle between the vector displacement during the first timestep Δt and the vector displacement during the second timestep Δt. The associated displacement rate is computed over $2\Delta t$ as:

$$\frac{|\Delta r|}{\Delta t} = \frac{\sqrt{(x_{i+1} - x_{i-1})^2 + (y_{i+1} - y_{i-1})^2}}{2\Delta t} \tag{3.1}$$

where x_i and y_i represent the Cartesian coordinates of position r_i.

Applying different values of the full timestep $2\Delta t$, we observe the short-time and moderate-time behavior of organelle motion. Larger time intervals would include more diffusive and/or filament hops and more turns unless the organelle is continuously bound over the entire interval, thus producing different characteristic motion. The distribution of turning angles and associated displacement rates for time intervals of 0.1 s, 0.2 s, and 0.5 s are shown in Fig. 3.16.

Each heat map displays a low $|\Delta r|/\Delta t$ regime with wide range of θ, and a high $|\Delta r|/\Delta t$ regime with $\theta \approx 0$. The low $|\Delta r|/\Delta t$ regime represents diffusive organelles that spend

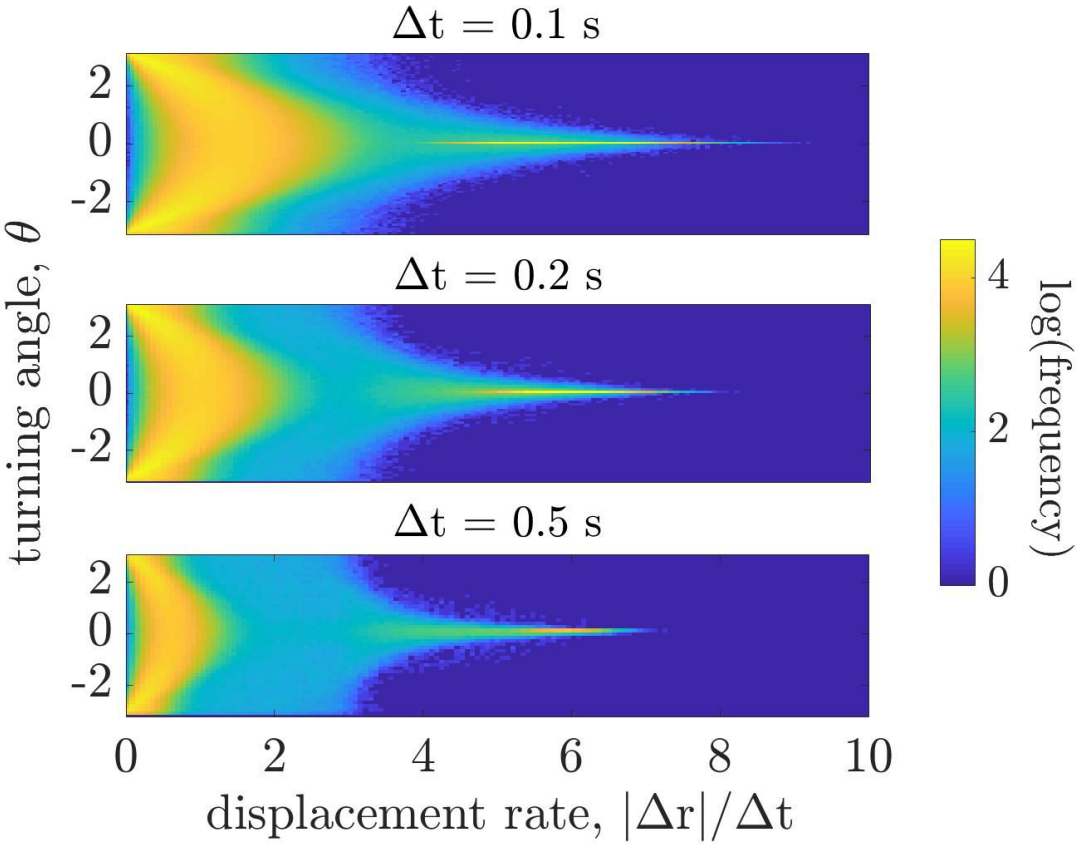

Figure 3.16: Distribution of motor turning angles and associated displacement rates over half-time intervals of 0.1 s, 0.2 s, and 0.5 s. Turning angle is defined as shown in Fig. 3.15 and displacement rates are computed using Equation 3.1. Data is obtained from each of 200 individual organelles from 25 independent trajectories over 1000 s each. The number of data points contained in each heat map is approximately 2.3×10^7 (top), 1.1×10^7 (center), and 3.9×10^6 (bottom). The frequency of each displacement rate and turning angle combination is log-transformed.

the majority of the time interval unbound, or the "passive regime". Since these organelles undergo diffusive motion, they turn at random angles and thus have a wide θ range. An inverse correlation between $|\theta|$ and $|\Delta r|/\Delta t$ emerges in the low displacement rate regime since an angle of $\pm\pi$ would indicate the organelle hopped forwards and backwards along the same path, which would yield a displacement of 0.

The high frequency of points in the high $|\Delta r|/\Delta t$ regime represent organelles that are bound and move along filaments for the majority of the time interval, or the "active regime". The turning angle is approximately zero since the organelle moves along a consistent vector while on a filament. As the time interval Δt increases, the passive and active regimes shrink in size and the maximum $|\Delta r|/\Delta t$ decreases. For small Δt, a small number of total moves occurs and thus the probability of being bound for the entire Δt interval increases. Thus, the relative frequency of $\theta = 0$ is highest at low Δt values.

Taken together, these results reveal that the largest organelle displacement rates are observed in the short-time regime, and passive and active regimes are clearly discernible over both short and moderate-time intervals. This suggests that organelle motion in a network of filaments, much like single motors on networks of finite-length filaments as detailed in Section 3.3.6, would not be well-approximated by purely diffusive motion. This is especially noteworthy given the relatively low filament binding rate leading to a steady state fraction of only 10% of organelles bound.

3.3.9 Cytoskeletal traffic in multiple motor systems

To study the effect of motor traffic on transport properties, we again apply excluded volume effects to motors bound to filaments and revert to the kinetic rates listed in Sec. 3.2 to increase motor movement on filaments. To characterize the transport properties of a given multiple motor system, we measure the normalized motor current for a given set of conditions, which is computed as the number of filament-bound motor moves per unit length per unit time.

We begin by investigating the dependence of current on the number of motors. We systematically increase the number of motors in a 10 μm $\times$ 10 μm system of 20 randomly oriented filaments of indefinite length. Since kinetic rates are kept constant, the number of bound motors increases with the total number of motors in the system up to the point

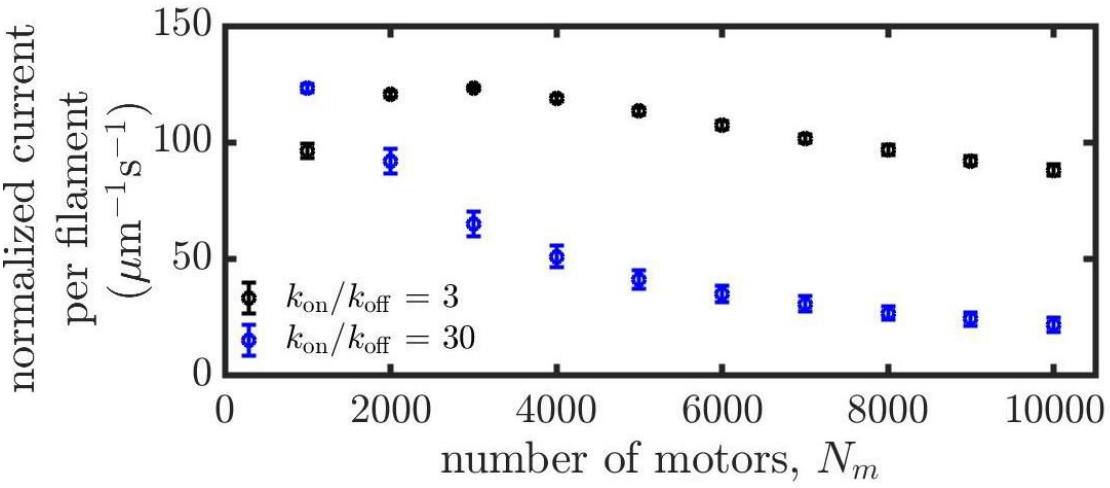

Figure 3.17: Motor current per μm of filament versus number of motors in a 10 μm $\times$ 10 μm system of 20 randomly oriented filaments of indefinitely length. Each data point shows the mean and standard deviation over 25 independent trajectories of 100 s each. The binding rate k_{on} is fixed at 6 s^{-1} and the unbinding rates k_{off} used are 2 s^{-1} and 0.2 s^{-1} . The lower k_{on}/k_{off} ratio reveals non-monotonic behavior of current with respect to N_m while a 10-fold decrease in unbinding rate leads to monotonically decreasing current with increasing N_m.

where filaments become saturated with motors. In the extreme case, a system that has every filament completely saturated with bound motors will have zero current unless unbinding events first occur to make segments of filament accessible to motor motion. At high motor densities, excluded volume effects on filaments are significant in that "traffic" limits motor moves on filaments. To investigate the effect of motors being bound to filaments for longer time periods, the k_{on} to k_{off} ratio is altered by decreasing k_{off} by a factor of 10. The motor current per length of filament as a function of the number of motors in the system for both of these sets of kinetic rates is shown in Figure 3.17.

For the lower k_{on}/k_{off} ratio, the current is maximized at an intermediate value of motor population. A 10-fold decrease in the off rate leads to monotonically decreasing current in the motor population regime considered. This can be understood intuitively since a decreased unbinding rate implies a higher number of motors bound at steady state and consequently an increased incidence of "traffic jams" that limit current. These jams are only successfully alleviated with readjustments of motor positions on the filament, which is often achieved through an unbinding event followed by a binding event at a different filament site. In effect, systems that are more densely populated with molecular motors, and thus possess a

higher propensity for traffic jams, achieve greater current when unbinding is more frequent. Figure 3.17 confirms that greater current is achieved in the high motor density regime for the system with greater unbinding rate.

To probe the effect of having a network of filaments versus a single filament, we consider a single filament in which motors always remain bound. The length of filament was fixed at 10 μm to correspond to the characteristic length of the multiple filament system. Motors were first placed on the filament at random positions, and periodic boundary conditions on the filament were applied to measure motor current over extended time periods. Next, motors were placed immediately adjacent to each other. Since all motor moves occur with equal displacement, the latter case represents a situation in which motors are either immediately adjacent or separated by an integer number of motors moves. The number of motors bound to the filament was systematically increased to match the average number of motors bound at steady state per 10 μm of filament in the filamentous network. The motor current as a function of the number of bound motors per filament for these two single filament cases along with the filament network case are shown in Figure 3.18.

Motor current is greatest in the close-packing configuration for higher filament density cases. When filament density is low, motors are less likely to encounter traffic on a filament and so all three cases have approximately equal current. The randomly positioned motor configuration is similar to the filamentous network configuration since positions at which binding occurs are determined stochastically. The filamentous network achieves greater current only at high values of motor density on the filament. As the filament approaches saturation, the randomly positioned motors on a single filament system reach a fixed upper limit in current while the filamentous network is able to achieve larger current up to an elevated upper limit because of unbinding and binding events. In this way, the effects of a network configuration of filaments are observed most prominently at high motor densities.

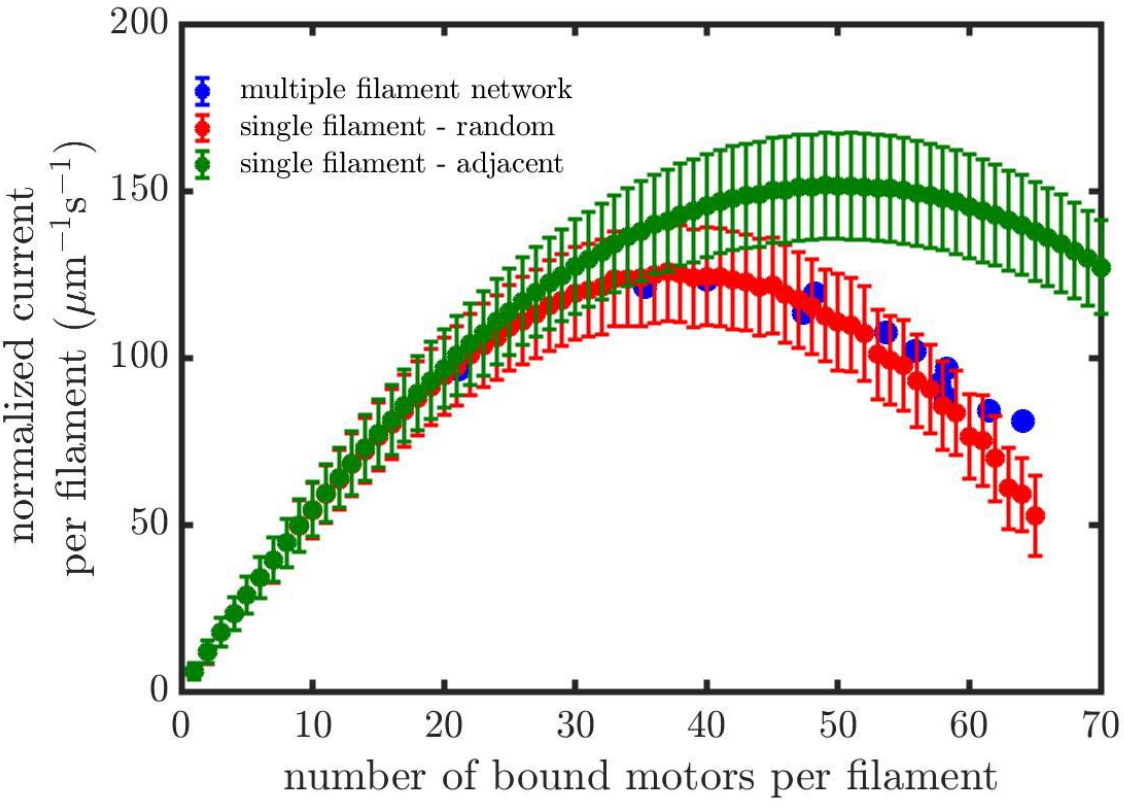

Figure 3.18: Motor current per μm of filament as a function of average number of bound motors per filament for single filament and network cases. Each data point represents the mean and standard deviation over 1000 independent trajectories of 100 s each. Maximum current is achieved when motors are positioned immediately adjacent to each other on a single filament. Relative to randomly positioned motors on a single filament, the filament network achieves greater current as filaments approach their saturation point.

3.4 Conclusions

We used stochastic computer simulations to explore the transport of molecular motors traversing a two-dimensional interval with random configurations of cytoskeletal filaments. The motors undergo a combination of diffusion in the cytoplasm and active transport when bound to filaments. We varied the length and number of filaments and characterized the mean first-passage time (MFPT) for a motor to traverse the interval. As shown in Fig. 3.2, cases with relatively small numbers of long filaments had large MFPTs with high variability. This was a consequence of anomalously large first-passage times associated with particular network configurations. Cases with large numbers of short filaments also produced large MFPTs relative to pure diffusion, although with less relative variability. Large numbers of long filaments decreased the MFPT relative to the case of purely diffusive motion. The fact that MFPTs for systems of many short filaments were larger than those for purely diffusive motion suggests that a minimum filament length is needed for active transport to enhance transport across a domain.

We further investigated the source of large, highly variable FPTs, finding that specific filament configurations produced localized spatial "traps" in which motors spend most of their time. Additionally, we systematically perturbed the polarity of each filament to assess the impact on the MFPT. Surprisingly, perturbing certain filaments produced large changes in MFPT. Some of these were found "downstream" of traps, suggesting that high residence times in traps were not only the consequence of the filament configuration in the immediate vicinity, but also of filaments that linked the trap to other spatial regions. These filaments typically provided the only clear path through a region that was otherwise filled with filaments polarized in the opposite direction. We also showed that in cases with large numbers of filaments, the mean square displacement of unconfined motors can be used to determine an effective diffusion coefficient. However, this diffusion coefficient underestimates the MFPT to traverse a confined interval, again suggesting the importance of local filament organization when confined in a finite domain.

The potential for local filament structures to lead to increased FPTs was highlighted by the introduction of a long and narrow bundle region of horizontally oriented like-polarized

filaments while preserving net zero filament polarity. Occupancy within a bundle region leads to larger horizontal displacements that allow a motor to bypass local structures composed of a small number of filaments. In the regime of few long filaments, bundling of filaments of either polarity leads to lower MFPTs compared to the non-bundled case. An effective way to mitigate slow transport is in the bundling of filaments with positive polarity, which was shown to consistently produce lower MFPTs with increasing filament density. Bundling, whether it be in the negatively or positively polarized direction, was shown to increase reliability of transport by decreasing FPT variability in low to moderate filament density regimes.

We briefly studied the motion of motor-organelle complexes on networks of filaments using parameters consistent with experimental observations from a collaborating research group. We found that passive and active motion regimes exist at small and moderate time intervals even for low filament binding rates. Sampling at higher time intervals leads to a smaller range of displacement rates in both regimes as probabilities of being bound to a filament for a large fraction of the time interval decrease. The short to moderate time behavior of organelle motion on a network of filaments, much like the movement of individual motors, would not be well-approximated by purely diffusive motion.

We modeled cytoskeletal traffic by considering multiple motors moving on individual filaments, finding that motor current may be optimized at intermediate motor densities since saturation of motors on filaments effectively limits motor movement due to excluded volume effects. In comparison to randomly placed motors on single filaments, we found that the use of a filament network is effective in attaining higher motor current in the high motor density regime. This suggests that a network configuration is most effective in achieving faster transport when many motors cooperatively interact in the system space.

Overall, we identified general parameter regimes and mechanisms by which intracellular transport of a single molecular motor on a static filament network in two dimensions can become slow and/or unreliable. Many cells have quasi-two-dimensional regions in which motor transport occurs. For example, some plant cells have highly-constricted regions due to the close proximity of a vacuole and plasma membrane. However, understanding transport in less confined regions is also of interest, and extending to three dimensions may reduce the likelihood of traps due to the additional degree of freedom for escape. Additionally,

the actin cytoskeleton is regulated by myriad proteins that organize it into structures such as actin bundles [78, 79], which can vary in thickness and density. It will be of interest to understand effects of actin organization on intracellular transport. In this context, understanding dynamic changes in the cytoskeleton [89, 70, 47], crowding effects due to many motors [155, 2, 106, 136, 148, 33, 112], and the effects of multiple motors associated with individual cargo [126] will be interesting avenues of future research. This study provides a foundation for investigating these future directions.

Chapter 4

Protein Organization Along the Actomyosin Ring

Summary: Sections 4.4 - 4.5 of this chapter are based on the submitted paper:

Onwubiko, U., Mlynarczyk, P. J., Wei, B., Habiyaremye, J., Clack, A., Abel, S. M., and Das, M. E. (2018) *The Cdc42 GEF, Gef1, promotes uniform protein distribution along the actomyosin ring to enable concentric furrowing.* Manuscript submitted for publication.

4.1 Introduction

4.1.1 Cell polarity by positive feedback

The establishment of cell polarity is another important biological process involving heterogeneous distributions of proteins, in which an asymmetric accumulation of proteins such as Rho GTPases serves to define a unique cellular axis. It has been shown that regions with high density of proteins can spontaneously arise, and these protein clusters can persist for long periods of time [35, 36], even in the apparent absence of pre-existing cues [130, 152]. Abrupt transitions in protein spatial patterns can activate cellular pathways and subsequently direct downstream cellular processes [27], and so precise regulation of spatial pattering and formation of protein clusters is crucial in ensuring proper cellular function.

Experimental and theoretical studies have suggested that several distinct mechanisms may contribute to the establishment and preservation of cell polarity. Mechanisms involving directed transport utilize the cytoskeleton to preserve polarity by directing signalling molecules to specific locations on the membrane [151, 98]. Positive feedback has been shown to be capable of amplifying stochastic fluctuations to produce clusters of active molecules [31, 50, 63, 103], and thus play a central role in dynamically stable spatial pattern formation. Activation of positive feedback circuits can induce spontaneous cortical polarization in cells [152, 75], and so it has been hypothesized that positive feedback alone can enable the recruitment of signaling molecules to localized regions on the plasma membrane and thus establish sustained cell polarity [7]. However, it has also been shown that regulation of spatial patterning can be achieved through the coupling of positive feedback with other proposed mechanisms such as coupled activation-dependent inhibitors [139, 110], long-range negative feedback [54], molecular noise regulation [91], feedback component sequestration [64], or endocytosis [142]. Besides these potential mechanisms, proteins also undergo diffusive motion while on the plasma membrane. Lateral diffusion can strongly influence spatial distributions of proteins [62, 142] and reduce polarized distributions even in the presence of positive feedback circuits.

Budding yeast is an established model system that utilizes a simple actin-independent positive feedback circuit for establishment of spontaneous polarization of the GTPase Cdc42 [7, 77]. In this system, the GTPase Cdc42, a major regulator of cell growth and shape, can recruit other Cdc42 molecules to the plasma membrane via its interactions with the guanine nucleotide exchange factor (GEF) Cdc24 and the adaptor protein Bem1 [152, 25, 75, 127]. This leads to a state of cell polarization that is maintained in a state of dynamic equilibrium with rapid protein exchange between the membrane and the cytoplasm, and polarization sites are found to incur occasional drifting [152]. The degree of polarization was found to be maximized at intermediate total protein numbers [77], but the influence of parameters such as feedback strength and endocytosis rate were not explored.

In this work, we first explore a model of cell polarity by means of a simple self-recruitment positive feedback mechanism coupled with lateral diffusion and spontaneous association and dissociation from a ring. We examine the influence of the diffusion coefficient, feedback

strength, and endocytosis rate on spatial clustering by systematically varying each of these parameters. We also explore collective protein-protein interactions by means of a modified diffusion mechanism and explore the resulting influence of endocytosis rate. We analyze the clustering of proteins using the a spatial descriptive statistic that measures the average fraction of proteins within a given distance from a protein, normalized to the circumference of the ring.

4.1.2 Protein organization during cytokinesis

Cytokinesis is the final step in the cell division process in which a cell divides into two daughter cells. In animal and fungal cells, this typically involves the assembly and constriction of an actomyosin ring and formation of a cleavage furrow [113]. In order to orchestrate cytokinesis, proteins within a cell dynamically localize to different areas at different times. In some cases, proteins aggregate at specific areas to form clusters while in others they distribute evenly along the ring. Proper concentric constriction and successful completion of cytokinesis relies on precise spatial organization of proteins on the mature actomyosin ring. Understanding the underlying mechanisms of protein organization remains an active area of research, in part because failure to complete cytokinesis has been implicated in tumorigenesis and the onset of cancer [49, 51, 26].

A model organism for the study of eukaryotic cytokinesis is the fission yeast *Schizosaccharomyces pombe*. There has been significant progress made in the understanding of the mechanisms behind assembly and constriction of the actomyosin ring using fission yeast as a model system [113]. In *S. pombe* cells, proteins are recruited to the division site at the onset of anaphase to form cytokinetic nodes, which in turn recruit cytoskeletal proteins to form an actomyosin ring [113, 88]. The ring hosts many of the proteins involved in cell division and acts as a substrate for protein binding and movement. After the ring is assembled, it undergoes a maturation phase [86] during which an indentation on the cell surface known as a cleavage furrow forms on the membrane and a wall structure known as the septum ingresses [61, 144]. Successful cytokinesis occurs when constriction of this ring occurs concentrically, which requires the formation of a concentric membrane furrow [150]. Proteins associated to the ring before and during ring constriction may serve a role in ensuring timely and concentric

ring constriction. Experimental studies have shown that several cytokinetic proteins localize to the division site during the maturation phase [13, 20, 105, 118, 154] and contribute to ring constriction, including the F-BAR-domain-containing scaffold protein Cdc15.

The regulation of Cdc15 localization on the ring is achieved through cooperativity of multiple genes. The guanine nucleotide exchange factor (GEF) Gef1 activates the small GTPase Cdc42 at the actomyosin ring to promote ring constriction [32, 114]. Formins also have a role in ring assembly, as they associate to actin filament ends to regulate actin polymerization. Recent experimental studies have shown that cells containing a *gef1* deletion mutation combined with an activated allele of the formin *cdc12* exhibit non-concentric membrane furrowing [109]. In these *gef1*Δ*cdc12*Δ*503* mutant cells, Cdc15 is unevenly distributed along the cytokinetic ring which in turn contributes to an uneven rate of furrowing [109]. A potential source of Cdc15 on actomyosin rings is from endocytic actin patches. These patches are composed of branched actin and contain associated proteins including Cdc15. During endocytosis, many of these endocytic proteins are internalized into the cell, but some are left on the assembled actomyosin ring. It is possible that assembled actomyosin rings recruit groups of Cdc15 from these endocytic patches. The size and association rate of these patches of Cdc15 proteins could influence the resulting spatial distribution on the mature ring.

We explore a second model involving explicit interactions via protein binding and unbinding on the actomyosin ring along with spontaneous association of patches of molecules (rate k_{patch}). We investigate the interplay between diffusion (coefficient D_m) and binding strength (rate k_b) by systematically varying both parameters and observing the resulting spatiotemporal behavior. The molecules represent Cdc15 proteins in fission yeast, and unique patch size and association rate parameter sets are selected for each of four genotype cases: *gef1*$^+$*cdc12*$^+$, *gef1*Δ*cdc12*$^+$, *gef1*$^+$*cdc12*Δ*503*, and *gef1*Δ*cdc12*Δ*503*. These genotypes correspond to the wild-type, single mutant *gef1* deletion, single mutant activated *cdc12* deletion, and double mutant strains, respectively. Data for parameter estimation has been obtained by Cdc15 fluorescence intensity measurements and provided by the M. Das research group [109]. We characterize the degree of clustering for each of the four different simulated genotype cases by computing the coefficient of variation (CV) in protein population across

four equal ring quadrants after 20 minutes for many independent simulations. Finally, we compute a statistical average of the CV values for each modeled genotype and infer the potential mechanism underlying the observed phenotypic behavior of Cdc15 distribution on the actomyosin ring in the different strains.

4.2 Methods: Positive feedback model

We first consider a simple model of protein recruitment to the membrane that involves positive feedback. This model, illustrated in Figure 4.1, is adapted from a previously published model [7, 77]. Proteins can be either located in the cytoplasm or associated with a spatially resolved actomyosin ring of circumference 30 μm. Positions on the ring are discretized into individual lattice sites of length 0.1 μm, and multiple proteins are allowed to occupy a single lattice site. A protein can transition from the cytosol to the ring either by spontaneous association (rate k_{on}) or recruitment by another protein (rate k_{fb}). While associated with the ring, lateral diffusion occurs at a specified rate k_{hop}. Dissociation from the ring can occur either spontaneously by individual proteins (rate k_{off}) or by endocytosis (rate k_e), in which proteins associated with multiple lattice sites are removed. We model endocytosis as occurring across three consecutive lattice sites, which is meant to correspond to the approximate size of an endosome internalizing the proteins from the membrane. The probability of endocytosis occurring at a given set of three given adjacent sites is taken to be directly proportional to the fraction of the total ring protein population contained across the given set of three adjacent sites. The propensity equations for this model are described in Appendix C.1.

Additionally, we also consider protein-protein interactions by means of a modified diffusion mechanism (coefficient D_m') in which a lateral hop to a neighboring site is equally likely to occur from any occupied lattice site regardless of its protein population. This mechanism effectively reduces the hopping rate of any single protein on the ring, and accounts for slower diffusion of oligomers that may form from protein binding interactions on the membrane. With this assumption, proteins at a given site hop to adjacent lattice sites at a

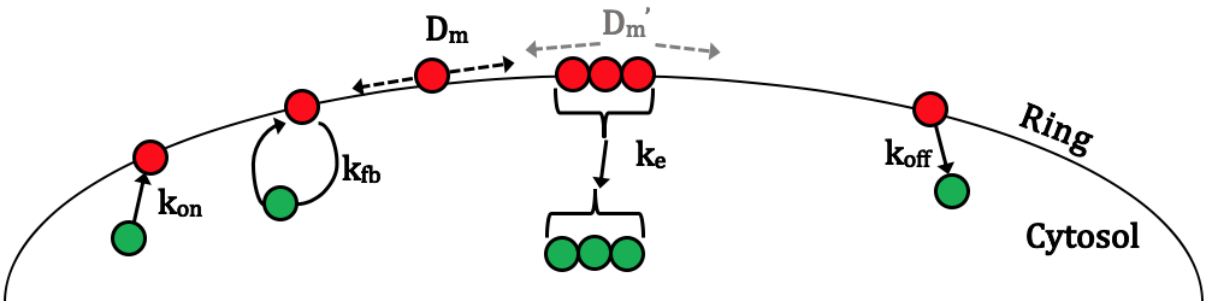

Figure 4.1: Schematic of the positive feedback circuit used to model protein organization along an actomyosin ring. Proteins are either in the cytoplasm (green) or associated with the ring (red). Transitions between the cytoplasm and ring occur by spontaneous association (k_{on}), active recruitment (k_{fb}), endocytosis (k_e), and spontaneous dissociation (k_{off}). Molecules diffuse along the membrane with diffusion coefficient D_m. At times we consider modified protein diffusion, in which molecules that are clustered diffuse more slowly ($D_m' < D_m$).

rate that is inversely proportional to the number of proteins at the site. This causes proteins to diffuse more slowly when they accumulate at a site ($D_m' < D_m$).

Stochastic simulations using the Gillespie algorithm are then used to characterize the spatiotemporal behavior of proteins on the ring with respect to the lateral diffusion coefficient D_m, feedback strength k_{fb}, and endocytosis rate k_e. We systematically vary each of these parameters by multiple orders of magnitude and study the resulting distribution of proteins over time. Since protein motion is effectively 1D, the spatiotemporal behavior can be visualized via 2D kymograph plots. Spatial descriptive statistics are then applied over multiple independent trajectories to compare the level of clustering observed under different parameter values.

4.3 Results

We begin by carrying out simulations using kinetic parameter values consistent with the previously published model [7, 77], as shown in Table 4.1.

Table 4.1: Base parameters used for positive feedback model

Parameter	Description	Value
k_{off}	Spontaneous off rate	9 min^{-1}
k_{on}	Spontaneous on rate	0.0005 min^{-1}
k_{fb}	Feedback rate	0.01 min^{-1}
k_e	Endocytosis rate	0 min^{-1}
D_m	Lateral diffusion coefficient	1.2 $\mu m^2 min^{-1}$
N	Total number of molecules	2000
L	Ring circumference	30 μm

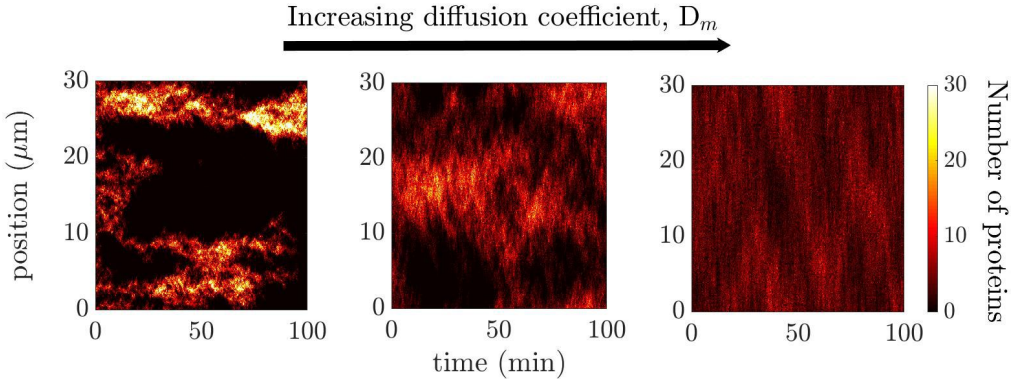

Figure 4.2: Kymographs representing the number of proteins across the ring with respect to time using parameters from Table 4.1 and varying diffusion coefficient (D_m = 0.12, 1.2, 12 $\mu m^2 min^{-1}$).

4.3.1 Large diffusion coefficients promote homogeneous spatial distributions

The influence of diffusion on the ability of the system to sustain polarity is apparent through observation of the behavior that results from varying D_m by a single order of magnitude. In the absence of protein-protein interactions, lateral diffusion distributes proteins along the ring, with higher diffusion coefficients leading to more protein movement.

As seen in Figure 4.2, fast protein diffusion leads to more even spatial distributions of protein. However, at low values of D_m, the positive feedback mechanism of protein self-recruitment leads to proteins recruiting other proteins to localized areas before they diffuse away. In this parameter regime, relatively large protein clusters form and persist for extended periods of time.

4.3.2 Feedback is necessary for polarization

We vary the feedback strength by three orders of magnitude and observe the time evolution of protein distributions on the ring, samples of which are shown in Figure 4.3a. Feedback is necessary for polarization in this model, and increasing feedback strength leads to more recruitment of proteins to the ring. However, high feedback strengths facilitate recruitment to any occupied site. When several proteins have associated to the ring at distinct locations, this leads to recruitment to multiple independent sites and thus decreases polarization. Also, since a finite total number of proteins N exists in the system, an upper limit in protein population on the ring is eventually reached at high feedback strength. When the cytoplasmic pool of proteins has been depleted and all protein is associated to the ring, recruitment only happen when preceded by a dissociation event. With diffusion being at higher propensity at these conditions, diffusive moves will be favored over dissociation and thus the spatial distribution will be more homogenized. The largest levels of polarity are instead acheived at intermediate values of k_{fb}.

4.3.3 Endocytosis in the presence of feedback suppresses clustering

We also include endocytosis with rates on the same order as those for the positive feedback, and vary the rate of endocytosis, k_e, across multiple orders of magnitude. Representative kymographs of protein organization are shown in Figure 4.3b. Increasing k_e leads to more proteins transitioning to the cytosol, and thus fewer proteins on the membrane. Clustering also decreases with increasing k_e since larger clusters on the ring are preferentially engulfed and removed. Since multiple proteins occupy single lattice sites and endocytosis dissociates all proteins from three consecutive sites, increasing feedback strength in the presence of relatively slow diffusion would not offset the low fraction of membrane-bound proteins or low levels of clustering achieved as a consequence of high endocytosis rates.

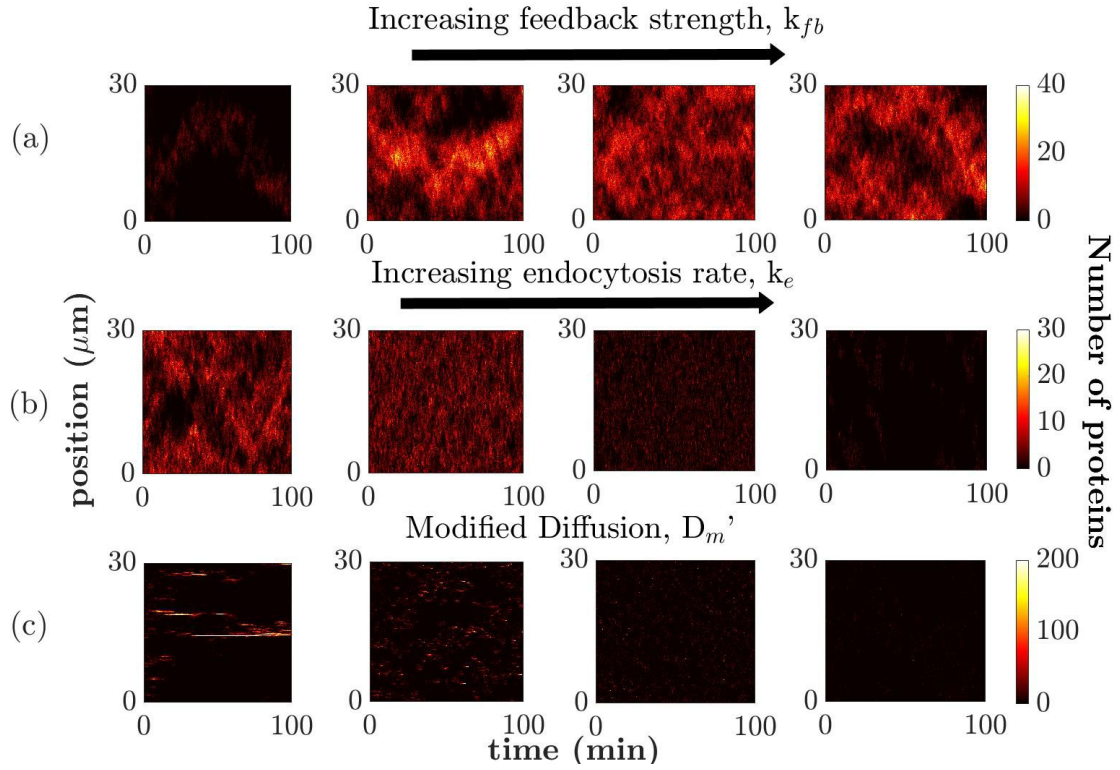

Figure 4.3: Kymographs representing the number of proteins across the ring with respect to time for cases in which (a) feedback strength is increased from left to right (k_{fb} = 0.005, 0.1, 1.0, 10.0 min^{-1}), (b) endocytosis rate is increased from left to right (k_e = 0.01, 0.1, 1.0, 2.0 min^{-1}) with constant feedback strength of k_{fb} = 0.1 min^{-1}, and (c) modified diffusion, in which the rate of diffusion D_m' for a given molecule is inversely proportional to the number of molecules in the given lattice site, is used and the endocytosis rate is again increased from left to right (k_e = 0, 0.01, 0.1, 0.5 min^{-1})

4.3.4 Endocytosis abrogates large clusters formed from protein binding interactions

Finally, diffusion is modified so that proteins that are clustered diffuse more slowly. This is meant to mimic the effects of binding interactions between membrane-bound proteins, since proteins that bind to each other to form oligomers would be more resistant to lateral diffusive motion. With this assumption, the rate of endocytosis is again varied across multiple orders of magnitude, with representative kymographs shown in Fig. 4.3c. As seen in the leftmost panel, the system exhibits clustering in the absence of endocytosis. Sustained cluster size is significantly higher since proteins within the cluster are less likely to diffuse away as the cluster grows. However, clustering is quickly abrogated with the introduction of endocytosis since the largest clusters are preferentially targeted for complete dissociation. Clustering and the number of membrane-bound proteins further decrease with increasing k_e since this again leads to larger clusters on the membrane being engulfed at a higher rate.

4.3.5 Analysis of clustering

As proteins bind to the membrane, positive feedback promotes the recruitment of more proteins to the protein-containing sites, thus creating a spatial clustering effect. Clustering at select regions of the ring gives rise to polarity. To quantify the extent of clustering in a system, various spatial descriptive statistics can be used. One common measure to detect deviations from spatial homogeneity is Ripley's K function, which in one dimension can be expressed as:

$$K(r,t) = \frac{l}{N} \sum_{i=1}^{N} \sum_{j=1}^{N} \frac{I(d_{ij}(t) < r)}{N} \tag{4.1}$$

Where N is the number of membrane-bound proteins, l is the circumference of the ring, d_{ij} is the distance between the i^{th} and j^{th} proteins, I is an indicator function that is 1 if the argument is true and 0 if it is false. The K function measures the average fraction of proteins within a given distance r from a protein, normalized to the circumference of the ring. A spatially uniform Poisson process produces a linear K vs. r relationship. In the case

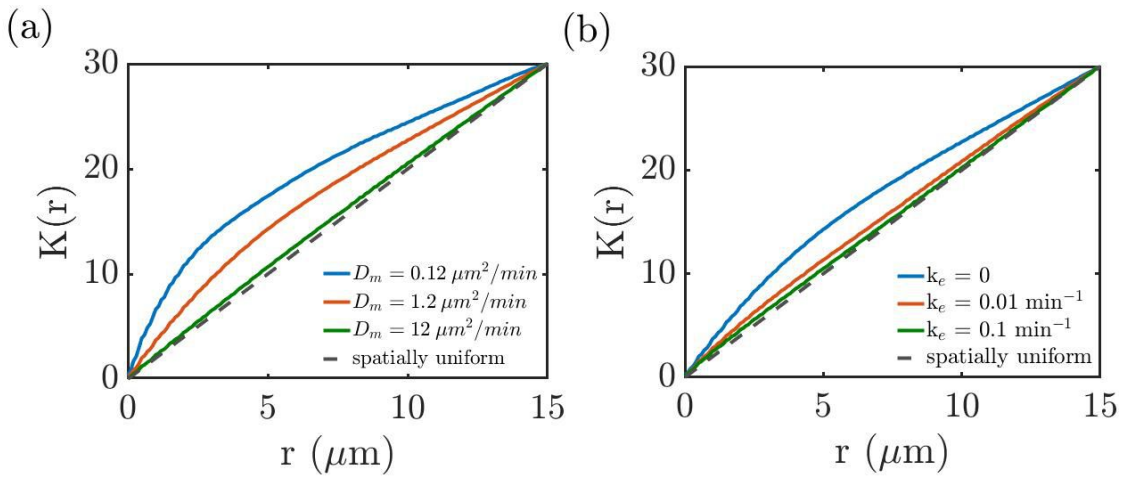

Figure 4.4: Ripley's K curves for rings of 30 μm circumference with positive feedback in recruitment at (a) varying lateral diffusion coefficients D_m and (b) varying rates of endocytosis. Parameters from Table 4.1 are used for all non-varied parameters, and each curve represents data averaged over 100 minutes for 100 independent cells. The K curve for a spatially uniform ring (dotted gray) is shown for reference.

of a 1D ring, this curve can be expressed by the equation $K(r) = 2r$. By definition, every membrane-bound protein on the ring is within a measuring distance $r = l/2$ of each other, so K evaluated at this distance is:

$$K(l/2) = (l)\frac{N^2}{N^2} = l$$

A system that exhibits some level of clustering, however, will have a higher fraction of proteins within small distances of each other, and thus have a K curve that lives above the $K(r) = 2r$ line. Two distinct regimes of increasing and then decreasing slope would indicate multiple clusters in the associated spatial pattern, with the second peak indicating the minimum distance between clusters. When applied to protein position data acquired from simulations or experiments, the Ripley's K function can be useful in quantifying clustering in the system at any point in time. By averaging $K(r)$ over many time points and many independent trajectories, one can characterize clustering behavior for a given parameter set.

To visualize the effect of diffusion on clustering, K curves are constructed for the conditions shown in Fig. 4.2 and presented in Fig. 4.4a. The K curves show less deviation from spatial uniformity as D_m increases, demonstrating that higher diffusion coefficients lead

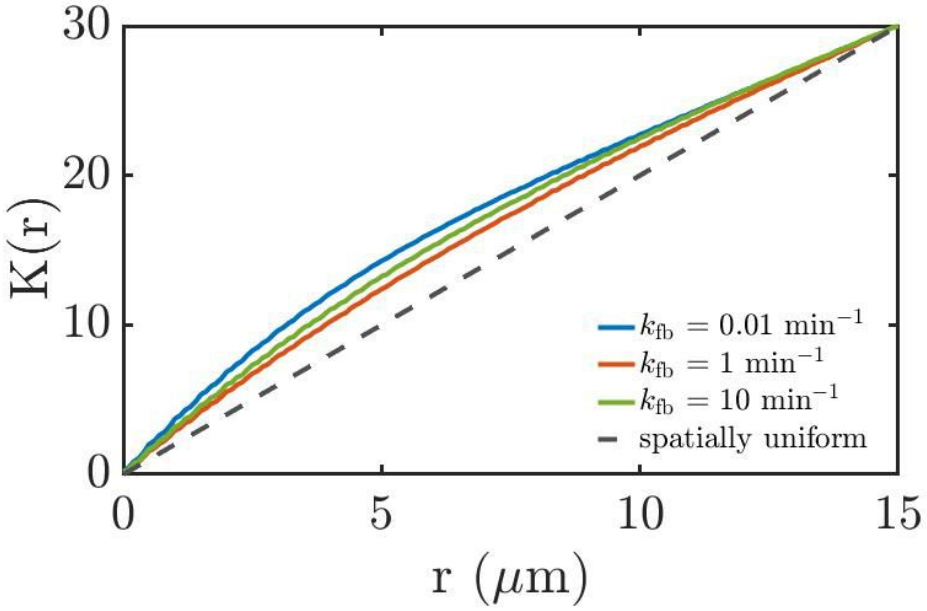

Figure 4.5: Ripley's K curves for rings of circumference 30 μm with positive feedback of varying strength k_{fb}. Parameters from Table 4.1 are used for all non-varied parameters, and each curve represents data averaged over 100 minutes for 100 independent cells. The K curve for a spatially uniform ring (dotted gray) is shown for reference.

to more homogeneous spatial distributions. Endocytosis also has a clear spatial homogenizing effect as illustrated in Figure 4.4b, where $k_e = 0.1$ min^{-1} leads to a nearly spatially uniform protein distribution.

The strength of feedback, however, does not directly correlate with level of clustering. As seen in Fig. 4.5, the lowest and highest values of k_{fb} (0.01 and 10 min^{-1}) both lead to more clustered ring configurations than the intermediate k_{fb} value of 1 min^{-1}. This reveals a non-trivial coupling between self-recruitment feedback and diffusion in the absence of endocytosis, and suggests that clustering is maximized at intermediate feedback strength.

4.4 Methods: Endocytic patch model

We also consider another model derived from an experimentally motivated hypothesis. In this model, proteins do not dissociate or recruit other proteins to the ring. Instead, proteins periodically associate in large groups from internalization of endocytic patches until ring maturation is complete. This model, illustrated in Figure 4.6, is intended to represent

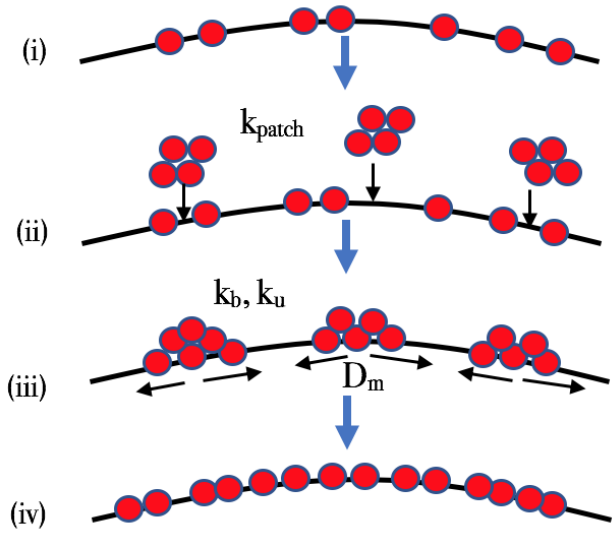

Figure 4.6: Schematic of endocytic patch recruitment model (from top down): (i) A small initial population of Cdc15 proteins (red) are randomly distributed on the ring (ii) Patches of Cdc15 proteins (from endocytic patches) associate to random locations on the ring at rate k_{patch} (iii) Proteins can bind to (rate k_b) and unbind from (rate k_u) each other and diffuse along the ring with diffusion coefficient D_m (iv) As time progresses, proteins accumulate and become distributed along the ring.

the interaction of the protein Cdc15 with the actomyosin ring during maturation prior to constriction. To elucidate the effect on Cdc15 spatial distribution of the Cdc42 activator Gef1 and the formin Cdc12, estimated parameters specific to wild-type (*gef1*$^+$*cdc12*$^+$) cells and three mutant genotypes (*gef1*Δ*cdc12*$^+$, *gef1*$^+$*cdc12*Δ*503*, and *gef1*Δ*cdc12*Δ*503*) are explicitly modeled. The number of Cdc15 molecules present on the ring after assembly and at constriction for all 4 different strains of yeast are approximated from experimental studies [158] and implemented as initial and final conditions. The number of Cdc15 molecules per cortical patch that associates to the ring for each strain is sampled from a normal (Gaussian) distribution, with the mean and variation in number of Cdc15 molecules taken from experimental studies [12]. In a single patch association event, all molecules associate to the same lattice site, which is chosen at random with no correlation with previous locations of association. We systematically vary the lateral diffusion coefficient D_m and binding rate k_b by multiple orders of magnitude at fixed unbiding rate k_u and study the resulting distribution of proteins over time. We use these results to select appropriate parameter values for use in subsequent simulations.

We consider discrete-space, continuous-time stochastic dynamics of Cdc15 proteins on a one-dimensional actomyosin ring of circumference 10 μm. The ring is again discretized into lattice sites of length 0.1 μm, and multiple proteins are allowed to occupy a single site. At the start of the maturation phase ($t = 0$), 500 Cdc15 proteins are randomly distributed on the ring. The population then steadily increases as endocytic patches near the ring are internalized, leaving groups of Cdc15 to associate with the ring. Once associated to the ring, proteins diffuse along the ring and can bind to other Cdc15 proteins and subsequently unbind. Only free (unbound) Cdc15 proteins are free to diffuse along the ring. Details of the propensity equations used in the stochastic simulation are included in Appendix C.2.

We simulate 10,000 individual trajectories for each of the four genotype strains, with each trajectory corresponding to a unique cell. We visualize spatiotemporal behavior for select cases using kymographs representing protein position over time. Additionally, we use a Gaussian kernel to mimic a fluorescence intensity visualization of Cdc15 distribution on individual mature rings. The variation in spatial distribution of each ring is then quantified by computing the coefficient of variation (CV), which is the ratio of the standard deviation σ to the mean μ, of the protein population across 4 equal quadrants of the ring. We then group the CV values for each genotype case for comparison.

4.5 Results

Networks with positive feedback are capable of producing cellular polarity. However, there is still a lack of evidence to support a self-recruitment mechanism for the cell division control protein Cdc15 in the fission yeast *Schizosaccharomyces pombe*. In this section, we explore a model of protein recruitment motivated by recent experimental studies [109]. Groups of Cdc15 molecules present in endocytic patches are recruited to the cytokinetic ring. Extracting measured values from literature and recent unpublished experimental work, we identify parameter sets for simulation of each of four distinct genotype strains: *gef1*$^{+}$*cdc12*$^{+}$, *gef1*$^{+}\Delta$*cdc12*$^{+}$, *gef1*$^{+}$*cdc12*Δ*503*, and *gef1*Δ*cdc12*Δ*503*. We then simulate the maturation period of endocytic rings in cells containing each genotype to test whether the hypothesized

clustered recruitment mechanism can lead to clusters at the end of maturation consistent with experiments.

4.5.1 Determining strain-specific model parameters

In *S. Pombe* cells, an actomyosin ring is assembled and undergoes a maturation period before constricting simultaneously with septum deposition, leading to membrane ingression and furrow formation. Previous experimental studies have indicated that the number of Cdc15 proteins present on the ring in wild-type *S. pombe* cells is $\backsim$500 upon assembly and $\backsim$2500 after maturation but prior to constriction [158]. Recent experimental work by collaborators (unpublished) [109] has shown that the number of Cdc15 proteins at maturation is lower in cells containing the activated formin mutant *cdc12*Δ*503* but remains approximately unchanged in cells containing only a *gef1* deletion [109]. Using measured fluorescence intensity data gathered by collaborators, the approximate number of Cdc15 proteins on the ring at maturation for the two activated formin mutant *cdc12*Δ*503* strains are 1820 and 1760 with and without the additional *gef1* deletion, respectively. The mean and variation in sizes of individual patches for all four strain cases are also estimated from published experimental data [12] combined with fold-change intensity measurements, and are listed in Table 4.2. The modeled rate of patch association, $\mathrm{k_{patch}}$, is computed such that the estimated total ring population will be acheived on average at a maturation time of $t_{\mathrm{final}} = 20$ minutes:

$$k_{\mathrm{patch}} = \frac{N_{\mathrm{total}} - N_0}{t_{\mathrm{final}} N_{\mathrm{patch}}} \tag{4.2}$$

where N_{total} is the total number of Cdc15 molecules on the ring at maturation and N_0 is the Cdc15 population on the ring after assembly. Given that the number of molecules in a patch is relatively large, the associated molecules on the ring are immediately considered clusters.

4.5.2 Slow diffusion and a large rate of protein-protein binding promote spatial heterogeneity

Experimental evidence has shown that Cdc15 readily oligomerizes [101], so we explicitly model protein-protein interactions on the ring in the form of binding (rate k_b) and unbinding

Table 4.2: Individual strain parameters for patch association

Case	Genotype	Patch association rate, k_{patch} (min^{-1})	Patch Size, N_{patch}
1	*gef1*$^{+}$ *cdc12*$^{+}$	0.77	130±43
2	*gef1*Δ *cdc12*$^{+}$	0.51	194±69
3	*gef1*$^{+}$ *cdc12*Δ*503*	0.41	152±46
4	*gef1*Δ *cdc12*Δ*503*	0.27	243±98

(rate k_u) reactions between Cdc15 molecules. We assume that only free monomers can laterally diffuse on the ring, so binding limits the number of proteins available to diffuse. To gauge the interplay between binding and diffusion in our model system, we vary both k_b and D_m by orders of magnitude while keeping k_u constant for the wild-type genotype case (Case 1 parameters) and observe the resulting spatiotemporal behavior of ring maturation.

As can be seen in Fig. 4.7, for slow diffusion, spatial behavior is similar across different binding strengths. Since Cdc15 associates to the ring in large groups at single locations, a low diffusion coefficient will often prevent proteins from distinct clusters from dispersing and reaching each other, thus precluding potential binding reactions between proteins originating from different clusters. Instead, binding reactions only occur between proteins of the same cluster, causing the positions of most proteins to remain relatively unchanged during maturation. At intermediate diffusion coefficients, there is noticeably more outward propagation of newly recruited clusters at low and intermediate binding rates. At very large D_m and low k_b, the initial clusters quickly overlap and the ring becomes spatially homogeneous by the end of maturation. To ensure that, on average, proteins can traverse about half the ring circumference on the 20-minute maturation timescale, we use the diffusion coefficient of 1.2 $\mu\text{m}^2\text{min}^{-1}$ used in the previous model [98, 77, 7]. To reflect the tendency of Cdc15 to readily oligomerize after dephosphorylation during mitosis, [119, 101] a binding rate on the same order as the diffusive hopping rate (100 min^{-1}) is chosen along with a much lower unbinding rate of 1 min^{-1}. This relatively high ration of binding to unbinding ensures that spatiotemporal behavior will be dependent on initial cluster size N_{patch} and association rate k_{patch}, and thus distinct for the 4 different genotype cases. A summary of these parameters is included in Table 4.3.

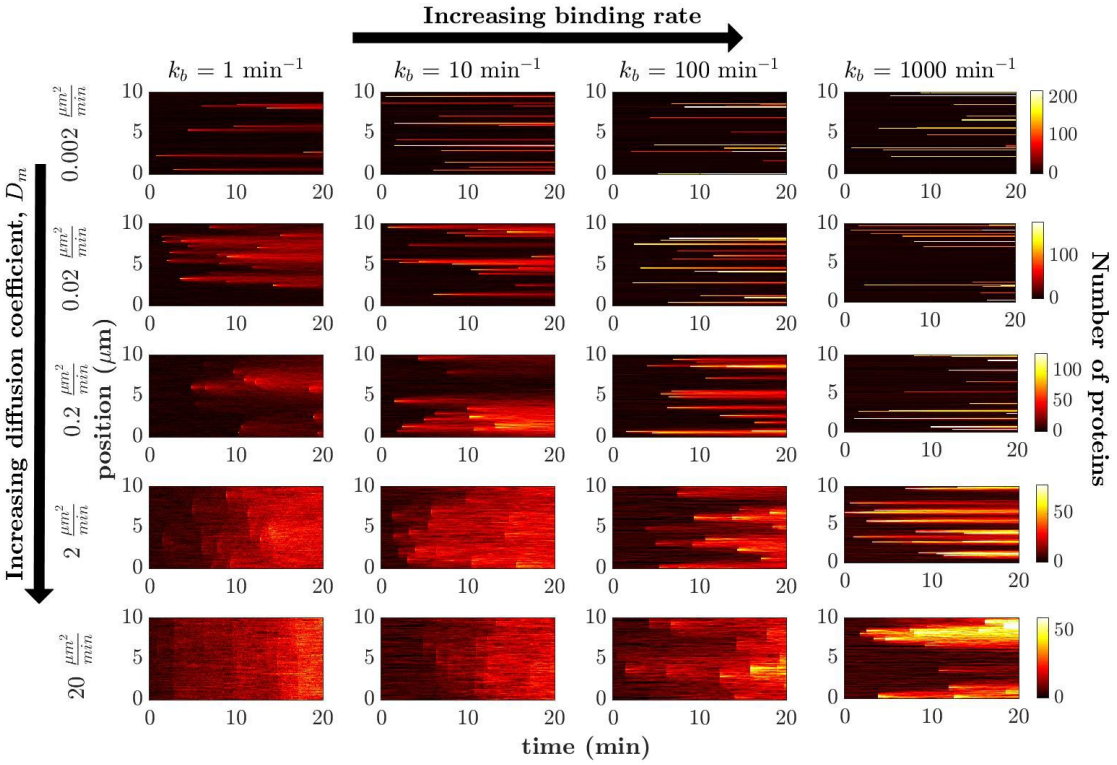

Figure 4.7: Representative 20-minute kymographs for spatial distribution of Cdc15 proteins during ring maturation at varying diffusion coefficients D_m and binding strength k_b.

Table 4.3: Global base parameters used in endocytic patch model

Parameter	Description	Value
k_b	Binding rate	100 min^{-1}
k_u	Unbinding rate	1 min^{-1}
D_m	Lateral diffusion coefficient	1.2 μm^{2}min^{-1}
N_0	Initial number of molecules	500
L	Ring circumference	10 μm
t_{final}	Maturation time	20 min

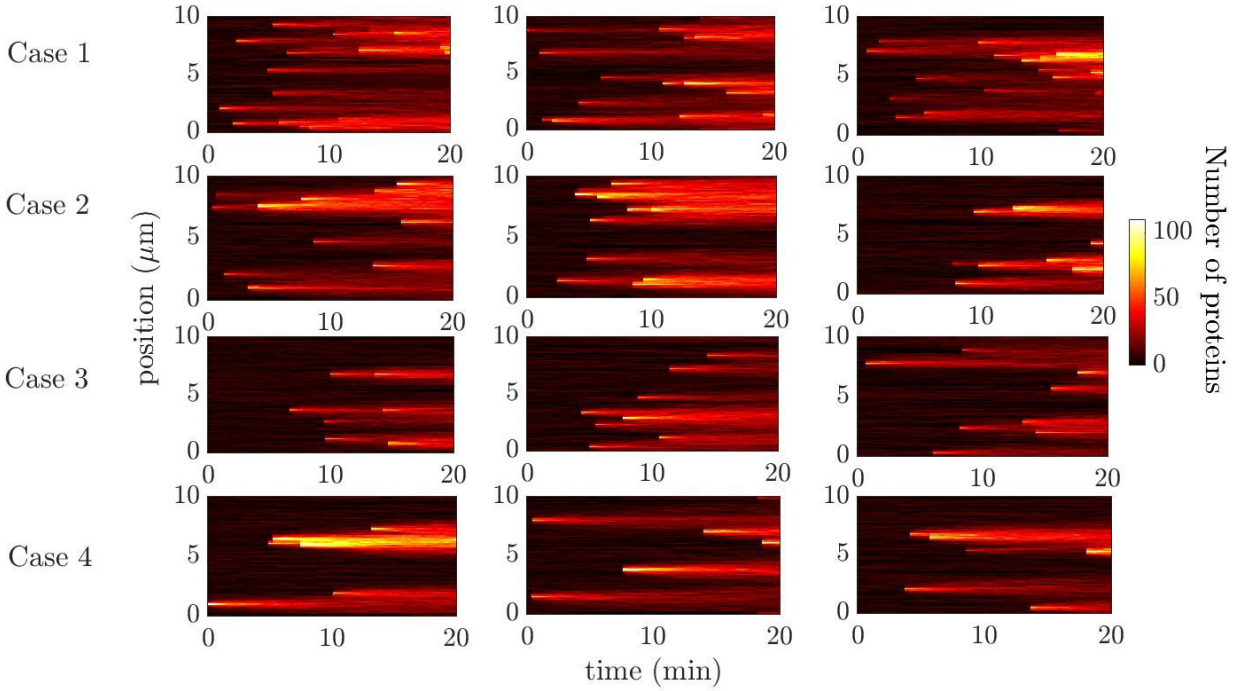

Figure 4.8: Kymographs representing the number of proteins across positions on the ring with respect to time during maturation for 3 independent cells for each of the 4 simulated genotype cases. Simulations were carried out using parameter values shown in Tables 4.2 and 4.3. The cells shown were chosen randomly from a larger set of 10,000 simulated cells.

4.5.3 Spatial heterogeneity of Cdc15 is most pronounced when few, large patches associate

Using the parameters in Table 4.3 and the parameters for different genotypes in Table 4.2, we simulate the spatial distribution of Cdc15 for many independent cells over a 20-minute ring maturation period. The spatial distribution at the end of 20 minutes is the Cdc15 distribution on the ring in a mature cell just prior to constriction for the given genotype, and a statistical analysis of this final distribution performed over many independent cells can give insight into differences between the distinct genotypes. We simulated 10,000 rings for each case. Figure 4.8 shows randomly selected examples.

As seen in Figure 4.8, the spatial behavior for a given genotype can vary considerably in different cells due to stochasticity. For example, in the last cell trajectory shown for Case 2 (2nd row, far right), the first Cdc15 patch associates much later than in the other two cells. Additionally, fewer total patches associate over the course of the 20-minute maturation

period. The end result is a ring that appears more heterogeneous due to limited spatial overlap in fewer clusters. The variation in spatiotemporal behavior increases when comparing across the different genotype cases. Given that each genotype case has a different association rate, the average total number of patches varies between cases. In the wild-type case (Case 1), an average of 15.4 patches associate in 20 minutes while in the double mutant (Case 4), an average of only 5.4 patches associate during maturation. Fewer recruited clusters provide less opportunity for spatial overlap and thus more spatial heterogeneity. To visualize the final Cdc15 distribution on the mature ring in a manner resembling fluorescence microscopy, we first transform 1D linear positions p for each protein i at $t = 20$ min into 2D circular coordinates $(x(i), y(i))$ using the following equations:

$$x(i) = \frac{d_r}{2} sin\left(\frac{2\pi p(i)}{d_r}\right) \tag{4.3}$$

$$y(i) = \frac{d_r}{2} cos\left(\frac{2\pi p(i)}{d_r}\right) \tag{4.4}$$

where d_r represents the ring diameter. We then apply a Gaussian kernel with a suitable standard deviation $\sigma = 0.1$ μm to reflect the approximate measurement resolution of a typical laboratory instrument that measures fluorescence intensity. The mature rings (at $t = 20$ min) corresponding to the spatial distributions of the randomly selected cells shown in Fig. 4.8 are shown in Fig. 4.9.

As seen in the figure, there is considerable variation in the spatial distribution among the rings, even for cells with the same genotype. The number and width of clusters vary as a result of stochasticity in number and location of patch association. The rings for the double mutant (Case 4) appear the most polarized with clusters spanning smaller arclengths along the ring. Case 4 has the smallest number of associated patches along with the largest number of Cdc15 proteins per patch. As seen in Figure 4.8, the fewer associated patches tend to either dissipate or conglomerate to form larger clusters that are more spatially confined compared to Cases 1-3.

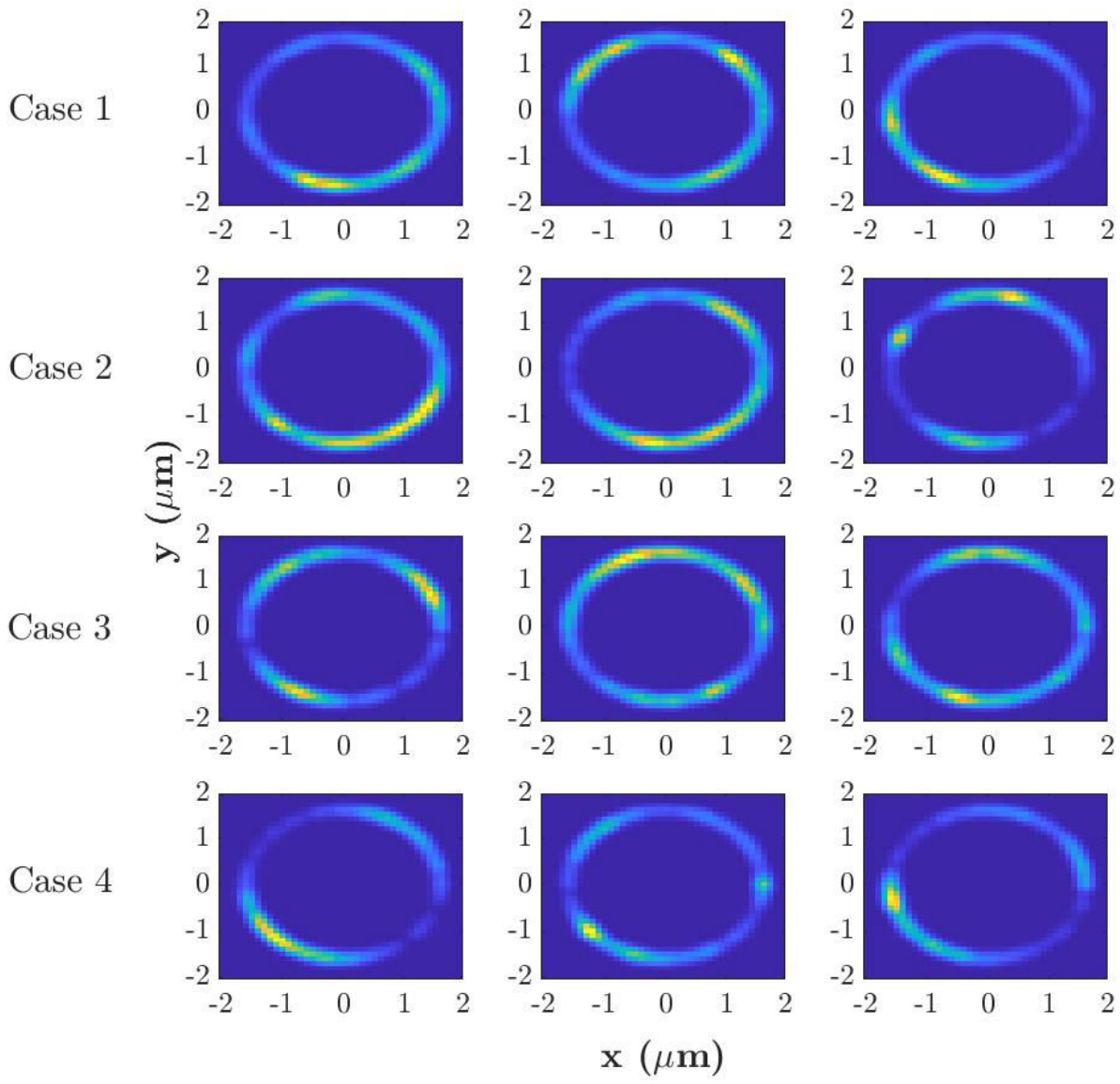

Figure 4.9: Spatial distributions of Cdc15 along the ring at $t = 20$ min for the simulated cells whose kymographs are shown in Fig. 4.8. Rings are constructed using a Gaussian kernel with standard deviation $\sigma = 0.1$ μm to mimic the resolution of experimental measurements.

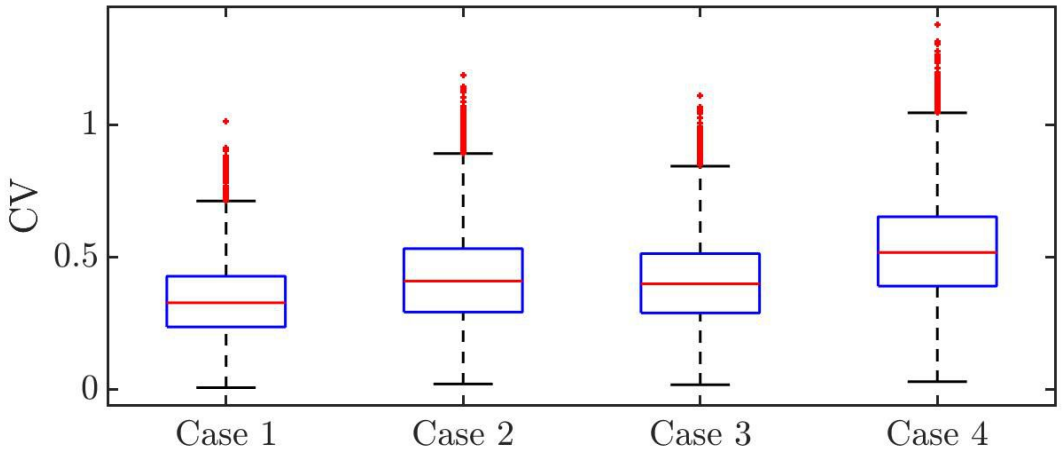

Figure 4.10: Box plots of the coefficient of variation (CV) for 10,000 simulations of each of the four simulated genotype cases. For each box, the central (red) mark is the median, the edges of the box are the 25^{th} and 75^{th} percentiles, and the whiskers extend to the most extreme data points not considered outliers. Outliers are plotted individually. The $\overline{CV}$ values for Cases 1-4 are 0.3405, 0.4217, 0.4096, and 0.5283, respectively. The differences between all pairs of cases are significant, with p-values all below 4×10^{-7}.

4.5.4 Analysis of variation in Cdc15 spatial distribution

To quantify the variation between the four genotype cases, we compute the coefficient of variation (CV) of the total Cdc15 population in individual quadrants of the ring at $t = 20$ min for all 10,000 simulated cells per case. This is done by dividing the ring into 4 equal segments, summing the total number of Cdc15 proteins in each quadrant, and dividing the standard deviation (σ) of these quadrant populations by the mean (μ) quadrant population. For a given total number of simulated cells n_{cells}, the average CV for each genotype can then be computed as:

$$\overline{CV} = \frac{\sum_{i=1}^{n_{\text{cells}}} \frac{\sigma_i}{\mu_i}}{n_{\text{cells}}} \tag{4.5}$$

A larger $\overline{CV}$ implies greater variation in population across the four ring quadrants and therefore suggests a more uneven spatial distribution of Cdc15. The CV distributions for all 4 genotype cases are depicted in the box plots shown in Figure 4.10.

The double-mutant (Case 4) shows the largest $\overline{CV}$ (0.5283) with most variation while the wild-type (Case 1) shows the smallest $\overline{CV}$ (0.3405) with least variation. To test for significance, we apply the 2-sample t-test between each pair of CV data sets across the 4

genotypes. Given the large sample size of 10,000 simulated cells, the difference between each pair of genotype cases is significant, with all p-values falling below 4×10^{-7}. These results suggest that the differences in patch association rate k_{patch} and patch size N_{patch} in the four modeled genotypes produce significant differences in the Cdc15 distribution in the mature ring.

Experimental results from a recent study show that cells lacking the Cdc42 activator Gef1, combined with an activated allele of the formin Cdc12, display non-concentric furrowing [109]. Using fluorescence microscopy, it was shown that these *gef1*Δ*cdc12*Δ*503* cells display normal actomyosin rings but uneven distribution of Cdc15 along the ring. Consistent with these findings, our simulations also show this genotype (Case 4) to have the greatest amount of spatial variation, as seen in Fig. 4.10. Slower patch recruitment dynamics for a fixed maturation time lead to association of a smaller number of recruited patches. Our results suggest that association of a smaller number of patches containing large numbers of Cdc15 proteins, along with strong binding interactions, could expain the observed phenotype of uneven Cdc15 distribution in these double mutant cells.

4.6 Conclusions

In this work, we explored two distinct models of protein organization along the cytokinetic ring. The first model relied on a positive feedback mechanism to create cell polarization. There was a continual exchange of proteins between the actomyosin ring and a bulk cytoplasmic pool via spontaneous assocation and dissociation, positive feedback recruitment of proteins to the ring, and endocytosis. Lateral diffusion was also implemented to allow for protein movement along the ring. By varying the lateral diffusion coefficient D_m, it was found that increasing diffusion promotes spatial homogeneity in protein distribution along the ring. By varying the feedback strength k_{fb}, it was apparent that feedback is necessary to obtain polarization. However, an increase in feedback strength did not necessarily translate to an increase in polarization since a high feedback rate could promote recruitment to multiple distinct local areas on the ring or deplete the cytoplasmic pool of proteins available for

recruitment. This suggests that the highest levels of polarity are achieved at low diffusion and intermediate feedback strength.

Endocytosis was found to suppress clustering and lead to a smaller fraction of ring-bound proteins. Since large numbers of spatially localized proteins are preferentially removed in an endocytic event, a larger feedback strength was found to be ineffective in offseting the depleting effects of endocytosis. Even when binding interactions between proteins on the ring were introduced, endocytosis was found to quickly abrogate any large clusters formed. When endocytosis was removed in the presence of protein-protein binding interactions, however, the system sustained clusters of many proteins confined to a smaller area since proteins are less likely to diffuse away as the cluster grows. A Ripley's K analysis of the observed clustering at the various conditions confirmed that clustering is promoted with low diffusion, low rate of endocytosis, and intermediate feedback strength.

The second model explored was motivated by a recent experimental study on Cdc15 spatial organization on the actomyosin ring in fission yeast [109]. Here, there was no removal of ring-bound proteins by any means or positive feedback recruitment by ring-bound proteins. Instead, groups of Cdc15 proteins were recruited to the ring at random locations via endocytic patches and then allowed to laterally diffuse and bind/unbind to each other. To investigate the potential roles of the Cdc42 activator gef1 and the formin Cdc12 in establishing concentric furrowing, parameter sets to represent a wild-type strain along with three mutant strains were selected from literature and determined from fluorescence intensity measurements. After simulating rings in many independent cells of each genotype, it was found that the double mutant *gef1*Δ*cdc12*Δ*503* displayed the largest variation in Cdc15 spatial distribution, an observations that is consistent with experimental findings [109]. The model suggests that the absence of Gef1 along with an activated allele of Cdc12 may result in the association of a smaller number of patches containing large numbers of Cdc15 proteins that, in the presence of strong binding interactions, lead to clustering and uneven distributions of Cdc15 on mature actomyosin rings. This in turn leads to non-concentric furrowing which compromises the fitness of the daughter cells after cytokinesis. The advancement of our understanding of the underlying mechisms behind cellular defect formation can potentially contribute to the development of improved drug treatments and targeted cell therapies.

Chapter 5

Conclusions

In this dissertation, we used computational modeling to characterize the behavior of biological systems. By explicitly defining biological processes in terms of reaction events and measurable reaction rates, one is able to construct a computational model capable of simulating the behavior associated with a wide variety of biological systems. Modern computational resources have made useful and efficient modeling approaches more accessible and feasible to implement as a primary or auxiliary method of research. The complementary nature of *in silico* methods to *in vivo* and *in vitro* experiments render them widely applicable and capable of becoming increasingly more common in biological study.

We applied a stochastic simulation algorithm in modeling three distinct biological systems. By employing data analysis and visualization methods, we were able to investigate the spatiotemporal effects of transport and network topology in a simple biochemical reaction network with positive feedback (Ch. 2), molecular motors on a cytoskeletal network of actin filaments (Ch. 3), and cell division proteins organizing on the cytokinetic ring (Ch. 4). In each system, we were able to obtain mechanistic insight regarding observable biological phenomena. The results found in these studies can be used as a vehicle for further hypothesis refinement and testing.

5.1 Confinement and diffusion in a reaction network with positive feedback (Chapter 2)

Positive feedback is a common motif in a variety of biochemical reaction networks that regulate key cellular processes including signal tranduction. Bistability is a common feature of many such networks, and allows for cellular decisions to be made in the form of a binary response. Stochastic fluctuations in a cellular environment are known to contribute to the switching between two stable states, and allow for genotypically identical cells to exhibit phenotypic differences. While many experimental and theoretical studies have advanced the understanding of the mechanisms responsible for emergent phenomena underlying networks that exhibit positive feedback and bistability, there is still no general framework for understanding the role of geometry and diffusion in signal transduction.

We used a simple two-component reaction network with positive feedback to investigate the effects of space and diffusion on bistability and stochastic switching. We employed a slab-like system geometry for the system space and varied the diffusion coefficient and level of confinement in a single dimension. By targeting both the active and inactive steady state through application of differential initial conditions, we were able to test whether a given system exhibits bistability and stochastic switching. We found that confined systems with high molecular mobility promote the active state, and stochastic switching from the inactive to active state is only observed at high levels of confinement. The activation of a system occurs via the formation of a single cluster of active molecules that quickly propagates in space. These results provide a general framework for thinking about the roles of system geometry and diffusion in positive feedback networks, and suggest that confinement can be used to initiate the formation of localized active clusters of molecules that then spatially propagate to activate a system.

5.2 First passage of molecular motors on networks of cytoskeletal filaments (Chapter 3)

Active intracellular transport is essential for maintaining proper cellular function and fitness in many eukaryotic organisms. This mode of transport is often facilitated by molecular motor proteins that bind cargo and generate directed motion along cytoskeletal filaments using energy obtained from ATP. Cytoskeletal filaments are typically arranged in a network, with individual filaments possessing a specific polarity that determines the direction a motor moves when bound to it. Recent experimental and theoretical studies have shown that the structure of a cytoskeletal network influences motor transport, but the relationship between specific filament configurations and large-scale motor transport remains largely unknown.

We used stochastic simulations to study the transport of single motors traversing cytoskeletal networks with random filament configurations. By systematically varying the number and length of filaments, we were able to characterize the first-passage times of motors traversing an interval of fixed length and identify regimes of slow and fast transport. We found that systems containing few long filaments exhibited slow and highly variable transport. We found that polarity had a large effect on transport, with the reversal of polarity on all filaments typically leading to drastic changes in mean first-passage time (MFPT). For select cases, we examined the effect of individual filaments on collective transport properties by reversing the polarity on individual filaments and measuring the resulting MFPT. We found that particular filaments can have an outsized influence on MFPT by acting as lynchpins that transport motors to and from regions of the system that act as traps that promote extended occupancy. We also found that bundling of horizontal, like-polarized filaments in a narrow region spanning the system length can reduce MFPT and FPT variablity, thus leading to fast, reliable transport.

5.3 Protein organization along the actomyosin ring during cytokinesis (Chapter 4)

Cytokinesis is the final step in the cell division process and is essential in the regulation of cell growth, development, and repair in multicellular organisms. In eukaryotes, this process typically involves the assembly, maturation, and constriction of an actomyosin ring along with a spatial coordination of various cytokinetic proteins. The homogeneous distribution of select protein species on the ring is instrumental in ensuring proper concentric ring constriction and preventing cellular defects. Recent experimental work has advanced the understanding of some key proteins and processes responsible for ring assembly and constriction, but mechanisms behind the spatiotemporal evolution of protein organization on the ring remain unknown.

We used stochastic computer simulations to explore two distinct models of protein organization along the cytokinetic ring. In the first, positive feedback resulted from a self-recruitment mechanism by proteins on the ring. Feedback was necessary to establish a polarized protein distribution, and protein clustering is suppressed by endocytosis and fast diffusion. Protein binding interactions were found to increase the number of proteins in a cluster while confining the size of the cluster region, but only in the absence of endocytosis.

In the second model, groups of cytokinetic proteins associated to the ring via endocytic patches at specified rates and subsequently diffused and interacted with other proteins along the ring in the absence of feedback or any form of dissociation from the ring. This mechanism, along with the associated parameters, was motivated by recent experiments by collaborators [109]. By systematic variation of the diffusion coefficient and protein-protein binding rates, we found that fast diffusion and weak binding promote an even protein distribution on the ring after the maturation period. The largest degrees of clustering with the most spatial variability was obtained in cells exhibiting slow association of large patches. These results suggest that homogeneous spatial distribution of proteins in mature actomyosin rings may depend on frequent association of smaller sized protein clusters.

5.4 Future prospects

In the area of intracellular transport on filamentous cytoskeletal networks, an extension to 3D systems could provide more insight into the effects of geometry and confinement on collective motor transport properties. It would be expected that a decreased level of confinement would lead to fewer junctions of close proximity filaments, and thus reduce the likelihood of local trapping regions composed of a small number of filaments. Also, since the structure of cytoskeletal networks is known to evolve in response to environmental stimuli, the implementation of continually rearranging filament structures could reveal intriguing spatiotemporal behavior.

For protein organization along the actomyosin ring, alternate assumptions can be used in modeling specific interactions between proteins on the ring. For example, limiting the number of monomer units that bind to form oligomers or allowing oligomers to laterally diffuse at lower nonzero rates can lead to alternate system behavior. Also, the implementation of alternate model considerations such as multiple interacting species of proteins or alternate mechanisms of protein exchange between the ring and cytoplasmic pool may elicudate other key spatiotemporal features of cells undergoing cytokinesis. Continued collaboration between computational modelers and experimental biologists can accelerate scientific discovery regarding the underlying mechanisms behind observed biological phenomena.

5.5 Closing

Computational modeling can be instrumental in elucidating the spatiotemporal effects of transport and network topology in biological systems. By translating complex biological processes into simplified, explicitly defined models with measurable parameters, one can elucidate key mechanistic features of emergent biological phenomena that would be otherwise unattainable by purely *in vitro* and *in vivo* methods. The establishment of an iterative feedback loop between experimental and computational research can create an efficient and sustainable model of hypothesis refinement and testing, and thus lead to accelerated scientific discovery and innovation.

Bibliography

[1] Abel, S. M., Roose, J. P., Groves, J. T., Weiss, A., and Chakraborty, A. K. (2012). The membrane environment can promote or suppress bistability in cell signaling networks. *The Journal of Physical Chemistry B*, 116(11):3630–3640. 12, 13, 29

[2] Abel, S. M., Tse, Y.-L. S., and Andersen, H. C. (2009). Kinetic theories of dynamics and persistent caging in a one-dimensional lattice gas. *Proc. Natl. Acad. Sci. USA*, 106(36):15142–15147. 62

[3] Alberts, B., Johnson, A., Lewis, J., Raff, M., Roberts, K., and Walter, P. (2008). *Molecular Biology of the Cell: 5th Edition*. Garland Science. 32

[4] Allen, R. J., Warren, P. B., and ten Wolde, P. R. (2005). Sampling rare switching events in biochemical networks. *Phys. Rev. Lett.*, 94:018104. 17

[5] Alon, U. (2007). Network motifs: theory and experimental approaches. *Nature Reviews Genetics*, 8(6):450. 12

[6] Alonso, S. and Baer, M. (2010). Phase separation and bistability in a three-dimensional model for protein domain formation at biomembranes. *Physical biology*, 7(4):046012. 12

[7] Altschuler, S. J., Angenent, S. B., Wang, Y., and Wu, L. F. (2008). On the spontaneous emergence of cell polarity. *Nature*, 454(7206):886. 64, 67, 68, 78

[8] Anderson, D. F., Enciso, G. A., and Johnston, M. D. (2014). Stochastic analysis of biochemical reaction networks with absolute concentration robustness. *Journal of The Royal Society Interface*, 11(93). 13

[9] Ando, D., Korabel, N., Huang, K. C., and Gopinathan, A. (2015). Cytoskeletal network morphology regulates intracellular transport dynamics. *Biophys. J.*, 109(8):1574–1582. 32, 33, 40, 42

[10] Andrews, S. S. and Bray, D. (2004). Stochastic simulation of chemical reactions with spatial resolution and single molecule detail. *Physical biology*, 1(3):137. 6

[11] Appert-Rolland, C., Ebbinghaus, M., and Santen, L. (2015). Intracellular transport driven by cytoskeletal motors: General mechanisms and defects. *Phys. Rep.*, 593:1–59. 31, 33

[12] Arasada, R. and Pollard, T. D. (2011). Distinct roles for f-bar proteins cdc15p and bzz1p in actin polymerization at sites of endocytosis in fission yeast. *Current Biology*, 21(17):1450–1459. 75, 77

[13] Arasada, R. and Pollard, T. D. (2014). Contractile ring stability in s. pombe depends on f-bar protein cdc15p and bgs1p transport from the golgi complex. *Cell reports*, 8(5):1533–1544. 66

[14] Arcizet, D., Meier, B., Sackmann, E., Rädler, J. O., and Heinrich, D. (2008). Temporal analysis of active and passive transport in living cells. *Phys. Rev. Lett.*, 101(24):248103. 31

[15] Aridor, M. and Hannan, L. A. (2000). Traffic jam: a compendium of human diseases that affect intracellular transport processes. *Traffic*, 1(11):836–851. 31

[16] Arkin, A., Ross, J., and McAdams, H. H. (1998). Stochastic kinetic analysis of developmental pathway bifurcation in phage λ-infected escherichia coli cells. *Genetics*, 149(4):1633–1648. 3

[17] Artyomov, M. N., Das, J., Kardar, M., and Chakraborty, A. K. (2007). Purely stochastic binary decisions in cell signaling models without underlying deterministic bistabilities. *Proceedings of the National Academy of Sciences*, 104(48):18958–18963. 11

[18] Bénichou, O., Chevalier, C., Klafter, J., Meyer, B., and Voituriez, R. (2010). Geometry-controlled kinetics. *Nature chemistry*, 2(6):472. 12, 13

[19] Bénichou, O., Loverdo, C., Moreau, M., and Voituriez, R. (2011). Intermittent search strategies. *Rev. Mod. Phys.*, 83(1):81. 32

[20] Bezanilla, M., Wilson, J. M., and Pollard, T. D. (2000). Fission yeast myosin-ii isoforms assemble into contractile rings at distinct times during mitosis. *Current Biology*, 10(7):397–400. 66

[21] Blake, W. J., Kærn, M., Cantor, C. R., and Collins, J. J. (2003). Noise in eukaryotic gene expression. *Nature*, 422(6932):633. 3

[22] Brandman, O. and Meyer, T. (2008). Feedback loops shape cellular signals in space and time. *Science*, 322(5900):390–395. 12

[23] Brangwynne, C. P., Koenderink, G. H., MacKintosh, F. C., and Weitz, D. A. (2009). Intracellular transport by active diffusion. *Trends Cell Biol.*, 19(9):423–427. 33

[24] Bressloff, P. C. and Newby, J. M. (2013). Stochastic models of intracellular transport. *Rev. Mod. Phys.*, 85(1):135. 31

[25] Butty, A.-C., Perrinjaquet, N., Petit, A., Jaquenoud, M., Segall, J. E., Hofmann, K., Zwahlen, C., and Peter, M. (2002). A positive feedback loop stabilizes the guanine-nucleotide exchange factor cdc24 at sites of polarization. *The EMBO journal*, 21(7):1565–1576. 64

[26] Caldwell, C. M., Green, R. A., and Kaplan, K. B. (2007). Apc mutations lead to cytokinetic failures in vitro and tetraploid genotypes in min mice. *J Cell Biol*, 178(7):1109–1120. 65

[27] Cebecauer, M., Spitaler, M., Sergé, A., and Magee, A. I. (2010). Signalling complexes and clusters: functional advantages and methodological hurdles. *J Cell Sci*, 123(3):309–320. 63

[28] Chou, T. and D'Orsogna, M. R. (2014). First passage problems in biology. In *First-Passage Phenomena and Their Applications*, pages 306–345. World Scientific. 33

[29] Collier, C. P. and Simpson, M. L. (2011). Micro/nanofabricated environments for synthetic biology. *Current opinion in biotechnology*, 22(4):516–526. 12

[30] Das, J., Ho, M., Zikherman, J., Govern, C., Yang, M., Weiss, A., Chakraborty, A. K., and Roose, J. P. (2009a). Digital signaling and hysteresis characterize ras activation in lymphoid cells. *Cell*, 136(2):337–351. 2, 12

[31] Das, J., Kardar, M., and Chakraborty, A. K. (2009b). Positive feedback regulation results in spatial clustering and fast spreading of active signaling molecules on a cell membrane. *The Journal of Chemical Physics*, 130(24):06B624. 12, 28, 64

[32] Das, M., Drake, T., Wiley, D. J., Buchwald, P., Vavylonis, D., and Verde, F. (2012). Oscillatory dynamics of cdc42 gtpase in the control of polarized growth. *Science*, page 1218377. 66

[33] Denisov, D., Miedema, D., Nienhuis, B., and Schall, P. (2015). Totally asymmetric simple exclusion process simulations of molecular motor transport on random networks with asymmetric exit rates. *Phys. Rev. E*, 92(5):052714. 62

[34] Doubrovinski, K. and Howard, M. (2005). Stochastic model for soj relocation dynamics in bacillus subtilis. *Proceedings of the National Academy of Sciences*, 102(28):9808–9813. 7

[35] Drubin, D. G. and Nelson, W. J. (1996). Origins of cell polarity. *Cell*, 84(3):335–344. 63

[36] Ebersbach, G. and Jacobs-Wagner, C. (2007). Exploration into the spatial and temporal mechanisms of bacterial polarity. *Trends in microbiology*, 15(3):101–108. 63

[37] Elf, J. and Ehrenberg, M. (2004). Spontaneous separation of bi-stable biochemical systems into spatial domains of opposite phases. *Systems biology*, 1(2):230–236. 12

[38] Elgart, V., Jia, T., Fenley, A. T., and Kulkarni, R. (2011). Connecting protein and mrna burst distributions for stochastic models of gene expression. *Physical biology*, 8(4):046001. 3

[39] Elowitz, M. B., Levine, A. J., Siggia, E. D., and Swain, P. S. (2002). Stochastic gene expression in a single cell. *Science*, 297(5584):1183–1186. 3

[40] Ennomani, H., Letort, G., Guérin, C., Martiel, J.-L., Cao, W., Nédélec, F., Enrique, M., Théry, M., and Blanchoin, L. (2016). Architecture and connectivity govern actin network contractility. *Current Biology*, 26(5):616–626. 32

[41] Enver, T., Pera, M., Peterson, C., and Andrews, P. W. (2009). Stem cell states, fates, and the rules of attraction. *Cell Stem Cell*, 4(5):387–397. 28

[42] Erban, R. and Othmer, H. G. (2004). From individual to collective behavior in bacterial chemotaxis. *SIAM Journal on Applied Mathematics*, 65(2):361–391. 3

[43] Fange, D. and Elf, J. (2006). Noise-induced min phenotypes in e. coli. *PLoS computational biology*, 2(6):e80. 11

[44] Ferrell Jr, J. E. (2002). Self-perpetuating states in signal transduction: positive feedback, double-negative feedback and bistability. *Current opinion in cell biology*, 14(2):140–148. 12

[45] Flenner, E., Janosi, L., Barz, B., Neagu, A., Forgacs, G., and Kosztin, I. (2012). Kinetic monte carlo and cellular particle dynamics simulations of multicellular systems. *Physical Review E*, 85(3):031907. 3

[46] François, P. and Hakim, V. (2004). Design of genetic networks with specified functions by evolution in silico. *Proceedings of the National Academy of Sciences of the United States of America*, 101(2):580–585. 12

[47] Freedman, S. L., Banerjee, S., Hocky, G. M., and Dinner, A. R. (2017). A versatile framework for simulating the dynamic mechanical structure of cytoskeletal networks. *Biophys. J.*, 113(2):448–460. 62

[48] Frigola, D., Casanellas, L., Sancho, J., and M., I. (2012). Asymmetric stochastic switching driven by intrinsic molecular noise. *PLoS ONE*, 7(2):e31407. 28

[49] Fujiwara, T., Bandi, M., Nitta, M., Ivanova, E. V., Bronson, R. T., and Pellman, D. (2005). Cytokinesis failure generating tetraploids promotes tumorigenesis in p53-null cells. *Nature*, 437(7061):1043. 65

[50] Gamba, A., de Candia, A., Di Talia, S., Coniglio, A., Bussolino, F., and Serini, G. (2005). Diffusion-limited phase separation in eukaryotic chemotaxis. *Proceedings of the National Academy of Sciences*, 102(47):16927–16932. 64

[51] Ganem, N. J., Storchova, Z., and Pellman, D. (2007). Tetraploidy, aneuploidy and cancer. *Current opinion in genetics & development*, 17(2):157–162. 65

[52] Gardiner, C. W. (2009). *Stochastic methods: a handbook for the natural and social sciences 4th edition*. Springer, Berlin. 13

[53] Gentry, B., Smith, D., and Käs, J. (2009). Buckling-induced zebra stripe patterns in nematic f-actin. *Phys. Rev. E*, 79(3):031916. 31

[54] Gierer, A. and Meinhardt, H. (1972). A theory of biological pattern formation. *Kybernetik*, 12(1):30–39. 64

[55] Gillespie, D. T. (1976). A general method for numerically simulating the stochastic time evolution of coupled chemical reactions. *Journal of computational physics*, 22(4):403–434. 5

[56] Gillespie, D. T. (1991). *Markov processes: an introduction for physical scientists*. Elsevier. 12

[57] Gillespie, D. T. (2007). Stochastic simulation of chemical kinetics. *Annual Review of Physical Chemistry*, 58:35–55. 4, 15, 34

[58] Goldstein, R. E., Tuval, I., and van de Meent, J.-W. (2008). Microfluidics of cytoplasmic streaming and its implications for intracellular transport. *Proceedings of the National Academy of Sciences*, 105(10):3663–3667. 32

[59] Goldstein, R. E. and van de Meent, J.-W. (2015). A physical perspective on cytoplasmic streaming. *Interface focus*, 5(4):20150030. 32

[60] Govern, C. C., Yang, M., and Chakraborty, A. K. (2012). Identifying dynamical bottlenecks of stochastic transitions in biochemical networks. *Physical Review Letters*, 108:058102. 28

[61] Goyal, A., Takaine, M., Simanis, V., and Nakano, K. (2011). Dividing the spoils of growth and the cell cycle: The fission yeast as a model for the study of cytokinesis. *Cytoskeleton*, 68(2):69–88. 65

[62] Greenberg, M. L. and Axelrod, D. (1993). Anomalously slow mobility of fluorescent lipid probes in the plasma membrane of the yeast saccharomyces cerevisiae. *The Journal of membrane biology*, 131(2):115–127. 64

[63] Greenfield, D., McEvoy, A. L., Shroff, H., Crooks, G. E., Wingreen, N. S., Betzig, E., and Liphardt, J. (2009). Self-organization of the escherichia coli chemotaxis network imaged with super-resolution light microscopy. *PLoS biology*, 7(6):e1000137. 64

[64] Gulli, M.-P., Jaquenoud, M., Shimada, Y., Niederhäuser, G., Wiget, P., and Peter, M. (2000). Phosphorylation of the cdc42 exchange factor cdc24 by the pak-like kinase cla4 may regulate polarized growth in yeast. *Molecular cell*, 6(5):1155–1167. 64

[65] Hafner, A. E. and Rieger, H. (2016). Spatial organization of the cytoskeleton enhances cargo delivery to specific target areas on the plasma membrane of spherical cells. *Phys. Biol.*, 13(6):066003. 32

[66] Harrington, H. A., Elisenda, F., Wiuf, C., and Stumpf, M. P. (2013). Cellular compartments cause multistability and allow cells to process more information. *Biophysical Journal*, 104(8):1824–1831. 30

[67] Hasty, J., Pradines, J., Dolnik, M., and Collins, J. J. (2000). Noise-based switches and amplifiers for gene expression. *Proceedings of the National Academy of Sciences*, 97(5):2075–2080. 7

[68] Hat, B., Kazmierczak, B., and Lipniacki, T. (2011). B cell activation triggered by the formation of the small receptor cluster: a computational study. *PLoS computational biology*, 7(10):e1002197. 12, 28

[69] Haugh, J. M. and Lauffenburger, D. A. (1997). Physical modulation of intracellular signaling processes by locational regulation. *Biophysical journal*, 72(5):2014–2031. 12

[70] Heng, Y.-W. and Koh, C.-G. (2010). Actin cytoskeleton dynamics and the cell division cycle. *Int. J. Biochem. Cell Biol.*, 42(10):1622–1633. 62

[71] Higuchi, H. and Endow, S. A. (2002). Directionality and processivity of molecular motors. *Curr. Opin. Cell Biol.*, 14(1):50–57. 32

[72] Hirokawa, N. (1998). Kinesin and dynein superfamily proteins and the mechanism of organelle transport. *Science*, 279(5350):519–526. 31

[73] Hong, Q. (2012). Cooperativity in cellular biochemical processes: noise-enhanced sensitivity, fluctuating enzyme, bistability with nonlinear feedback, and other mechanisms for sigmoidal responses. *Annual Review of Biophysics*, 41:179–204. 13

[74] Howard, J. (2001). *Mechanics of motor proteins and the cytoskeleton*. Sinauer Associates, 23 Plumtree Rd, Sunderland, MA 01375. 32

[75] Irazoqui, J. E., Gladfelter, A. S., and Lew, D. J. (2003). Scaffold-mediated symmetry breaking by cdc42p. *Nature cell biology*, 5(12):1062. 64

[76] Isaacson, S. and Peskin, C. (2006). Incorporating diffusion in complex geometries into stochastic chemical kinetics simulations. *SIAM Journal on Scientific Computing*, 28(1):47–74. 6

[77] Jilkine, A., Angenent, S. B., Wu, L. F., and Altschuler, S. J. (2011). A density-dependent switch drives stochastic clustering and polarization of signaling molecules. *PLoS computational biology*, 7(11):e1002271. 12, 28, 64, 67, 68, 78

[78] Kachar, B. (1985). Direct visualization of organelle movement along actin filaments dissociated from characean algae. *Science*, 227(4692):1355–1357. 62

[79] Kamiya, N. (1981). Physical and chemical basis of cytoplasmic streaming. *Annu. Rev. Plant Physiol.*, 32(1):205–236. 62

[80] Kapuy, O., Barik, D., Sananes, M. R. D., Tyson, J. J., and Novák, B. (2009). Bistability by multiple phosphorylation of regulatory proteins. *Progress in biophysics and molecular biology*, 100(1-3):47–56. 12

[81] Katrukha, E. A., Mikhaylova, M., van Brakel, H. X., en Henegouwen, P. M. v. B., Akhmanova, A., Hoogenraad, C. C., and Kapitein, L. C. (2017). Probing cytoskeletal

modulation of passive and active intracellular dynamics using nanobody-functionalized quantum dots. *Nat. Commun.*, 8:14772. 33

[82] Kitano, H. (2002). Computational systems biology. *Nature*, 420(6912):206. 1

[83] Kochańczyk, M., Jaruszewicz, J., and Lipniacki, T. (2013). Stochastic transitions in a bistable reaction system on the membrane. *Journal of the Royal Society Interface*, 10(84):20130151. 12, 28

[84] Kolomeisky, A. B. (2013). Motor proteins and molecular motors: how to operate machines at the nanoscale. *J. Phys.: Condens. Matter*, 25(46):463101. 32

[85] Landau, D. P. and Binder, K. (2014). *A guide to Monte Carlo simulations in statistical physics*. Cambridge university press. 3

[86] Laporte, D., Zhao, R., and Wu, J.-Q. (2010). Mechanisms of contractile-ring assembly in fission yeast and beyond. In *Seminars in cell & developmental biology*, volume 21, pages 892–898. Elsevier. 65

[87] Lauffenburger, D. A. and Linderman, J. J. (1996). *Receptors: Models for Binding, Trafficking, and Signaling*. Oxford University Press, New York. 21, 30

[88] Lee, I.-J., Coffman, V. C., and Wu, J.-Q. (2012). Contractile-ring assembly in fission yeast cytokinesis: recent advances and new perspectives. *Cytoskeleton*, 69(10):751–763. 65

[89] Lee, S. H. and Dominguez, R. (2010). Regulation of actin cytoskeleton dynamics in cells. *Mol. Cells*, 29(4):311–325. 62

[90] Lente, G. (2015). *Deterministic kinetics in chemistry and systems biology: the dynamics of complex reaction networks*. Springer. 3

[91] Lestas, I., Vinnicombe, G., and Paulsson, J. (2010). Fundamental limits on the suppression of molecular fluctuations. *Nature*, 467(7312):174. 64

[92] Levin, M. (2003). Noise in gene expression as the source of non-genetic individuality in the chemotactic response of escherichia coli. *FEBS letters*, 550(1-3):135–138. 7

[93] Lewis, A. K. and Bridgman, P. C. (1992). Nerve growth cone lamellipodia contain two populations of actin filaments that differ in organization and polarity. *J. Cell Biol.*, 119(5):1219–1243. 32

[94] Losick, R. and Desplan, C. (2008). Stochasticity and cell fate. *Science*, 320(5872):65–68. 28

[95] Loverdo, C., Bénichou, O., Moreau, M., and Voituriez, R. (2008). Enhanced reaction kinetics in biological cells. *Nat. Phys.*, 4(2):134. 32

[96] Mak, M., Zaman, M. H., Kamm, R. D., and Kim, T. (2016). Interplay of active processes modulates tension and drives phase transition in self-renewing, motor-driven cytoskeletal networks. *Nat. Commun.*, 7:10323. 32

[97] Mallik, R. and Gross, S. P. (2004). Molecular motors: strategies to get along. *Curr. Biol.*, 14(22):R971–R982. 32

[98] Marco, E., Wedlich-Soldner, R., Li, R., Altschuler, S. J., and Wu, L. F. (2007). Endocytosis optimizes the dynamic localization of membrane proteins that regulate cortical polarity. *Cell*, 129(2):411–422. 64, 78

[99] Markowetz, F. (2017). All biology is computational biology. *PLoS biology*, 15(3):e2002050. 2

[100] McAdams, H. H. and Arkin, A. (1997). Stochastic mechanisms in gene expression. *Proceedings of the National Academy of Sciences*, 94(3):814–819. 3

[101] McDonald, N. A., Vander Kooi, C. W., Ohi, M. D., and Gould, K. L. (2015). Oligomerization but not membrane bending underlies the function of certain f-bar proteins in cell motility and cytokinesis. *Developmental cell*, 35(6):725–736. 77, 78

[102] Miller, C. J., Ermentrout, G. B., and Davidson, L. A. (2012). Rotational model for actin filament alignment by myosin. *J. Theor. Biol.*, 300:344–359. 32

[103] Mlynarczyk, P. J., Pullen III, R. H., and Abel, S. M. (2016). Confinement and diffusion modulate bistability and stochastic switching in a reaction network with positive feedback. *The Journal of chemical physics*, 144(1):015102. 11, 64

[104] Morton-Firth, C. J. and Bray, D. (1998). Predicting temporal fluctuations in an intracellular signalling pathway. *Journal of Theoretical Biology*, 192(1):117–128. 7

[105] Muñoz, J., Cortés, J. C. G., Sipiczki, M., Ramos, M., Clemente-Ramos, J. A., Moreno, M. B., Martins, I. M., Pérez, P., and Ribas, J. C. (2013). Extracellular cell wall β (1, 3) glucan is required to couple septation to actomyosin ring contraction. *J Cell Biol*, 203(2):265–282. 66

[106] Neri, I., Kern, N., and Parmeggiani, A. (2013). Modeling cytoskeletal traffic: an interplay between passive diffusion and active transport. *Phys. Rev. Lett.*, 110(9):098102. 62

[107] Ohsugi, Y., Saito, K., Tamura, M., and Kinjo, M. (2006). Lateral mobility of membrane-binding proteins in living cells measured by total internal reflection fluorescence correlation spectroscopy. *Biophysical journal*, 91(9):3456–3464. 12, 28

[108] Önfelt, B., Nedvetzki, S., Yanagi, K., and Davis, D. M. (2004). Cutting edge: Membrane nanotubes connect immune cells. *The Journal of Immunology*, 173(3):1511–1513. 12

[109] Onwubiko, U., Mlynarczyk, P. J., Wei, B., Habiyaremye, J., Clack, A., Abel, S. M., and Das, M. E. (2018). The cdc42 gef, gef1, promotes uniform protein distribution along the actomyosin ring to enable concentric furrowing. Manuscript submitted for publication. 66, 76, 77, 84, 85, 89

[110] Ozbudak, E. M., Becskei, A., and van Oudenaarden, A. (2005). A system of counteracting feedback loops regulates cdc42p activity during spontaneous cell polarization. *Developmental cell*, 9(4):565–571. 64

[111] Ozbudak, E. M., Thattai, M., Lim, H. N., Shraiman, B. I., and Van Oudenaarden, A. (2004). Multistability in the lactose utilization network of escherichia coli. *Nature*, 427(6976):737. 12

[112] Parmeggiani, A., Franosch, T., and Frey, E. (2003). Phase coexistence in driven one-dimensional transport. *Phys. Rev. Lett.*, 90(8):086601. 62

[113] Pollard, T. D. (2010). Mechanics of cytokinesis in eukaryotes. *Current opinion in cell biology*, 22(1):50–56. 65

[114] Proctor, S. A., Minc, N., Boudaoud, A., and Chang, F. (2012). Contributions of turgor pressure, the contractile ring, and septum assembly to forces in cytokinesis in fission yeast. *Current biology*, 22(17):1601–1608. 66

[115] Ramadurai, S., Holt, A., Krasnikov, V., van den Bogaart, G., Killian, J. A., and Poolman, B. (2009). Lateral diffusion of membrane proteins. *Journal of the American Chemical Society*, 131(35):12650–12656. 12, 28

[116] Raser, J. M. and O'shea, E. K. (2004). Control of stochasticity in eukaryotic gene expression. *science*, 304(5678):1811–1814. 3

[117] Redner, S. (2001). *A guide to first-passage processes*. Cambridge University Press. 32

[118] Ren, L., Willet, A. H., Roberts-Galbraith, R. H., McDonald, N. A., Feoktistova, A., Chen, J.-S., Huang, H., Guillen, R., Boone, C., Sidhu, S. S., et al. (2015). The cdc15 and imp2 sh3 domains cooperatively scaffold a network of proteins that redundantly ensure efficient cell division in fission yeast. *Molecular biology of the cell*, 26(2):256–269. 66

[119] Roberts-Galbraith, R. H., Ohi, M. D., Ballif, B. A., Chen, J.-S., McLeod, I., McDonald, W. H., Gygi, S. P., Yates III, J. R., and Gould, K. L. (2010). Dephosphorylation of f-bar protein cdc15 modulates its conformation and stimulates its scaffolding activity at the cell division site. *Molecular cell*, 39(1):86–99. 78

[120] Ross, I. L., Browne, C. M., and Hume, D. A. (1994). Transcription of individual genes in eukaryotic cells occurs randomly and infrequently. *Immunology and cell biology*, 72(2):177. 7

[121] Ross, J. L., Ali, M. Y., and Warshaw, D. M. (2008). Cargo transport: molecular motors navigate a complex cytoskeleton. *Curr. Opin. Cell Biol.*, 20(1):41–47. 31

[122] Ryan, J. M. and Nebenführ, A. (2018). Update on myosin motors: Molecular mechanisms and physiological functions. *Plant Physiol.*, 176(1):119–127. 32

[123] Samii, L., Blab, G. A., Bromley, E. H., Linke, H., Curmi, P. M., Zuckermann, M. J., and Forde, N. R. (2011). Time-dependent motor properties of multipedal molecular spiders. *Phys. Rev. E*, 84(3):031111. 32

[124] Samoilov, M., Plyasunov, S., and Arkin, A. P. (2005). Stochastic amplification and signaling in enzymatic futile cycles through noise-induced bistability with oscillations. *Proceedings of the National Academy of Sciences*, 102(7):2310–2315. 3

[125] Schliwa, M. and Woehlke, G. (2003). Molecular motors. *Nature*, 422:759–765. 31

[126] Scholz, M., Burov, S., Weirich, K. L., Scholz, B. J., Tabei, S. A., Gardel, M. L., and Dinner, A. R. (2016). Cycling state that can lead to glassy dynamics in intracellular transport. *Phys. Rev. X*, 6(1):011037. 32, 33, 40, 62

[127] Shimada, Y., Wiget, P., Gulli, M.-P., Bi, E., and Peter, M. (2004). The nucleotide exchange factor cdc24p may be regulated by auto-inhibition. *The EMBO journal*, 23(5):1051–1062. 64

[128] Smits, W. K., Kuipers, O. P., and Veening, J.-W. (2006). Phenotypic variation in bacteria: the role of feedback regulation. *Nature Reviews Microbiology*, 4(4):259. 12

[129] Snider, J., Lin, F., Zahedi, N., Rodionov, V., Clare, C. Y., and Gross, S. P. (2004). Intracellular actin-based transport: how far you go depends on how often you switch. *Proc. Natl. Acad. Sci. USA*, 101(36):13204–13209. 32

[130] Sohrmann, M. and Peter, M. (2003). Polarizing without a c (l) ue. *Trends in cell biology*, 13(10):526–533. 63

[131] Srividya, I.- and Anton, Z. (2016). *First Passage Processes in Cellular Biology*, pages 261–306. Wiley-Blackwell. 33

[132] Stamnes, M. (2002). Regulating the actin cytoskeleton during vesicular transport. *Curr. Opin. Cell Biol.*, 14(4):428–433. 33

[133] Sturrock, M., Hellander, A., Matzavinos, A., and Chaplain, M. A. (2013). Spatial stochastic modelling of the hes1 gene regulatory network: intrinsic noise can explain heterogeneity in embryonic stem cell differentiation. *Journal of The Royal Society Interface*, 10(80):20120988. 7

[134] Szabo, A. (1989). Theory of diffusion-influenced fluorescence quenching. *The journal of physical chemistry*, 93(19):6929–6939. 13, 21

[135] Takahashi, K., Tănase-Nicola, S., and Ten Wolde, P. R. (2010). Spatio-temporal correlations can drastically change the response of a mapk pathway. *Proceedings of the National Academy of Sciences*, 107(6):2473–2478. 7, 12

[136] Teimouri, H., Kolomeisky, A. B., and Mehrabiani, K. (2015). Theoretical analysis of dynamic processes for interacting molecular motors. *J. Phys. A: Math. Theor.*, 48(6):065001. 62

[137] Till, J. E., McCulloch, E. A., and Siminovitch, L. (1964). A stochastic model of stem cell proliferation, based on the growth of spleen colony-forming cells. *Proceedings of the National Academy of Sciences*, 51(1):29–36. 3, 7

[138] Torney, D. C. and McConnell, H. M. (1983). Diffusion-limited reaction rate theory for two-dimensional systems. *Proc. R. Soc. Lond. A*, 387(1792):147–170. 13, 21

[139] Turing, A. M. (1952). The chemical basis of morphogenesis. *Phil. Trans. R. Soc. Lond. B*, 237(641):37–72. 64

[140] Tyson, J. J., Chen, K. C., and Novak, B. (2003). Sniffers, buzzers, toggles and blinkers: dynamics of regulatory and signaling pathways in the cell. *Current opinion in cell biology*, 15(2):221–231. 12

[141] Tyson, J. J. and Novák, B. (2010). Functional motifs in biochemical reaction networks. *Annual review of physical chemistry*, 61:219–240. 12

[142] Valdez-Taubas, J. and Pelham, H. R. (2003). Slow diffusion of proteins in the yeast plasma membrane allows polarity to be maintained by endocytic cycling. *Current biology*, 13(18):1636–1640. 64

[143] Vale, R. D. and Milligan, R. A. (2000). The way things move: looking under the hood of molecular motor proteins. *Science*, 288(5463):88–95. 31

[144] Vavylonis, D., Wu, J.-Q., Hao, S., O'shaughnessy, B., and Pollard, T. D. (2008). Assembly mechanism of the contractile ring for cytokinesis by fission yeast. *Science*, 319(5859):97–100. 65

[145] Vellela, M. and Qian, H. (2009). Stochastic dynamics and non-equilibrium thermodynamics of a bistable chemical system: the schlögl model revisited. *Journal of The Royal Society Interface*, 6(39):925–940. 13

[146] Verchot-Lubicz, J. and Goldstein, R. E. (2010). Cytoplasmic streaming enables the distribution of molecules and vesicles in large plant cells. *Protoplasma*, 240:99–107. 34

[147] Vick, J. K. and Nebenführ, A. (2012). Putting on the breaks: regulating organelle movements in plant cells. *J. Integr. Plant Biol.*, 54(11):868–874. 31

[148] Vuijk, H., Rens, R., Vahabi, M., MacKintosh, F., and Sharma, A. (2015). Driven diffusive systems with mutually interactive langmuir kinetics. *Phys. Rev. E*, 91(3):032143. 62

[149] Walters, M. C., Fiering, S., Eidemiller, J., Magis, W., Groudine, M., and Martin, D. (1995). Enhancers increase the probability but not the level of gene expression. *Proceedings of the National Academy of Sciences*, 92(15):7125–7129. 7

[150] Wang, N., Lee, I.-J., Rask, G., and Wu, J.-Q. (2016). Roles of the trapp-ii complex and the exocyst in membrane deposition during fission yeast cytokinesis. *PLoS biology*, 14(4):e1002437. 65

[151] Wedlich-Soldner, R., Altschuler, S., Wu, L., and Li, R. (2003). Spontaneous cell polarization through actomyosin-based delivery of the cdc42 gtpase. *Science*, 299(5610):1231–1235. 64

[152] Wedlich-Soldner, R., Wai, S. C., Schmidt, T., and Li, R. (2004). Robust cell polarity is a dynamic state established by coupling transport and gtpase signaling. *J Cell Biol*, 166(6):889–900. 63, 64

[153] Wehrens, M., ten Wolde, P. R., and Mugler, A. (2014). Positive feedback can lead to dynamic nanometer-scale clustering on cell membranes. *The Journal of chemical physics*, 141(20):11B614_1. 12, 28

[154] Wei, B., Hercyk, B. S., Mattson, N., Mohammadi, A., Rich, J., DeBruyne, E., Clark, M. M., and Das, M. (2016). Unique spatiotemporal activation pattern of cdc42 by gef1 and scd1 promotes different events during cytokinesis. *Molecular biology of the cell*, 27(8):1235–1245. 2, 66

[155] Weiss, M., Elsner, M., Kartberg, F., and Nilsson, T. (2004). Anomalous subdiffusion is a measure for cytoplasmic crowding in living cells. *Biophys. J.*, 87(5):3518–3524. 62

[156] Wells, A. L., Lin, A. W., Chen, L.-Q., Safer, D., Cain, S. M., Hasson, T., Carragher, B. O., Milligan, R. A., and Sweeney, H. L. (1999). Myosin vi is an actin-based motor that moves backwards. *Nature*, 401(6752):505. 31

[157] Woodhouse, F. G. and Goldstein, R. E. (2013). Cytoplasmic streaming in plant cells emerges naturally by microfilament self-organization. *Proceedings of the National Academy of Sciences*, 110(35):14132–14137. 32

[158] Wu, J.-Q. and Pollard, T. D. (2005). Counting cytokinesis proteins globally and locally in fission yeast. *Science*, 310(5746):310–314. 75, 77

[159] Xu, J., King, S. J., Lapierre-Landry, M., and Nemec, B. (2013). Interplay between velocity and travel distance of kinesin-based transport in the presence of tau. *Biophys. J.*, 105(10):L23–L25. 34

Appendices

A Analysis of the chemical master equation and cluster formation

.

In this section, we provide details of the analysis used in Section 2.3.2. We begin by solving for the steady state distribution of the Markov chain describing the dynamics of the stochastic, well-mixed chemical kinetics. We then consider the system in the slow-diffusion regime and investigate the relationships between D, L (system size), and the likelihood of stochastic switching.

A.1 Steady state distribution

Consider a system consisting of N molecules. The Markov chain consists of $N+1$ states indexed by $k \in \{0, 1, 2, \ldots, N\}$. State k corresponds to a state with k molecules of type X and $N-k$ molecules of type A (Fig. A.1). State k can transition only to states $k+1$ and $k-1$. The transition rates from k to $k+1$ and from k to $k-1$ are given, respectively, by

$$\gamma_{k,k+1} = \big(N-k\big)k_1 + \big(N-k\big)\binom{k}{2}\tilde{k}_3$$
$$\gamma_{k,k-1} = \big(k\big)k_2 + \binom{k}{3}\tilde{k}_4 \ ,$$

where $\tilde{k}_3$ and $\tilde{k}_4$ are defined as before. Let π_k denote the steady state probability of being in state k. It is straightforward to formally solve for the distribution by balancing fluxes throughout the Markov chain. Starting with state 0, one can iteratively obtain

$$\pi_k = \left(\frac{\gamma_{k-1,k}}{\gamma_{k,k-1}}\right)\pi_{k-1} = \pi_0 \prod_{j=1}^{k}\left(\frac{\gamma_{j-1,j}}{\gamma_{j,j-1}}\right)$$

Using the normalization condition, $\sum_{k=0}^{N}\pi_k = 1$, one can write

$$\pi_0 = \left(1 + \frac{\gamma_{01}}{\gamma_{10}} + \frac{\gamma_{01}\gamma_{12}}{\gamma_{21}\gamma_{10}} + \cdots + \frac{\gamma_{01}\cdots\gamma_{N-1,N}}{\gamma_{N,N-1}\cdots\gamma_{10}}\right)^{-1}$$

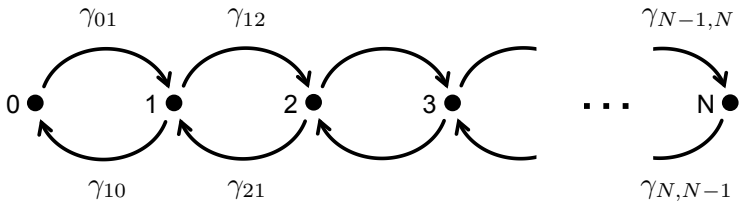

Figure A.1: Schematic of the Markov chain. States are labeled by the number of X molecules.

A.2 Cluster formation in the slow diffusion regime

We now wish to explore the system described in Section 2.3.2 in the slow diffusion regime. We begin by noting that the expected lifetime of an isolated X molecule is $\tau_X \sim k_2^{-1}$. In this time, the characteristic distance traversed by the molecule is $\xi \sim \sqrt{D/k_2}$. This length scale defines a spatial domain over which the X molecule can interact with other molecules while it is "active." The volume sampled by the molecule (assuming no wall effects) thus scales as $V_\xi \sim \xi^3 \sim (D/k_2)^{3/2}$. With the total concentration of molecules defined as c, the average number of molecules in the spatial domain is $N_\xi \sim cV_\xi$. If the volume V_ξ is small compared with the total system volume, then we can expect the number of molecules to be approximately Poisson distributed, with number fluctuations characterized by $N_\xi \sim cV_\xi \pm \sqrt{cV_\xi}$.

As noted in the Section 2.3.2, in the limit of immobile molecules, a large concentration of molecules must be present at a single lattice site in order to favor an active state (defined here as more than half of the molecules being in the X state). We wish to explore the effect of increasing the diffusion coefficient, and thus expanding the effective range over which molecules interact, using the scaling arguments introduced in the previous paragraph. For various values of ξ, we solve the master equation directly and determine the minimum total number of molecules (N) needed in volume V_ξ so that $\sum_{k=N/2}^{N} \pi_k \geq 0.9$. That is, we seek the smallest value of N such that a substantial portion of the steady state probability is associated with the active state (results are similar for values other than 0.9). Figure A.2 shows the effective concentration needed to satisfy this condition as a function of ξ. The concentration is reported as $n = (N/V_\xi)a^3$, which gives the average number of molecules in a volume the size of a single lattice site (for perspective, the highest concentration considered

in the main text gives $n = 1$ and the concentration at $L = 0.1$ μm gives $n = 0.1$). The curve is a decreasing function of ξ, with large values at small ξ. The range of n spans concentrations that are both larger and smaller than those considered in Fig. 2.3.

Using the curve constructed above, we now seek insight into the characteristic diffusion coefficient needed to promote stochastic switching. Letting c_L denote the concentration of molecules in a slab geometry with confinement length L, the average occupancy of a volume the size of a lattice site is $n_L = c_L(1 \pm 1/\sqrt{c_L V_\xi})a^3$. As ξ increases, the concentration required to significantly populate the active state decreases. At sufficiently large ξ, the required concentration crosses below the value of $c_L(1 + 1/\sqrt{c_L V_\xi})a^3$. Once the concentration of the domain exceeds the concentration needed to significantly populate the active state, spontaneous cluster formation is relatively likely to occur (using $c_L\, a^3$ instead of the upper fluctuation leads to larger domains but qualitatively similar results). We follow this procedure for various values of L and determine $D_c \sim k_2 \xi_L^2$ as a function of L, where ξ_L denotes the length at which the crossover occurs. This is plotted in Fig. A.2B and is consistent with intuition: As the system concentration decreases (larger L), larger diffusion coefficients are needed to promote interactions between molecules.

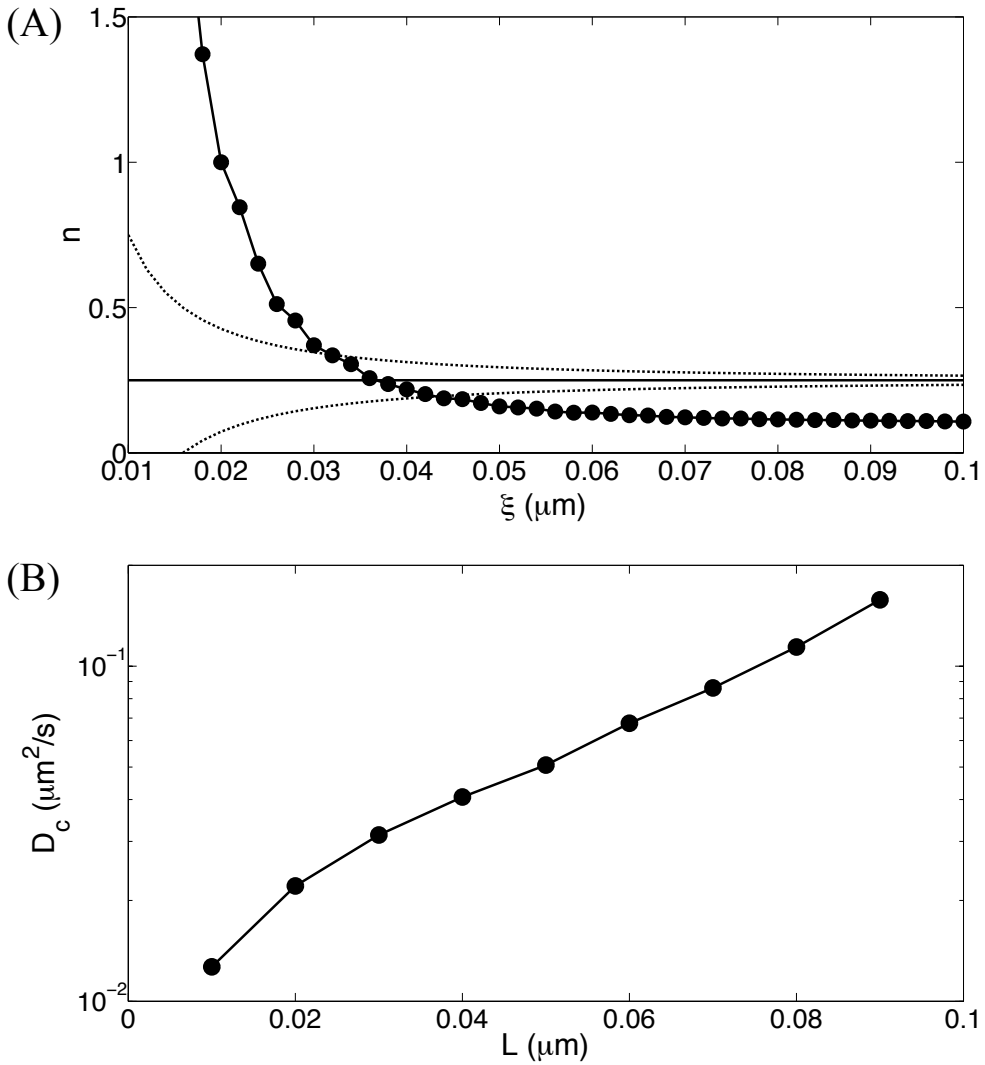

Figure A.2: **(A)** Concentration needed to ensure a substantial active state within a system of volume $V_\xi = \xi^3$. Concentration is reported as $n = (N/V_\xi)a^3$. The large circles are obtained by solving the Markov chain exactly and determining the minimum number of molecules needed to have at least 90% of the steady state probability in active states. The solid horizontal line is the concentration (in molecules per lattice site) associated with the slab geometry with $L = 0.04$ μm. The dashed lines represent characteristic concentration fluctuations, $n_L = c_L(1 \pm 1/\sqrt{c_L V_\xi})a^3$. **(B)** For various values of L, we plot the diffusion coefficient (D_c) associated with the value of ξ such that $c_L(1+1/\sqrt{c_L V_\xi})a^3$ first exceeds the curve in (A) obtained by solving the master equation.

B Mean square displacement curves for D_e estimation

Here, we extend the results seen in Figure 3.10 to include the mean-square displacement curves with power-law fits for all filament lengths considered. As described in Section 3.3.6, motors begin in the center of a 100 μm $\times$ 100 μm domain with 200,000 filaments of the specified filament length randomly dispersed in the system space. This gives a filament concentration of 20 filaments/μm^2, which is equivalent to $N_f = 2000$ in the 20 μm $\times$ 5 μm system.

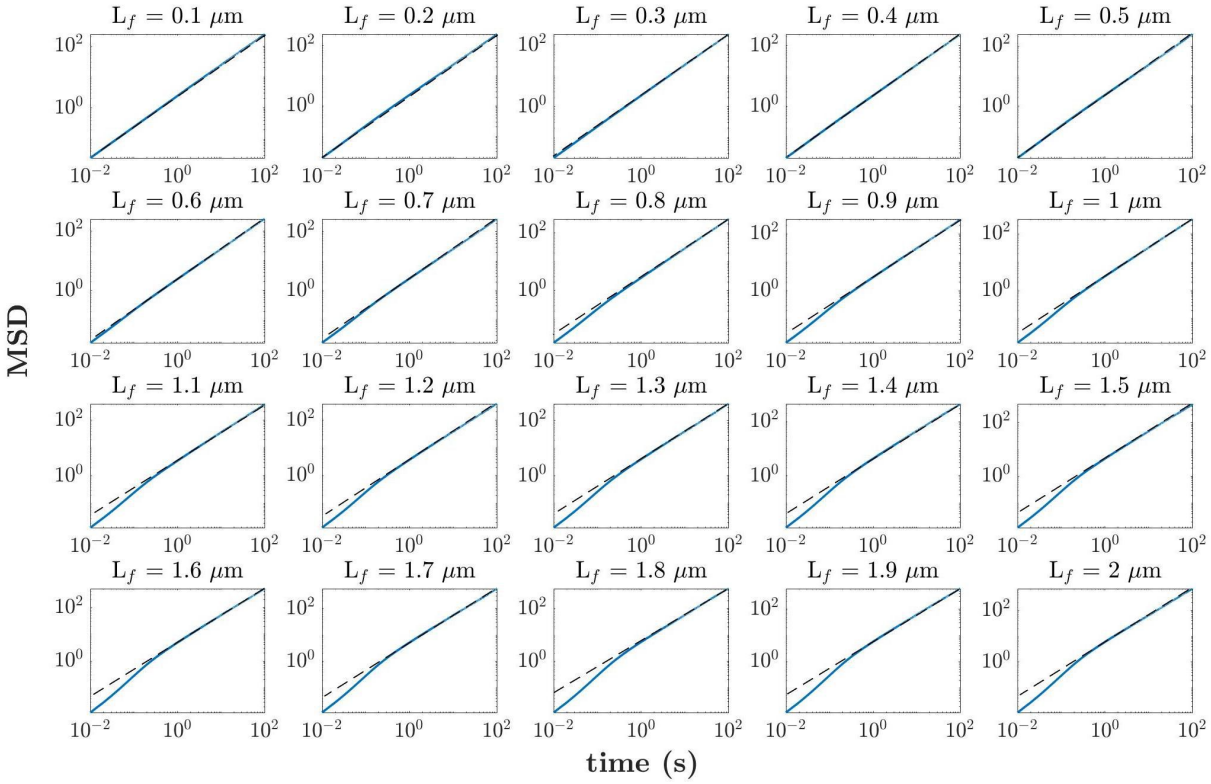

Figure B.1: Mean square displacement (MSD) with power-law fits to long time for motors in a 100 μm $\times$ 100 μm domain with 200,000 filaments of varying length. Data for each plot is obtained from 1000 independent trajectories of 100 s each.

Linear behavior in MSD at sufficiently long times indicates diffusive behavior. The short-time behavior for longer filaments indicates superdiffusive behavior. As seen in Fig B.1, motors exhibit diffusive behavior over the entire time interval only for short filament lengths. The short-time (< 1 s) behavior becomes noticeably superdiffusive when filament lengths exceed 0.7 μm.

C Protein organization along the actomyosin ring: Model propensity equations

In this section, we provide the propensity equations used to implement the Gillespie algorithm for the two protein organization model constructions described in Chapter 4. Each propensity equation describes the rate at which a particular reaction event occurs. The probability of a given reaction i occuring on the time interval $[t_0, t_0+\tau]$ can be computed as:

$$P\{i, t_0 < t < t_0 + \tau\} = \frac{a_i(t_0)}{\sum_{i=1}^{n} a_n(t_0)}$$

C.1 Positive feedback model

$$\text{Association}: \quad a_1(t) = k_{\text{on}} N_{\text{cyt}}(t)$$

$$\text{Dissociation}: \quad a_2(t) = k_{\text{off}}(N - N_{\text{cyt}}(t))$$

$$\text{Recruitment}: \quad a_3(t) = k_{\text{fb}} N_{\text{cyt}}(N - N_{\text{cyt}}(t))$$

$$\text{Diffusion}: \quad a_4(t) = k_{\text{hop}}(N - N_{\text{cyt}}(t))$$

$$\text{Endocytosis}: \quad a_5(t) = k_e(N - N_{\text{cyt}}(t))$$

Where $N_{\text{cyt}}(t)$ represents the number of proteins in the cytoplasm at time t, with N being the conserved total number of proteins in the system. The rate constants for association, dissociation, and recruitment are expressed as k_{on}, k_{off}, and k_{fb} respectively. The constant k_{hop} is proportional to the diffusion coefficient D_m and represents the rate at which proteins hop to nearest neighbor lattice sites.

C.2 Endocytic patch model

$$\text{Association}: \quad a_1(t) = \begin{cases} k_{\text{patch}} & N(t) < N_{\text{total}} \\ 0 & N(t) \geq N_{\text{total}} \end{cases}$$

$$\text{Diffusion}: \quad a_2(t) = \sum_{i=1}^{n_{\text{sites}}} N_u(i,t)$$

$$\text{Binding}: \quad a_3(t) = k_b \sum_{i=1}^{n_{\text{sites}}} \max\{[N_u(i,t) - 1], 0\}$$

$$\text{Unbinding}: \quad a_4(t) = k_u(N - 1 - \sum_{i=1}^{n_{\text{sites}}} N_u(i,t)$$

Here, $N(t)$ is the number of Cdc15 molecules on the ring at time t, n_{sites} is the total number of lattice sites, and $N_u(i,t)$ represents the number of unbound proteins in lattice site i at time t. N_{total} is the experimentally measured average number of proteins on the ring at the end of maturation. The rates of patch association and hopping to a nearest neighbor lattice site are expressed as k_{patch} and k_{hop}, respectively. The propensity of binding, $a_3(t)$, is the product of the binding rate constant k_b and the number of potential bonds in the system while the propensity of unbinding, a_4, is the product of the unbinding rate constant k_u and the number of bonds in the system.

Vita

Paul John Mlynarczyk was born to Andrzej and Mary Mlynarczyk in Park Ridge, Illinois on June 3, 1986. After graduating from Maine East High School in 2004, he attended the *University of Illinois at Urbana-Champaign* where he earned his Bachelor of Science degree in Chemical Engineering with a minor in Computer Science in May 2008. While working as a Product Control Engineer in the steel industry, he earned a Master of Science degree in Chemical Engineering from *North Carolina State University* in May 2011. Shortly after joining the research group of Dr. Steven Abel at the *University of Tennessee* in the fall of 2013, he became a licensed Professional Engineer and earned a second Master of Science degree from *Kansas State University* in August 2014 with research in theoretical models of the polymer glass transition temperature. His doctoral research focused on computational modeling of transport processes in biological systems. He intends to resume his industrial career by pursuing work in biotechnology.